Development of nanofluids based on nanoencapsulated phase change materials
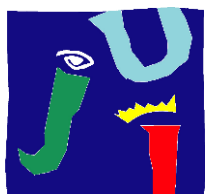
A dissertation presented by Nuria Navarrete Argilés for the Degree of Doctor of Philosophy

AUTHORED BY:
NURIA NAVARRETE ARGILÉS

SUPERVISED BY:
ROSA MONDRAGÓN CAZORLA

CASTELLÓN DE LA PLANA, MARCH 2020

DESARROLLO DE NANOFLUIDOS BASADOS EN MATERIALES DE CAMBIO DE FASE NANOENCAPSULADOS

Memoria presentada por Nuria Navarrete Argilés para optar al grado de doctora por la Universitat Jaume I

AUTORA:

NURIA NAVARRETE ARGILÉS

DIRECTORA:

ROSA MONDRAGÓN CAZORLA

CASTELLÓ DE LA PLANA, MARZO 2020

FUNDING

Predoctoral contract:

- *Ayuda predoctoral para la formación de personal investigador FPI – UJI, dentro del Plan de Promoción de la Investigación de la UJI 2016* (Ref. PREDOC/2016/28). Universitat Jaume I.
  1 de marzo de 2017 – 29 de febrero de 2020

Research stays:

- Birmingham Centre for Energy Storage (BCES), Birmingham, United Kingdom.
  6th February 2017 – 26th February 2017
  Financed by COST Action CA15119 NANOUPTAKE (European Cooperation in Science and Technology) from European Union.

- Birmingham Centre for Energy Storage (BCES), Birmingham, United Kingdom.
  31st July 2017 – 20th August 2017
  Financed by COST Action CA15119 NANOUPTAKE (European Cooperation in Science and Technology) from European Union.

- Delft University of Technology (TU Delft), Delft, the Netherlands.
  3rd September 2018 – 21st December 2018
  Financed by *Beca para realizar estancias temporales en otros centros de investigación, para el personal docente e investigador de la Universidad del Plan de Promoción de la Investigación de la UJI 2018* (Ref. E-2018-10).

COMPENDIUM OF PUBLICATIONS

- Navarrete, N., Gimeno-Furió, A., Mondragón, R., Hernández, L., Cabedo, L., Cordoncillo, E. & Juliá, J. E. Nanofluid based on self-nanoencapsulated metal/metal alloys phase change materials with tuneable crystallisation temperature. *Scientific Reports* 7, 1–10 (2017).
  DOI: 10.1038/s41598-017-17841-w
  Impact factor: 4.011

- Navarrete, N., Mondragón, R., Wen, D., Navarro, M. E., Ding, Y. & Juliá, J. E. Thermal energy storage of molten salt-based nanofluid containing nano-encapsulated metal alloy phase change materials. *Energy* 167, 912–920 (2019).
  DOI: 10.1016/j.energy.2018.11.037
  Impact factor: 5.537

- Navarrete, N., Gimeno-Furió, A., Forner-Escrig, J., Juliá, J. E. & Mondragón, R. Colloidal stability of molten salt-based nanofluids: Dynamic Light Scattering tests at high temperature conditions. *Powder Technology* 352, 1–10 (2019).
  DOI: 10.1016/j.powtec.2019.04.045
  Impact factor: 5.439

- Navarrete, N., La Zara, D., Goulas, A., Valdesueiro, D., Hernández, L., van Ommen, J. R. & Mondragón, R. Improved thermal energy storage of nanoencapsulated phase change materials by atomic layer deposition. *Solar Energy Materials & Solar Cells.* 206, 110322. 2020. ISSN 0927-0248.
  DOI: 10.1016/j.solmat.2019.110322
  Impact factor: 6.019

"This thesis has been accepted by the co-authors of the publications listed above that have waved the right to present them as a part of another PhD thesis"

To my parents,
this thesis is thanks to them
because they made me who I am

ABSTRACT

The present thesis is intended to deal with the synthesis and characterisation of nanofluids (liquids with nanometric particles dispersed in them) that include phase change materials as nanoparticles. The main goal of the work is to develop new materials that suppose an enhancement in the heat transfer properties and thermal storage capacity of the currently available technologies.

Energy transition is one of the key challenges of our time. Moving towards renewable and clean energy sources will suppose a decrease in the CO_2 emissions majorly responsible for greenhouse effect, as well as providing an alternative to fossil fuels, whose availability is uncertain in the future, especially when considering the increasing world energy demand. Solar thermal energy is one of the technologies englobed as renewable, being the Sun a reliable and massive source.

Concentrated solar power (CSP) plants harvest the radiation coming from the Sun and transform it into electricity, and the current technology allows for an intermediate step of thermal energy storage that allows power generation even when intermittencies of the source take place (because of night time or weather conditions). Therefore, in CSP plants a heat collection and transfer step can be found usually through the use of thermal oils as heat transfer fluid, and also a storage stage that uses molten salts as thermal energy storage materials.

In this thesis the focus is put in the creation of nanofluids based on both these types of fluids (thermal oils and molten salts) to improve the efficiency of CSP plants. The election of nanoencapsulated phase change materials (nePCMs) to be added as the solid part of the nanofluid is due to their capacity of storing thermal energy as latent heat, besides the common storage mechanism through sensible heat.

Nevertheless, the inclusion of phase change materials in a base fluid, and specially metals, which were studied in this work, carries some difficulties with it that need to be looked into. The need of a core-shell structure in the nanoparticles, of an encapsulation able to withstand working parameters such as high temperatures and thermal cycling, or of the mitigation of negative supercooling effects, are challenges that have to be faced prior to the addition of the nanoparticles into the base fluid, and that have been dealt with through this work. Solutions

for the effective nanoencapsulation of PCM cores are offered, testing their suitability for their use in thermal applications, and a way to control supercooling through the use of non-eutectic metallic alloys is presented.

Moreover, nanofluids that are used for high temperature often present additional problems, such as interactions between the base fluid and nanoparticles that can result in the damage of those, or lack of colloidal stability, that means a detriment in the enhanced properties of the nanofluid. Both of these issues have also been studied in this thesis, ensuring that compatibility between the nanofluid components was present, and developing a new experimental set-up for colloidal stability analysis by measuring dynamic light scattering at high temperature.

As a result, different nanofluids based on a synthetic thermal oil (Therminol 66) and molten salts (a mixture of $NaNO_3$ and KNO_3 in a 60:40 wt.% commonly known as solar salt) have been synthesised and characterised in order to study the influence of nePCMs addition (Sn, Sn/Pb and Al/Cu encapsulated nanoparticles) on their thermal properties such as thermal conductivity, heat transfer capacity, specific heat and thermal energy storage capacity.

Finally, a cutting-edge technology such as atomic layer deposition (ALD) has been used to synthesise encapsulation coatings of very few nanometres (SiO_2 and Al_2O_3), and their influence on the nanofluids characteristics were evaluated, resulting in positive effects in the thermal energy performance of the nanofluids studied.

RESUMEN

La presente tesis pretende lidiar con la síntesis y caracterización de nanofluidos (líquidos con partículas nanométricas dispersadas en su interior) que incluyen materiales de cambio de fase como nanopartículas. El objetivo principal del trabajo es desarrollar nuevos materiales que supongan una mejora en las propiedades de transferencia de calor y capacidad de almacenamiento térmico respecto a las tecnologías disponibles en la actualidad.

La transición energética es uno de los retos principales de nuestro tiempo. El cambio a fuentes de energía renovables y limpias supondrá un descenso en las emisiones de CO_2, principal responsable del efecto invernadero, al mismo tiempo que proporcionará una alternativa a los combustibles fósiles, cuya disponibilidad para el futuro es incierta, especialmente cuando se tiene en cuenta el crecimiento de la demanda energética global. La energía solar térmica es una de las tecnologías englobadas como renovables, ya que el Sol es una fuente fiable e inmensa.

Las centrales termosolares absorben la radiación proveniente del Sol y la transforman en electricidad. Además, la tecnología actual permite la existencia de una etapa intermedia de almacenamiento de energía térmica, que permite la generación de electricidad incluso cuando existen intermitencias en la fuente (por ser de noche, o debido a las condiciones climáticas). Por lo tanto, en las centrales termosolares se puede encontrar una unidad de absorción y transferencia de calor, conseguido normalmente mediante el uso de aceites térmicos como fluidos de transferencia de calor, y otra unidad de almacenamiento de energía, que usa sales fundidas como materiales de almacenamiento térmico.

En esta tesis, la mayor atención está puesta en la creación de nanofluidos basados en ambos tipos de fluidos (aceites térmicos y sales fundidas) para mejorar la eficiencia de las centrales termosolares. La elección de materiales de cambio de fase nanoencapsulados para ser añadidos como la parte sólida de los nanofluidos se debe a su capacidad de almacenar energía térmica como calor latente, aparte del mecanismo común de almacenamiento por calor sensible.

No obstante, la introducción en los fluidos base de materiales de cambio de fase, especialmente cuando se trata de metales como en este trabajo, conlleva algunas dificultades que necesitan ser estudiadas. La necesidad de una estructura de corteza y núcleo en las

nanopartículas, un encapsulado capaz de soportar parámetros de funcionamiento tales como altas temperaturas y ciclado térmico, o la atenuación de los efectos negativos del superenfriamiento, son retos a los que hay que enfrentarse antes de añadir las nanopartículas al fluido base, y que se han estudiado en este trabajo. En él se ofrecen soluciones para la nanoencapsulación efectiva de núcleos de materiales de cambio de fase, probando su idoneidad para ser usados en aplicaciones térmicas, y se presenta un mecanismo para controlar el superenfriamiento mediante el uso de aleaciones metálicas no eutécticas.

Por otra parte, los nanofluidos utilizados a alta temperatura frecuentemente presentan problemas adicionales, como las interacciones entre el fluido base y las nanopartículas que pueden resultar en el deterioro de las mismas o la falta de estabilidad coloidal, en detrimento de las propiedades mejoradas del nanofluido. Estos dos temas se han estudiado en esta tesis, asegurando la compatibilidad de ambos componentes de cada nanofluido, y desarrollando un nuevo montaje experimental para medir la estabilidad coloidal a alta temperatura por medio de la dispersión dinámica de la luz.

Como resultado, varios nanofluidos basados en un aceite térmico sintético (Therminol 66) y en sales fundidas (una mezcla de $NaNO_3$ y KNO_3 en una proporción 60:40 wt.% conocida comúnmente como sal solar) han sido sintetizados y caracterizados con el objetivo de estudiar la influencia de la introducción de materiales de cambio de fase nanoencapsulados (nanopartículas encapsuladas de Sn, Sn/Pb y Al/Cu) en sus propiedades térmicas tales como conductividad térmica, capacidad de transferencia de calor, calor específico y capacidad de almacenamiento térmico.

Finalmente, se ha utilizado una tecnología novedosa como la deposición de capa atómica para sintetizar encapsulados con cortezas de muy pocos nanómetros (de SiO_2 y Al_2O_3), y se ha estudiado su influencia en las características de los nanofluidos, comprobando que tienen efectos positivos en el comportamiento térmico de los nanofluidos estudiados.

RESUM

La present tesi pretén tractar la síntesi i caracterització de nanofluids (líquids amb partícules nanomètriques dispersades en el seu interior) que inclouen materials de canvi de fase com a nanopartícules. L'objectiu principal del treball és desenvolupar nous materials que suposen una millora en les propietats de transferència de calor i capacitat d'emmagatzematge tèrmic respecte a les tecnologies disponibles en l'actualitat.

La transició energètica és un dels reptes principals del nostre temps. El canvi a fonts d'energia renovables i netes suposarà un descens en les emissions de CO_2, principal responsable de l'efecte hivernacle, al mateix temps que proporcionarà una alternativa als combustibles fòssils, la disponibilitat dels quals és incerta per al futur, especialment quan es té en compte el creixement de la demanda energètica global. L'energia solar tèrmica és una de les tecnologies englobades com renovables, ja que el Sol és una font fiable i immensa.

Les centrals termosolars absorbeixen la radiació provinent de el Sol i la transformen en electricitat. A més, la tecnologia actual permet l'existència d'una etapa intermedia d'emmagatzematge d'energia tèrmica, que permet la generació d'electricitat fins i tot quan hi ha intermitències a la font (per ser de nit, o a causa de les condicions climàtiques). Per tant, en les centrals termosolars es pot trobar una unitat d'absorció i transferència de calor, aconseguit normalment mitjançant l'ús d'olis tèrmics com fluids de transferència de calor, i una altra unitat d'emmagatzematge d'energia, que fa servir sals foses com materials de emmagatzematge tèrmic.

En aquesta tesi, la principal atenció està centrada en la creació de nanofluids basats en ambdós tipus de fluids (olis tèrmics i sals foses) per millorar l'eficiència de les centrals termosolars. L'elecció de materials de canvi de fase nanoencapsulats per ser afegits com la part sòlida dels nanofluids es deu a la seua capacitat d'emmagatzemar energia tèrmica com a calor latent, a part del mecanisme comú d'emmagatzematge per calor sensible.

No obstant això, la introducció en els fluids base de materials de canvi de fase, especialment quan es tracta de metalls com en aquest treball, comporta algunes dificultats que necessiten ser estudiades. La necessitat d'una estructura d'escorça i nucli en les nanopartícules, un encapsulat capaç de suportar paràmetres de funcionament com ara altes temperatures i ciclat tèrmic, o l'atenuació dels efectes negatius de l'superrefredament, són reptes als quals cal

enfrontar-se abans d'afegir les nanopartícules al fluid base, i que s'han estudiat en aquest treball. S'hi ofereixen solucions per a la nanoencapsulació efectiva de nuclis de materials de canvi de fase, provant la seua idoneïtat per a ser usats en aplicacions tèrmiques, i es presenta un mecanisme per controlar el superefredament mitjançant l'ús d'aliatges metàl·lics no eutèctics.

D'altra banda, els nanofluids utilitzats a alta temperatura freqüentment presenten problemes addicionals, com les interaccions entre el fluid base i les nanopartícules que poden resultar en el deteriorament de les mateixes o la falta d'estabilitat col·loïdal, en detriment de les propietats millorades de l'nanofluid. Aquests dos temes s'han estudiat en aquesta tesi, assegurant la compatibilitat de tots dos components de cada nanofluid, i desenvolupant un nou muntatge experimental per mesurar l'estabilitat col·loidal a alta temperatura per mitjà de la dispersió dinàmica de la llum.

Com a resultat, diversos nanofluids basats en un oli tèrmic sintètic (Therminol 66) i en sals foses (una barreja de N_aNO_3 i KNO_3 en una proporció 60:40 wt.% coneguda comunament com a sal solar) han estat sintetitzats i caracteritzats amb l'objectiu de estudiar la influència de la introducció de materials de canvi de fase nanoencapsulats (nanopartícules encapsulades de Sn, Sn/Pb i Al/Cu) en les seues propietats tèrmiques com ara conductivitat tèrmica, capacitat de transferència de calor, calor específic i capacitat d'emmagatzematge tèrmic.

Finalment, s'ha utilitzat una tecnologia innovadora com la deposició de capa atòmica per a sintetitzar encapsulats amb escorces de molt pocs nanòmetres (de SiO_2 i Al_2O_3), i s'ha estudiat la seua influència en les característiques dels nanofluids, comprovant que tenen efectes positius en el comportament tèrmic dels nanofluids estudiats.

ACKNOWLEDGEMENTS

I would like to thank both my supervisors: Quique, who started me in this research thing and walked me through the first steps, helping me become who I am now and acting sometimes as a father as well as a mentor, and of course, Rosa Mondragón, for the support and trust even at the times when I seemed a bit stuck, and for all she has taught me not only about labs, but also about teaching. Thank you for reviewing so fast, too. I would also like to thank Leonor Hernández and the rest of the Multiphase Fluids Group, for their collaboration over these years.

I would also like to express my gratitude to Prof. Yulong Ding from the University of Birmingham for taking me into his group on both my research stays at the BCES, to Helena, for always taking care of everything related to them, and to the rest of the lunch group, for making them fun. Also in Birmingham, I got to know Belén, who I really want to thank for all she has taught me about CSPs and molten salts, and her support as a kind of elder research sister.

In a similar way, I want to thank Prof.dr.ir Ruud van Ommen from TU Delft for accepting me into his group and teaching me all I know about ALD and MLD along with Aris, Damiano, Jordi and Max. Thank you for always finding a way to fit all my experiments in your already busy schedules. Also thanks to David Valdesueiro, for putting me into contact with them when I asked him for a research stay. I want to thank too David, Alba and of course, Rosi, for always joining on the trips, lunches, evenings at the botanical, and every sort of plan we came up with. The three of them along with the international friends (from BE, ESN Delft, and specially Marc) made those four months amazing.

I would also like to express my gratitude to the people at Universitat Jaume I that have helped me in this work, in particular to the SCIC technicians (special thanks to Cristina for the many

hours dedicated to DSC), to the administrative staff of the department (Marian and Rosa), and also to Gladys, who always has an encouraging word to give.

Of course I have to thank all the people with whom I have shared office over the years, extensive to the ones joining the coffee breaks. Thanks to Adrián, Carlos, Daniel and Laura for the advices, laughs and random conversations that have often meant a necessary break from work. Also thanks to Fani, who was there at the beginning as a workmate and is now a dear friend. And many, many, many thanks to Alexandra and Marta, because they have to be the best people to share an office with (if you are not afraid of strange things happening), thank you for your laughs, support, and help at any time I have needed it.

I wish to thank the rest of my friends, either from Castellón, Teruel, Mallorca or Vienna, for listening to me and sharing life views whenever I had concerns over work, and adding lots of good times to these years.

Y finalmente, gracias a mi familia. A mi hermano, que más o menos sabe lo que hago, y a mis padres, que no tanto, pero de los que nunca me ha faltado el apoyo y el cariño, esta tesis es gracias a ellos porque ellos son los que me han hecho quien soy.

CONTENTS

LIST OF FIGURES

LIST OF TABLES

Nomenclature

ALD	Atomic Layer Deposition	F	Faraday constant
CSP	Concentrated Solar Power	G	Gravity acceleration
DLS	Dynamic Light Scattering	h	heat transfer coefficient
DSC	Differential Scanning Calorimetry	I	Ionic strength
EDX	Energy-Dispersive X-ray spectroscopy	k_B	Boltzmann constant
EELS	Electron Energy-Loss Spectroscopy	m	Mass
FT-IR	Fourier-Transform Infrared spectroscopy	Mo	Mouromtseff number
GPC	Growth Per Cycle	Nu	Nusselt number
HTF	Heat Transfer Fluid	q	Energy density storage
ICP-OES	Inductively Coupled Plasma Optical Emission Spectroscopy	R	Ideal gas constant
		R_H	Hydrodynamic radius
IL	Ionic Liquids	T	Temperature
LCOE	Levelized Cost Of Energy	t	Time
LDV	Laser Doppler Velocimetry	V	Volume
LFA	Laser Flash Analysis	w	Mass fraction
PCM	Phase Change Material	X	Displacement of a particle
nePCM	Nanoencapsulated Phase Change Material	zi	Ionic charge
SEM	Scanning Electron Microscopy	E	Dielectrical constant
STEM	Scanning Transmission Electron Microscopy	η	Viscosity
TEM	Transmission Electron Microscopy	κ^{-1}	Electrical double layer thickness
TES	Thermal Energy Storage	ϕ	Volume fraction
TGA	Thermogravimetrical Analysis	k	Thermal conductivity
THW	Transient Hot Wire	ρ	Density
XRD	X-Ray Diffraction		
		Subscripts	
Symbols		bf	Base fluid
α	Thermal diffusivity	$cryst1$	First crystallisation
A	Particle radius	$cryst2$	Second crystallisation
A_{eff}	Hamaker constant	exp	Experimental value
c_i	Concentration of ions	$fusion$	Fusion
c_p	Specific heat	$latent$	Latent heat
D	Diameter	nf	Nanofluid
ΔH	Phase-change enthalpy	np	Nanoparticles
ΔT	Temperature step	o	Vaccuum
D_t	Translational diffusion coefficient	$sensible$	Sensible heat
EC	Electrical conductivity	th	Theoretical value
ε_r	Relative error	$total$	Total energy

Chapter 1: INTRODUCTION

One of the great global challenges of the 21st century is to mitigate and adapt to the effects of Global Warming. The global temperature has raised an average of 1 ^{o}C since 1880, with eighteen of the nineteen warmest years registered taking place since 2001[1]. Human activity in the last few decades has been determined to be extremely likely to contribute to this changes in our climate[2], partly due to the emissions of greenhouse gases. Approximately, two thirds of the global greenhouse gas emissions are related to the use of fossil fuels in energy production[3]. In Europe, a 78% of the total greenhouse gasses emissions in 2017 was related to energy processes[4]. The need to reduce this environmental impact has led to stablish goals like cutting greenhouse gas emissions by 80-95 % by 2050, in order to limit the global temperature increase to 2 ^{o}C with respect to pre-industrial levels, as decided during the Paris Agreement[5].

Besides, the predicted increase of energy demands due to industrialisation of less developed countries and growth of the global population, along with the uncertainty of the availability of commonly used energy sources such as fossil fuels to cover for these future energy demands[6], leads to the need to find alternative energy sources. This, paired with the need to reduce CO_2 emissions in order to mitigate greenhouse effect, has boosted the relevance of research in renewable and clean energy sources.

Renewables energies represented a 26.2% of the global electricity generation in 2018, and a 30.7% in Europe[5] and this share is expected to increase in the near future. Regarding the possible sources for this energy transition, the Sun emits yearly an equivalent to about 7000 times the world primary energy consumption per year[7], which makes it the most abundant potential energy source on Earth.

Two main technologies of solar energy harvesting exist in the present: photovoltaics and solar thermal. The former uses semiconducting materials that exhibit the photovoltaic effect, i.e.

they are able to convert light into electric current. The latter harvests the radiation coming from the Sun as thermal energy, using it in heating processes (such as warming water for sanitary use) or in a steam cycle to produce electricity, as it is the case of concentrated solar power (CSP) plants.

1.1   Concentrated Solar Power Plants

In CSP plants, radiation coming from the sun is concentrated in a collector using mirrors. A heat transfer fluid (HTF) absorbs the resulting thermal energy and transports it to a heat exchanger where water is heated for the production of steam, which feeds a turbine connected to an electricity generator.

According to the shape of the mirrors and their arrangement within the plant, four typical CSP configurations can be found: parabolic trough, parabolic dish, Fresnel reflectors and power tower. Both parabolic trough and Fresnel reflectors concentrate radiation linearly on a pipe containing a HTF, whereas parabolic dishes and the heliostats in power towers focus the radiation on a single point. Schemes of how some of these plant configurations work are depicted in Figure 1.1.
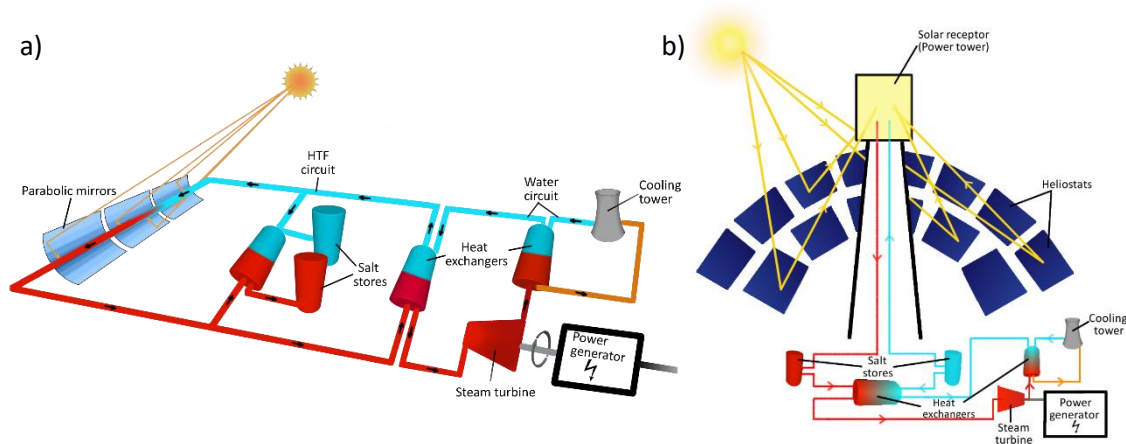
Figure 1.1. Scheme of CSP plants with (a) parabolic trough and (b) power tower collectors.

An advantageous feature of CSP plants is that when the amount of harvested energy exceeds the power demand in that moment, the HTF can be pumped to a different sector of the circuit, which contains a second heat exchanger used to heat up a thermal energy storage (TES) material. This sector usually consists of two different tanks (hot and cold) filled with molten salts. Energy is stored as heat in the hot tank, so when the power demand exceeds the energy production, the TES material is transferred from the hot tank to the cold one through a heat exchanger in which the HTF is heated before joining the main circuit again. This way, the plant can keep working and power demands can be covered despite the intermittencies of sunlight availability (e.g. during night time or adverse weather conditions).

Broadly speaking, the main difference between CSP plants with line focussing and ones with point focussing is the working temperatures reached and, as a consequence, the HTF used. In the case of CSP plants with linear concentration, the operation temperatures reached are around 390 $^{\circ}$C, so the most commonly used HTFs are thermal oils. However, in CSP plants in which the solar radiation is concentrated in a single point, such as power towers, the temperatures reached are above 500 $^{\circ}$C, allowing for the HTF to be the same material used as thermal storage, commonly molten salts[8]. This can be observed in Figure 1.1, where the

scheme in (a) shows a parabolic trough plant that uses different fluids as thermal absorption fluid and storage material, whereas the power tower plant in (b) uses the same one for both purposes. Although some power tower plants also combine different fluids, the use of molten salts as a heat transfer material is also present in the industry.

Nevertheless, one of the main disadvantages of both thermal oils and molten salts is that their thermal properties are relatively low, especially when compared to those of water, commonly used as HTF for low temperature applications. Namely, thermal conductivity values are usually less than 0.4 W/m·K for thermal oils and 0.5 W/m·K for solar salt (a mixture of nitrates commonly used in the industry), whereas for water is between 0.55 and 0.65 W/m·K. Besides, specific heat ranges around 2.5 J/g·K for thermal oils and 1.5 J/g·K for solar salt, compared to the 4.2 J/g·K of water[9,10]. For this reason, research in HTFs has focused in mechanisms to improve their thermal conductivity, to make the collection and transport of energy more efficient, and their specific heat, so the thermal energy storage capacity can be increased.

One of the ways to increase these thermal properties of a fluid is by adding very small solid particles, creating what is known as a nanofluid.

1.2 NANOFLUIDS

A nanofluid is a colloidal suspension of solid nanometric particles, usually in a range from 10-100 nm, homogeneously dispersed in a liquid or gas. There are several reasons to add solid particles to a fluid, and one of them is to improve its thermal properties. The combination of solid particles with a fluid in order to improve its properties was a concept already studied by Maxwell[11], and many applications have been researched through time for fluids in which micrometric particles were added. However, the main difficulty when working with this kind of suspensions is the tendency of the particles to settle due to gravity, which causes the fluid properties to stop being homogeneous, but disadvantages regarding clogging in pumps and tubes can also be found. This adversities can be overcome by means of nanoparticles.

In nanofluids, due to the small range of sizes, the surface-to-volume ratio of the particles is so high that the interactions are mainly defined by short-range phenomena like Van der Waals attraction and surface forces. Therefore, the force fields created by each of the particles are stronger than the gravity forces, so instead of precipitating they follow a random movement called Brownian. This means that if the particles are somehow kept from agglomeration, a fully engineered nanofluid will have been synthesised, in which the thermal properties of the solid coexist to a certain extent with the transport properties of the fluid.

Research in nanofluids started in 1993 with a paper published by Masuda[12]. Two years later, in 1995, Choi coined the term[13] and ever since, research of nanofluids with improved thermal properties has been extended and broadened. Traditionally, the most commonly studied nanofluids have been those using water as the base fluid[14–17]. However, their use is limited for low and medium-low temperature applications. Regarding medium and high-temperature applications, thermal oils, glycols and molten salts are used as base fluids, and since their thermal properties are inherently worse than those of water, the improvements in their thermal conductivity and specific heat are of great relevance.

The main properties to study in nanofluids are the following:

- **Thermal conductivity**: is the capacity of transferring heat from a material to another that is in contact with it. The highest the thermal conductivity is for a material, the

3

higher the transfer rate. The addition of nanoparticles of high thermal conductivity materials (e.g. metals) is used to improve this property in HTFs.

- **Thermal storage capacity**: is the sum of the sensible heat (the capacity of materials to absorb or release thermal energy when its temperature varies) and the latent heat (the capacity of storing/releasing heat during phase changes). It plays a very important role in TES materials. Regarding sensible heat, the addition of solid materials with a lower sensible heat (c_p) should mean a decrease in the specific heat of the nanofluid compared to the base fluid, according to the mixture rule. However, abnormal enhancements have been registered for the specific heat of nanofluids when they are based in ionic liquids (including molten salts)[18–22]. This phenomenon has been determined to be related to ionic exchange between the nanoparticles and the base fluid[23].

- **Colloidal stability**: refers to the capacity of the particles to remain homogeneously dispersed in the suspension through time, without agglomerating or settling. In this respect, nanoparticles present an advantage respect to micrometric particles, since their reduced size causes Brownian motion to outcome gravity action. Colloidal stability is a key issue in nanofluids. Aggregation of the nanoparticles has to be avoided for them to stay suspended. In some cases, the stability can be achieved by electrostatic repulsion in polar solvents (e.g. changing the pH of the solution[24] for water-based nanofluids) or by means of steric repulsion, the preferred method for non-polar solvents (e.g. using anti-agglomerant/surfactant agents). However, depending on the working temperature of the nanofluid, it is difficult to find a stabiliser that does not suffer from thermal degradation. That makes colloidal stability especially hard to achieve for high-temperature nanofluids.

- **Viscosity**: is the resistance of a fluid to deformation against shear or traction stresses. The addition of solid particles to fluids usually means an increase of viscosity, whose extent depends on the concentration. If the viscosity increase caused by the addition of nanoparticles is of importance, a higher pumping power will be needed, increasing the cost of the whole hydraulic installation. Also, it is worth noticing that viscosity in liquids usually decreases with temperature, so this is a feature to be taken into account for HTFs.

- **Chemical compatibility between nanoparticles and base fluid**: interactions between the nanoparticles and the base fluids can take place. This can mean that morphological, compositional or corrosion related phenomena are occurring to the particles. These can be detrimental for the purpose of the nanofluid, so they need to be thoroughly studied and considered.

Although initially the biggest part of the research in this topic was conducted in order to develop nanofluids with an enhanced thermal conductivity to work as HTFs, the possibility to have increments in specific heat has made them also relevant for thermal storage purposes[18,25,26].

The two physical ways of storing thermal energy in a material are sensible and latent heat, as depicted in Figure 1.2, where the variation of the temperature over time for a material that is storing thermal energy is shown.
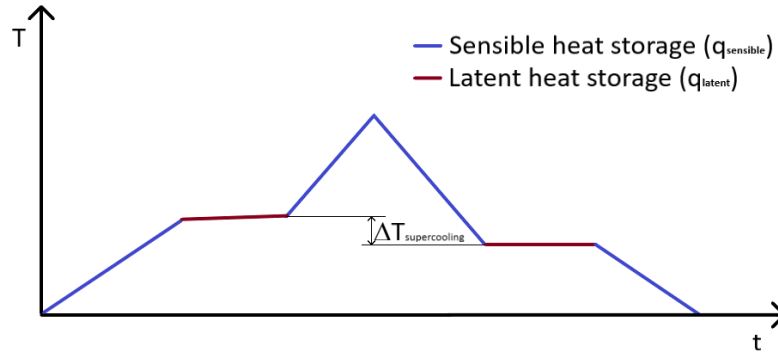
Figure 1.2. Physical thermal energy storage mechanisms.

Therefore, the thermal energy stored by a material can be defined as:

$$q_{total} = q_{sensible} + q_{latent}$$

During sensible heat storage, the temperature of the material is increasing. This is directly related to specific heat, so its enhancement would mean an increase in the sensible heat storage of the material. Moreover, during latent heat storage the energy is stored due to a phase change, without increasing the material temperature. Both of them can be defined according to Equation 1.2 and Equation 1.3.

$$q_{sensible} = m * c_p * \Delta T$$

$$q_{latent} = m * \Delta H_{fusion}$$

Therefore, improvements of the storage capacity of TES materials can be achieved by increasing its specific heat, but they are also possible to obtain due the contribution of latent heat, and thus have been researched through the use of phase change materials (PCMs).

1.3 PHASE CHANGE MATERIALS

PCMs are materials with a capacity of absorbing and releasing considerable amounts of energy during their change of state. The most common PCMs are based in melting and solidification cycles, so when the temperature rises the material absorbs an amount of energy necessary for it to melt. Once it is in liquid phase, when the temperature decreases the energy is released again to the surrounding medium, as the material solidifies. A complete melting-solidification cycle is illustrated in Figure 1.3.

The use of PCMs is something common and extended, and goes as far as putting ice into a drink, so the thermal energy needed to melt it is obtained from the surrounding liquid, that is consequently cooled down. The amount of heat needed to melt the material is directly related to its phase change enthalpy and equal to the amount of thermal energy that can be stored by latent heat.
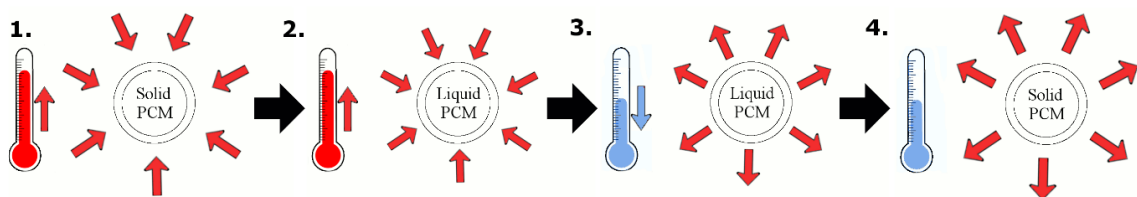
Figure 1.3. Functioning of a phase change material.

All these characteristics make phase change materials especially relevant for applications with thermal cycles, but also for their use as temperature regulators (during the energy absorption process of the phase change, the temperature increase is rather constant) and as thermal energy storage systems.

Besides water, materials susceptible to be used as PCMs range from paraffins and fatty acids to salt hydrates or metals. A simple diagram for the election of materials according to their melting temperature and phase change enthalpy is shown in Figure 1.4.
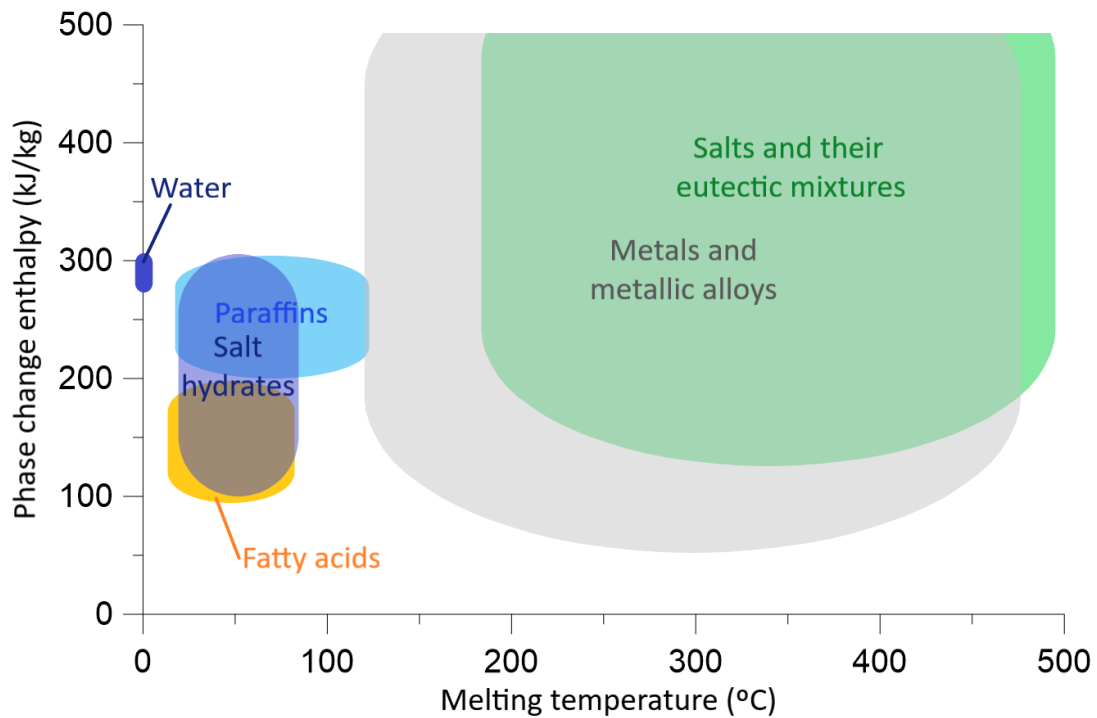
Figure 1.4. PCM types according to melting temperature and phase change enthalpy.

1.3.1   Use in nanofluids

Regarding the use of PCMs in nanofluids, they can be employed directly as the "base fluid", a material that is initially solid but melts during the process, with nanoparticles dispersed within it that can serve to promote its fusion or crystallisation; or as the solid phase, i.e. the solid nanoparticles.

In the case of PCMs introduced as the solid part of a nanofluid some difficulties are added. The first one of them is that the nanoparticles need some kind of encapsulation that prevents them from collapsing into each other when melted. If this encapsulation is not present, when the melted nanoparticles contacted each other, they would merge forming a bigger drop of PCM that no longer is on the nanometric scale and would cause the nanofluid to lose its properties.

In order to avoid this situation, two options are possible (see Figure 1.5): the first one is to introduce the nanoparticles in a higher melting-temperature material matrix, so they remain apart from each other no matter in which state they are [27,28]. The second option is to create core-shell structured nanoparticles, composed of a PCM nucleus and higher melting-temperature coating of a few nanometres surrounding it. This latter option is the most commonly used to introduce PCMs in nanofluids[29,30], however, achieving the presence of this shell is not always something trivial.
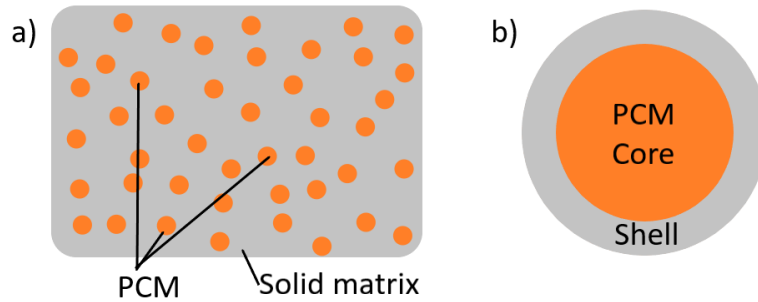
Figure 1.5. Types of PCM nanoencapsulation: (a) Solid matrix with PCM nanoparticles and (b) core-shell structure

Traditionally, encapsulating shells for nano- or micro-PCMs have consisted of a silica or polymeric coating chemically synthesised over the nuclei[29–33]. This synthesis processes usually involve several steps, making the production of core-shell nanoparticles quite complex.

Application of PCMs as micro or nanomaterials can be found in thermal regulators for comfort, such as in building materials or clothes[34–36]. However, when thinking about nanofluids, the microparticles present an additional disadvantage besides the already mentioned colloidal stability issues, since the encapsulating shell of the particles can break and cause clogging when passing through pumping systems or valves, whereas this can be avoided with nanoparticles thanks to their reduced size.

1.3.2 Metallic nanoencapsulated PCMs (nePCMs)

Among the materials that can be used as PCMs for thermal energy storage, metals present several advantages. They have high thermal conductivity, so they respond quickly to the temperature changes in the surrounding media, allowing for fast charge and discharge processes. Also, their high density compared with other materials makes it possible to have remarkable improvements in mass related properties (e.g. specific heat) with a not so high volumetric loading of particles (which are preferred to avoid a detrimental effect on the viscosity of nanofluids).

Moreover, the high melting temperatures of the metals make them suitable for their use in medium- and high-temperature nanofluids, and by using metallic alloys the temperature of the phase change can be almost custom-determined for the application. According to the melting temperature, the increase in the thermal storage capacity also takes place in a determined range of temperatures depending on the material, which can be very interesting for certain processes.

A phenomenon that frequently takes place in nePCMs and that needs to be considered, is the supercooling of the nuclei material, meaning that their crystallisation takes place at a temperature inferior to that of the melting[37,38]. This difference between the melting and crystallisation points is probably due to the purity and small size of the nuclei, that favours homogeneous crystallisation taking place. This type of crystallisation requires of more energy than heterogeneous one (when several nucleation spots are present), so it occurs at a temperature lower than that of the melting. The extent of that difference varies according to the material and size of the nuclei, ranging from a few degrees up to more than one hundred[38]. Although this peculiarity can be seen as a disadvantage when we think of pure thermal energy storage, since the energy will be released at a lower temperature than that was stored, causing loses, it can be of use in other several applications such as thermal barriers or air conditioning.

7

1.4 OBJECTIVES

The present thesis aims to contribute in providing deeper knowledge and developing effective solutions in the topics of heat transfer and thermal energy storage, by combining both nanofluids and phase change materials, for their application in medium- and high-temperature applications like CSP plants.

The main focus of the work is on developing nanofluids that present an enhanced heat storage capacity, making use of the latent heat inherent to phase change materials. In order to do so, the most common difficulties when using high-temperature nanofluids and nePCMs are also studied and dealt with through this thesis.

To overcome the problems related to the use of metals as nePCMs in thermal applications, the suitability of different ways of encapsulation that can suppose a simplification of the synthesis process is studied, and also the use of metallic alloys as a method of control of supercooling is proposed. Besides, as a method to test the behaviour of the synthesised nanofluids containing nePCMs, thermal characterisations at lab scale are performed, including thermal cycles of charge and discharge of the PCMs.

In order to deal with the issues associated with nanofluids working at high temperature, an experimental set-up to analyse colloidal stability of the suspended particles at high-temperature is developed, and the interactions between the base fluid and the nanoparticles are studied to ensure compatibility of the materials.

To evaluate the capacity of the nanofluids synthesised to enhance the thermal properties of commonly used base fluids, heat transfer properties and energy storage capacity are measured under different conditions, including their evolution through time. Variations in thermal conductivity and specific heat are studied, and the contribution of the nePCMs latent heat to the thermal storage capacity of the nanofluids is evaluated.

The partial objectives of the thesis, which allow to control and evaluate the development of nanofluids based on nanoencapsulated phase change materials, are the following:

- To achieve an enhancement of the heat transfer and thermal storage properties of the nanofluids based on nePCMs respect to the base fluids, working on different combinations of them for different temperature ranges.
- To develop at least one nanofluid based on thermal oil for medium-temperature applications and one based on solar salt for high-temperature applications, including metallic nePCMs specifically selected for each one of them.
- To test the suitability of the natural oxide encapsulation found in many metallic nePCMs, consisting on a passivating layer that is naturally formed when exposed to oxygen, to act as a shell to contain the pure metal in the core of the particles when immersed in the fluid and under working conditions.
- To control the extent and effects of supercooling, in order to make possible the management of the absorption and release of thermal energy by the PCM according to the application.
- To develop a procedure for the thermal characterisation of these nanofluids under different conditions of operation, including thermal cycling.
- To build an experimental set-up to study colloidal stability of the nanofluids at high-temperature, controlling the size of the particles and their evolution through time in terms of aggregation or settling.

- To study the influence of temperature and time over the colloidal stability of nanofluids.
- To test the suitability of mechanical redispersion to bring the agglomerates and settled particles to their initial state, as a method to mitigate the negative effects of the lack of colloidal stability.
- To study the behaviour of multi-coated nanoparticles, with a second encapsulating layer, in terms of preservation of their thermal storage capacities.
- To provide new knowledge and go a step forward in the enhancement of heat transfer fluids and thermal energy storage materials by using nanofluids.

A summary of the main and specific goals of this thesis, and the extent of their study on each chapter is presented in Table 1.1.

Table 1.1. Summary of the challenges related to nanofluids based on nePCMs faced in each chapter. ● Represents issues that are thoroughly studied in the chapter and ○ issues that are studied in a less deep manner.

Difficulty	Chapter 4	Chapter 5	Chapter 6	Chapter 7
Overcoming problems related to the use of metals as nePCMs in thermal applications				
• **Synthesis of an encapsulating shell**	●	○		●
• **Supercooling**	●	○		
• **Thermal stability**	○	○		●
Overcoming issues associated with nanofluids at high-temperature				
• **Colloidal stability**			●	
• **Interactions between components**	○	○	●	○
Creating nanofluids that enhance the thermal properties of the base fluid				
• **Thermal conductivity**	○	○		
• **Thermal storage capacity**	○	●		●

Chapter 2: STRUCTURE

Considering the goals set for this work in the previous chapter, a breakdown of the results presented in the following chapters is provided next, detailing the topics that will be covered in each one of them.

- Chapter 3: Methodology and characterisation techniques.

  In this chapter, the processes followed for the synthesis of the different nanofluids and nePCMs is described, along with the techniques and methodology used to characterise them in terms of morphology, composition, colloidal stability, thermal properties and performance as HTF or TES material.

- Chapter 4: Nanofluid based on self-nanoencapsulated metal/metal alloys phase change materials with tuneable crystallisation temperature.

  This chapter deals with the synthesis of a medium-temperature nanofluid based on a commercially used thermal oil (Therminol 66). Metallic nePCMs (Sn) are used as the solid phase. Suitability of the naturally formed oxide encapsulation and its compatibility with the base fluid are studied, including thermal cycling conditions. The increase of the thermal properties such as thermal conductivity and heat storage capacity is measured.
  A method to control the extent of supercooling is developed, using metallic alloys on the peritectic region.

- Chapter 5: Thermal energy storage of molten salt-based nanofluid containing nanoencapsulated metal alloy phase change materials.

  In this chapter, a nanofluid composed of Al/Cu nePCMs and solar salt as the base fluid for high-temperature applications is synthesised and characterised. The main issues

like oxide encapsulation suitability, supercooling extent, compatibility between the components and resistance to thermal cycling are validated. Enhancements of the thermal storage capacity are reported.

- Chapter 6: Colloidal stability of molten salt-based nanofluids: dynamic light scattering tests at high temperature conditions.

  This chapter deals with the problem of measuring colloidal stability at high temperature. A dynamic light scattering (DLS) system is set up for the measurements of particle/cluster size evolution through time as a means to measure colloidal stability. After the calibration of the set-up and a theoretical analysis, stability and redispersion measurements are performed in solar salt-based nanofluids at high temperature. In order to analyse how the interactions between the nanofluid components, different combinations of base fluids and nanoparticles are studied in terms of colloidal stability.

- Chapter 7: Improved thermal energy storage of nano-encapsulated phase change materials by atomic layer deposition

  In this chapter, a second encapsulation layer is synthesised on metallic nePCMs by using atomic layer deposition. The performance of the multi-layered nanoparticles is studied in terms of stability of their properties when submitted to thermal cycling. A nanofluid based on solar salt is synthesised using the multi-layered nePCMs (Sn@SnO$_x$@SiO$_2$ and Sn@SnO$_x$@Al$_2$O$_3$), and the effects of the second coating on the interactions between particles and base fluid are studied. The nanofluids are characterised as thermal energy storage materials, showing an enhancement respect to the base fluid.

- Chapter 8: General discussion and conclusions.

  This chapter offers an overview of the goals achieved through this thesis. A summary of the main challenges faced in the development of nanofluids based on nePCMs is provided, along with a detailed breakdown of the specific goals that have been accomplished in the thesis.

- Chapter 9: Gaps and future research.

  In this chapter, possible research lines to continue with the work presented here are proposed, covering the remaining gaps left and stablishing potential innovations that could be looked into in order to follow the findings of this thesis.

Chapter 3: Methodology and characterisation techniques

When talking about the properties of nanoparticles or the synthesis of nanofluids, it is necessary to take into account that the mechanisms defining them might not be the common ones for macroscopic matter. Some of the assumptions and simplifications that are often made for bulk materials do not work when applied to nanometric stuff and therefore, special attention should be put in the methodology and characterisation techniques employed. A summary of the experimental methods used in this work has been included in Table 3.1 by the end of this section.

3.1 Synthesis methods

3.1.1 Water- and thermal oil-based nanofluids

Nanofluids that used water and a commercial thermal oil as the base fluid have been used in this work. The synthesis process consisted in adding the desired amount of nanoparticles in each case to the base fluid. Proper dispersion of the nanoparticles was then assured by sonicating the samples with an ultrasonic probe operating at 200 W for 3-5 min.

In the case of the oil-based (Chapter 4), the characterisation performed covered an initial approach to the thermal properties of the nanofluid, studying only the static case without analysing their time evolution. No surfactants or stabilising agents were included in the oil-based nanofluids for this reason. In the case of the water-based nanofluids in Chapter 6, the aim was to make a comparison of nanofluids based on different base fluids, and since no surfactant could be used for the high-temperature nanofluids due to temperature restrictions, surfactants were also not added to the water-based ones.

3.1.2   Molten salt-based nanofluids

Two different molten salts have been used in this work as base fluids, $CaNO_3$ and a mixture of sodium and potassium nitrates known as solar salt. $CaNO_3$ melts at 40 °C, so the synthesis of this nanofluid is similar to the explained for oil and water-based ones, mixing the nanoparticles with the base fluid and sonicating to disperse them. However, this nitrate also presents high deliquescence, that is the tendency to absorb water from the environment, and thus special care had to be taken to preserve from moisture by keeping the sample in an oven at 80 °C during the whole synthesis process.

Solar salt, used in Chapter 5, Chapter 6 and Chapter 7, is the mixture of 60 wt.% of $NaNO_3$ and 40 wt.% of KNO_3. The nitrates were also kept in an oven to remove any possible moisture before starting with the nanofluids synthesis. $NaNO_3$ and KNO_3 were grounded together in a mortar in the desired proportions and then the nanoparticles were added. The melting temperature of solar salt is around 220 °C, so the nanofluid cannot be sonicated to disperse the nanoparticles. However, after adding the nanoparticles, the solid mixture with the salts was grounded in a mortar until achieving a homogeneous powder and then the sample was melted and the nanofluid was mixed with a mechanical stirrer at 1000 rpm, just before quickly cooling the sample again in the shape of pellets for its subsequent characterisation.

3.1.3   Atomic layer deposition (ALD)

An additional oxide coating has been synthesised on the nePCMs in Chapter 7. Atomic layer deposition bases its working principle in cyclically exposing a surface to two different precursors, with purge steps between them. The active groups in the surface react with the first one and create new active groups that will react with the second one, theoretically resulting in the formation of a monolayer of the coating material on the initial surface. The larger the number of cycles applied, the thicker the layer of deposited material will be. Coatings of SiO_2 and Al_2O_3 were synthesised using an ALD set-up for small particles. The reactor consisted of a glass column placed on a vibrating table that, along with the constant nitrogen flow, serves to fluidise the particles in order for the precursors to be able to reach all the surface available. The details for each experiment are explained in Chapter 7.

3.2   MORPHOLOGICAL CHARACTERISTICS

When dealing with nanometric matter, special techniques are required for direct visualisation of the samples. The shape, size or spatial distribution of the nanoparticles within a sample are not discernible to the naked eye, and so more sophisticated instruments are needed for the analysis of these properties.

Electron microscopy techniques have been used to visualise the different nePCMs. These techniques base their functioning in the emission of an electron beam over a sample, whose shape and trajectory are controlled by electromagnetic and electrostatic lenses, and the subsequent analysis of the electron-matter interactions. The main difference among the most common microscopes is the way in which these interactions are analysed after.

Besides the detailed visualisation of the nanoparticles, electron microscopy also offers the possibility of capturing a more general view of a nanoparticle population, allowing to obtain the particle size distribution of a sample by analysis of the images.

3.2.1 Scanning electron microscopy (SEM)

In scanning electron microscopes the electron beam impacts on the surface of the sample. The accelerated electrons interact with the atoms in the surface and are scattered. The detected signal from the reflected electrons is analysed and provides information about the topography and composition of the sample surface. For the external examination of nePCMs, a scanning electron microscope JEOL-JSM 6510 has been used in Chapter 5 and Chapter 7.

3.2.2 Transmission Electron Microscopy (TEM)

In transmission electron microscopy, the electrons analysed after hitting the sample are the ones that have passed through it. The information obtained is therefore of the internal structure of the sample, such as crystal structure, morphology or stress state. In TEM, materials with different densities are visualised as different intensities of grey, since the amount of electrons that pass through the materials depends on their density. Therefore, transmission electron microscopy has been of special relevance in this work, since it makes very easy to visualise the different materials composing the shell and cores of nePCMs. Two microscopes, JEOL-JEM 2100 and Philips CM200 (that included the possibility of visualisation at high temperature), have been used through this work, along with a Field Emission TEM (JEOL-JEM 2100F) that allows ultrahigh resolution in scanning transmission microscopy due to its field emission electron gun.

3.2.3 Scanning transmission electron microscopy (STEM)

Scanning transmission electron microscopes combine both techniques mentioned. They allow to obtain images from transmitted electrons (like TEM does) and also to focus the electron beam in a very small spot and move it through the sample (like SEM does), so in the end, the image is obtained from a point-by-point mapped analysis. A STEM FEI TALOS F200X was used in Chapter 4 for the visualisation of Sn/Pb nePCMs.

3.3 COMPOSITION

Different techniques for the determination of the samples chemical composition have been used. Some of them are usually paired with electron microscopy, such as Energy-dispersive X-ray spectroscopy or electron energy loss spectrometry, which allows to analyse composition in a very precise spot of the sample in some cases. Other techniques, such as X-ray diffraction, inductively coupled plasma optical emission spectroscopy or Fourier-transform infrared spectroscopy deal with the samples as a whole and provide results of the general composition of the sample.

3.3.1 Energy-dispersive X-ray spectroscopy (EDX)

This technique is based on the principle that each element has its own atomic structure, so when excited by an electron beam they emit X-rays of a specific energy, forming a unique set of peaks on its electromagnetic emission spectrum for each element. Electron microscopes already have an electron beam that can act as the excitation source needed for EDX, so adding an X-ray detector and analyser system, EDX is easily performed. In Chapter 4, Chapter 5 and Chapter 7, EDX analysis modules from Oxford INCA paired to the transmission electron microscopes (JEOL-JEM 2100 and JEOL-JEM 2100F) have been used for qualitative elemental analysis of the samples.

3.3.2   Electron energy loss spectrometry (EELS)

In electron energy loss spectrometry the inelastic interactions between the electron beam and the sample materials are analysed. When an electron interact inelastically with a material part of its energy is lost and its path is slightly deflected. By analysing these changes, in combination with the spatial resolution of STEM, the elements composing a sample can be determined very precisely, along with their electronic structures or the nature of their bonds. An EELS analysis module paired to the STEM FEI TALOS F200X has been used to obtain a spatial composition analysis of the Sn/Pb nePCMs in Chapter 4.

3.3.3   X-Ray powder diffraction (XRD)

In order to obtain qualitative information about the crystalline structure and chemical composition of nanoparticles, X-Ray powder diffraction is one of the preferred techniques. Crystalline materials have their atoms arranged in periodical structures with interatomic distances that depend on the material. Consequently, it is possible to determine the composition of a crystalline material by analysing the angles and intensities of the diffracted beams after an X-ray beam has incised on it. The crystalline phases of the metallic nePCMs and their metallic oxide shells have been determined with a XRD Bruker D8 spectrometer in Chapter 4 and Chapter 7.

3.3.4   Inductively coupled plasma optical emission spectroscopy (ICP-OES)

In optical emission spectroscopy, atoms in their fundamental state are excited to higher energetic states. In ICP-OES, this is achieved through an inductively coupled plasma torch. The excited atoms are not stable and when they go back to their fundamental states, they emit the absorbed energy as electromagnetic radiation with a characteristic wavelength according to the electronic configuration of each element. Moreover, the intensity of the radiation is proportional to the amount of element in the sample, so this technique allows for the quantification of elemental composition when the radiation detected is correlated to calibration curves. ICP-OES has been used in Chapter 7 to quantitatively determine the amount of material deposited in the nePCMs by ALD.

3.3.5   Fourier-transform infrared spectroscopy (FT-IR)

Absorption infrared spectroscopy is used to qualitatively determine the molecular structures according to the IR radiation absorption of their molecular vibration. The vibrational spectrum of a molecule is considered a unique property, characteristic of that particular molecule, so it can be used to identify the composition of a sample when comparing to reference standards. The spectrum is obtained by processing an interferogram using the Fourier transform, which allows for a higher spectral resolution data collection than with the traditional dispersive spectroscopy, in which wavelength is slowly increased while the spectrum is recorded. FT-IR has been used to analyse the composition of the coatings in Chapter 7.

3.4   COLLOIDAL STABILITY AND SIZE

Particle aggregation and colloidal stability play a key role in nanofluids, as a proper dispersion of the particles is needed in order to maintain the enhanced properties acquired with the addition of nanoparticles. Several experimental methods are commonly used in the literature to determine the temporal evolution of stability, such as direct visualisation or dynamic light scattering, which give meaningful information about the sedimentation or aggregation of the nanoparticles.

3.4.1 Direct visualisation

In order to analyse the colloidal stability of nanofluids, one of the commonly used methods is their direct visualisation at different intervals of time, especially in high-temperature nanofluids, given the common restrictions in the state-of-the-art instruments.

The procedure used for this purpose in Chapter 6 consisted of a set up with a high temperature cuvette, a camera and a LED lighting system, as shown in Chapter 6. When the nanoparticles are evenly dispersed within the nanofluid, its degree of transparency is uniform. However, if the nanofluid is not stable and the nanoparticles start forming clusters and settling, they concentrate in the bottom part of the nanofluid, increasing its opacity and appearing darker on the camera, whereas the upper part, now with a lower concentration of nanoparticles, increases its transparency showing a brighter image on the camera. Therefore, by periodically taking pictures of the sample, this evolution of light transmission can be evaluated and qualitatively associated with the colloidal stability of a nanofluid.

3.4.2 Dynamic light scattering (DLS)

Dynamic light scattering is a technique commonly used to measure particle size distribution in suspensions. Its working principle relates the random movement of the nanoparticles suspended in a fluid, also known as Brownian motion, to the size of the particles. When a laser beam at a specific wavelength irradiates a sample, the Brownian motion of the particles causes temporal fluctuations in the scattered light intensity. By analysing these fluctuations in the timescale they occur, information about the speed at which the particles move into a solution can be obtained. Smaller particles move faster than bigger ones, so in the end the hydrodynamic radius can be calculated according to the Stokes-Einstein equation (Equation 3.1).

$$D = \frac{k_B T}{6\pi\eta R_H}$$

Equation 3.1

where D is the translational diffusion coefficient, related to the speed of the particles, k_B is the Boltzmann constant, T is the temperature, η is the viscosity of the fluid and R_H is the hydrodynamic radius.

The hydrodynamic radius correspond to the radius of a hard sphere that will diffuse light in the same manner as the particle analysed, but in practice, the examined particles are not hard spheres. Moreover, when dealing with colloidal stability, the diffusing object can even be a cluster of several nanoparticles. Therefore, the hydrodynamic radius is used to compare the sizes of well dispersed particles or different levels of particle aggregation or their evolution, when talking about colloidal stability.

Two different DLS instruments have been used in Chapter 6 and Chapter 7 for this purpose. The ZetaSizer Nano ZS, from Malvern Instruments Ltd. is a commercial device, commonly used in the literature, which measures the intensity of the backscattered light at 173° and allows the analysis of samples up to 90 °C. Additionally, a high temperature DLS set-up was developed through the work with a VASCO FLEX Particle Analyzer from Cordouan Technologies. The set-up consisted in the DLS emitter and receiver, all contained in the same portable laser head that registers the light backscattered at an angle of 170°, and a heated steel cuvette that has two see-through quartz windows. The temperature of the sample in the cuvette can be then controlled by a heating ring and two K-thermocouples up to 500 °C, as it is depicted in Figure 3.1.
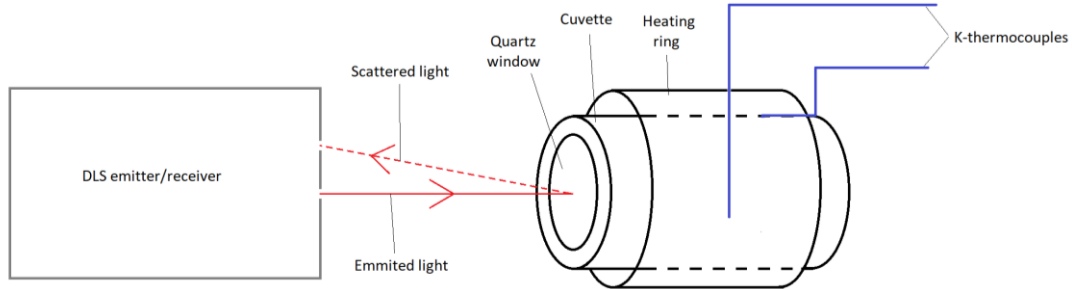
Figure 3.1. Scheme of the external DLS set-up for high temperature measurements.

3.4.3   Zeta potential

When a charged particle is in a colloidal suspension, ions of the medium adhere to its surface creating a double layer compensating its charge, so the particle appears to be electrically neutral from a great distance. Zeta potential is the electrical potential difference between a point in the dispersion fluid away from the particle and the stationary layer of fluid attached to it, namely, the slipping plane in the interfacial double layer.

Zeta potential is commonly used as an indicator of the stability in colloidal dispersions. Its value is proportional to the electrostatic repulsion between charged particles in a solution. Therefore, a high zeta potential means low possibility of aggregation, and thus, high colloidal stability; whereas if the potential is small, the attractive forces between the particles may exceed this repulsion and they will aggregate into clusters. A ZetaSizer Nano ZS from Malvern Instruments Ltd. has been used to study stability behaviour in Chapter 6.

3.5   THERMAL STABILITY AND PROPERTIES

The main thermal properties to study in heat transfer fluids and thermal energy storage materials are thermal conductivity, specific heat, and phase change enthalpy, in the case of processes with a phase change. Both specific heat and enthalpies can be determined by differential scanning calorimetry, whereas several methods, like transient hot wire and laser flash analysis can be used to calculate thermal conductivity. Stability of the enhanced thermal properties through heating-cooling cycles is another issue that needs to be taken into account in nanofluids for thermal applications, and besides differential scanning calorimetry, thermogravimetrical analysis can serve to determine the resistance of the materials integrity at high temperatures.

3.5.1   Differential scanning calorimetry (DSC)

In differential scanning calorimetry a sample and a reference are heated or cooled in order to maintain or reach a certain temperature. The differences in the heat flux needed for both crucibles are registered, allowing to determine several thermal particularities of the sample by comparing it to the reference.

According to the working principle of the technique, when a physical transformation such as a phase change or phase transition takes place in the sample, a higher or lower heat flow supply is needed to keep the sample at the exact same temperature of the reference. Thus, for endothermic processes in which the sample absorbs heat, like fusion, the amount of heat supplied to the sample should be higher than the supplied to the reference and, as opposite, in

exothermic processes like crystallisation, it should be smaller. Apart from state changes, differential scanning calorimetry also allows for measuring glass transition temperatures, and for quantifying the amount of thermal energy stored or released during any of these changes, making possible to determine the transition enthalpies associated to these processes. Also, if the differences in the heat flux are referenced to a material with a known specific heat capacity, it is possible to determine this property. A DSC2 from Mettler Toledo, with a maximum operating temperature of 700 °C, has been used to analyse the thermal behaviour of different nePCMs (phase change temperatures and enthalpies, specific heat and resistance to thermal cycling) in Chapter 4, Chapter 5 and Chapter 7, using 40 µl aluminium crucibles.

3.5.2   Transient hot wire (THW)

Among the techniques used to measure thermal conductivity, the transient hot wire method is one of the most commonly used. A probe containing an electrically insulated thin wire, which acts as both the heater and temperature sensor, is introduced in the sample. A voltage step is applied to this wire and the transient temperature rise on it is recorded. According to the heat flux and the temperature increase evolution with time it is possible to determine the thermal conductivity of the sample. A KD2Pro conductimeter from Decagon Devices, with a maximum operation temperature of 150 °C, has been used in Chapter 4 to characterise oil-based nanofluids.

3.5.3   Laser flash analysis (LFA)

Laser flash analysis is a method used to determine thermal diffusivity of materials. A pulse of energy is applied to the flat side of a thin sample and the energy received on the opposite side is recorded. Thermal diffusivity is then calculated according to the velocity with which the energy has reached the backside of the sample. For materials with higher thermal diffusivity, the energy supplied by the laser pulse is transmitted much faster than for materials with low thermal diffusivity. Knowing also the specific heat capacity and density of a sample, its thermal conductivity can be calculated. As one of the advantages of laser flash analysis is that it can be used for a broad range of temperatures, a LFA427 from Netzsch, with a range of operation temperatures from -120 °C to 1600 °C, has been used in Chapter 5 to analyse thermal diffusivity and determine thermal conductivity in molten salt-based nanofluids, using a platinum crucible coated with graphite.

3.5.4   Thermogravimetrical analysis (TGA)

This technique measures the mass evolution of a sample when subject to controlled temperature variations. The sample is heated into a crucible made of an inert material (e.g. platinum or alumina) while the sample holder is coupled to a microbalance registering the mass changes. Decomposition, oxidation, dehydration processes and any other transformation that implies a lost or addition of materials can be studied through thermogravimetrical analysis. Besides, when the sample is composed of several materials with different decomposition patterns, it can be used to determine the composition of the sample. A TGA1 from Mettler Toledo, with a maximum operation temperature of 1100 °C, has been used in Chapter 7 in order to analyse the oxidation behaviour of nePCMs.

Table 3.1. Summary of the experimental techniques and devices used in this work.

Technique	Equipment	Chapter 4	Chapter 5	Chapter 6	Chapter 7
SEM	JEOL-JSM 6510		●		●
TEM	JEOL-JEM 2100	●	●	●	
	JEOL-JEM 2100F				●
	Philips CM200	●			
STEM	FEI TALOS F200X	●			
EDX	Oxford INCA	●	●		●
EELS	-	●			
XRD	Bruker D8	●			●
ICP-OES	PerkinElmer Optima 5300DV				●
	PerkinElmer Optima 4300DV				●
FT-IR	Jasco 6200				●
Direct visualisation	-			●	
DLS	Malvern ZetaSizer Nano ZS			●	
	Cordouan VASCO FLEX			●	●
Zeta potential	Malvern ZetaSizer Nano ZS			●	
DSC	Mettler Toledo DSC2	●	●		●
THW	Decagon KD2 Pro	●			
LFA	Netzsch LFA427		●		
TGA	Mettler Toledo TGA1				●

Chapter 4: NANOFLUID BASED ON SELF-NANOENCAPSULATED METAL/METAL ALLOYS PHASE CHANGE MATERIALS WITH TUNEABLE CRYSTALLISATION TEMPERATURE

Nanofluids using nanoencapsulated phase change materials (nePCM) allow increments in both the thermal conductivity and heat capacity of the base fluid. Incremented heat capacity is produced by the melting enthalpy of the nanoparticles core. In this work two important advances in this nanofluid type are proposed and experimentally tested. It is firstly shown that metal and metal alloy nanoparticles can be used as self-encapsulated nePCM using the metal oxide layer that forms naturally in most commercial synthesis processes as encapsulation. In line with this, Sn@SnO$_x$ nanoparticles morphology, size and thermal properties were studied by testing the suitability and performance of encapsulation at high temperatures and thermal cycling using a commercial thermal oil (Therminol 66) as the base fluid. Secondly, a mechanism to control the supercooling effect of this nePCM type based on non-eutectic alloys was developed.

4.1 INTRODUCTION

The thermal properties of heat transfer fluids (HTFs) play a key role in the efficiency of thermal-based industrial processes such as electricity generation, oil and gas processing, chemical industry, and manufacturing processes, among others. From the environmental perspective, improving the efficiency of thermal systems is crucial since 90% of the world energy budget centres on heat conversion, transmission and storage. Minor improvements in the efficiency of thermal systems can significantly reduce CO_2 emissions[39,40].

Thermal oils, glycols and molten salts are used as HTFs in medium- and high-temperature applications because they present good thermal stability under high-temperature conditions. However, the thermal properties of these HTFs are quite poor, with thermal conductivity (k) and specific heat capacity (c_p) values below 0.4 W/m·K and 2.5 J/g·K, respectively. Nanofluids are defined as engineered colloidal suspensions of nanoparticles in a base fluid. Nanofluids allow a solid to be introduced into a liquid, transferring to some extent the solid thermal properties to the liquid and keeping, also to some extent, its liquid transport properties. Therefore, nanofluids present an effective route to improve HTFs thermal properties[41,42].

The earliest nanofluid works were related to thermal conductivity enhancement using water as the base fluid[12,13,43]. Afterwards, nanofluid-related research topics were extended and nanofluid viscosity and specific heat were involved[44]. Nanofluid thermal and rheological properties depend on the base fluid but, broadly speaking, it is possible to observe for a certain base fluid, nanoparticle morphology and a given nanoparticle concentration value, a more marked increment in viscosity than that in thermal conductivity. In non-ionic fluids, a slight drop in the specific heat of the nanofluid is also expected[45]. A few industrial applications exist in which nanofluids with such physical properties can be found of interest[46].

From 2010, new nanofluid approaches that use additional solid particle properties have been investigated. One of them is to use nano-encapsulated phase change materials (nePCM) as the solid phase. In this approach, nanoparticles have a solid-liquid PCM core and a high melting temperature shell that keeps the PCM confined when in the liquid phase. Use of nePCM allows both the thermal conductivity and heat capacity of the base fluid to increase by the latent heat contribution of nePCM cores. Metal and metal alloy nanoparticles can be used as nePCM cores suitable for medium- and high-temperature applications. Metal and metal alloy nanoparticle melting and crystallisation temperatures and enthalpies have been studied in detail in recent years. In most cases, encapsulation is obtained by inserting nanoparticles into a high melting temperature matrix[27,28,37,47–50], or by growing a silica[29,32,33,51–53] or trioctyl phosphine oxide TOPO[30] shell around them. Different metal cores have been investigated: indium[27,32,37,51], bismuth[27,28,37,47,50], tin[27,29,33,37,52,53], cadmium[27], lead[27,49], zinc[30], and their alloys[48,50,54]. Generally speaking, if metal cores are lower than 50 nm, lowering melting temperature and melting and crystallisation enthalpy values than those measured in the bulk material are observed due to the substantial contribution of the metal atoms near the shell[55,56]. In addition, lower crystallisation temperature values, defined as supercooling, are always found for these small nePCMs. The purity of the materials in the core and their small size prevent heterogeneous crystallisation as there are no nucleation spots inside the nuclei. Thus, homogeneous nucleation takes place for crystallisation at a lower temperature. The nePCM supercooling temperature depends on the nucleus material and size.

One important parameter in shell-type nePCM is the encapsulation ratio, which is defined as the ratio between the phase change enthalpy per unit of mass of nePCM and that of the PCM

bulk material. Encapsulation ratios below 1 are due to both the mass contribution of the nePCM shell, which does not melt within the working temperature range of nePCM, and the reduced enthalpy due to size effects (only for nePCM whose nuclei are smaller than 50 nm). In order to maximise the nePCM latent heat contribution, the encapsulation ratio should be as high as possible, assuring shell mechanical integrity.

Regarding the shells that surround nePCM cores, silica and TOPO shells have been previously used in nePCM-based nanofluids, where a wide range of base fluids, such as methanol[32], molten salt[29,30], poly-alpha-olefin (PAO)[51] and commercial thermal oil (Therminol 66)[33], have been used.

NePCMs offer considerable advantages over conventional nanoparticles, such as major and better controlled heat capacity increments. However, two main drawbacks limit their application in nanofluids. On the one hand, complex chemical synthesis processes are needed to obtain shell-type nePCM, which involve at least four chemical processes: one to produce metal nanoparticles, a second one to grow a polymeric template around them, a third one to grow the silica or TOPO shell on the template, and a final one to eliminate the polymeric template. On the other hand during the heat transfer process, nePCM cores should be melted and crystallised. Therefore, the difference between HTF charge and discharge temperatures should at least be the same as between the melting and supercooled crystallisation. This way, supercooling limits the impact of the nePCM latent heat contribution to the heat capacity of the base fluid, as the energy absorbed in the charging stage of the process will be released at a lower temperature in the discharge.

In this work, two new approaches to overcome the drawbacks of nePCM are proposed and experimentally checked. It is firstly shown that a metal oxide shell is produced during the metal nanoparticle fabrication process by standard commercial methods, which can be used as self-encapsulation for static and dynamic conditions to avoid complex chemical processes to create shell-type nePCM. It is secondly shown that non-eutectic metal alloy cores can eliminate the supercooling effect by using solid-phase remainders as nucleation spots during the crystallisation process. This latter approach, along with the proper alloy composition selection and a known value of the maximum working temperature of the HTF, enables a form of thermal management of the nePCM inside HTFs with a tuneable discharge temperature.

4.2 METHODS

4.2.1 NePCM preparation
Two types of nePCM were tested:

a) Commercial Sn nanoparticles of nominal sizes 60–80 nm and <300 nm were purchased from US Research Nanomaterials, Inc. These nanoparticles were produced by the electrical wire explosion method[57] and the electro-physical fumed[58] method, respectively.

b) In-house Sn/Pb alloy nanoparticles were synthesised using a modified polyole wet-chemical reduction process[53]. In a typical synthesis, 3.3 g of polyvinylpyrrolidone (PVP) (MW 40000, Sigma Aldrich) were dissolved in 55 ml of tetraethylene glycol (TEG) (99%, Sigma Aldrich) and heated to 140 °C. Then a $SnCl_2$ solution (1.03 g in 12 ml of TEG) was added slowly to the reaction mixture. The PVP solution turned yellow-brown after adding the $SnCl_2$ solution. Ten minutes later, a freshly prepared $NaBH_4$ (99%, Sigma Aldrich) solution (1.3 g of $NaBH_4$ in 15 ml of TEG) was added drop-wise to the reaction solution.

Next a $PbCl_2$ solution (0.115 g in 15 ml of TEG) was added. After 90 min, heat was removed and the solution was brought to room temperature. The reaction time and the amount of PVP allowed nanoparticle size distribution to be controlled. The entire synthesis was carried out with constant magnetic stirring with the protection of a N_2 atmosphere. Sn/Pb nanoparticles were washed 3 times with ethanol, twice with distilled water and separated out by centrifuging.

4.2.2 Nanofluid preparation

Nanofluids were prepared by adding nePCM to synthetic thermal oil HTF TH66 (Solutia, Inc.) at a 30% mass concentration. TH66 maximum operating temperature is 340 °C and 250 °C under closed circuit conditions and open conditions, respectively. The mixture was homogenised by sonication using a Sonopuls HD2200 (Bandelin) ultrasound probe in a 100% duty cycle for 5 minutes.

4.2.3 NePCM and nanofluid characterisation

The size and morphology of the Sn and Sn/Pb nePCM were determined by direct observation under a field emission transmission electron microscope (TEM, JEOL-JEM 2100) that operated at an accelerating voltage of 200 kV. The existence of the encapsulating oxide layer was also confirmed, and the analyses of the structure and qualitative differences in the composition of the core and shell were performed using the same microscope, which includes High-Resolution and EDX (Oxford INCA) analysis modules.

The quantitative determination of both the composition and the crystalline structure of the oxide layer were determined by X-Ray diffraction (XRD) using a Bruker D8 X-ray diffractometer with Cu Kα radiation by studying the angles from $2\theta = 10°$ to $2\theta = 70°$ with a 0.02° step.

The thermal study to evaluate the melting and crystallisation temperatures and the associated enthalpies, existence of supercooling and thermal cycling to test their evolution through time and use was performed in a differential scanning calorimeter (DSC2 Mettler Toledo). The Sn nePCM and nanofluid samples were subjected to 200 thermal cycles each, between 70 and 280 °C with 40 °C/min heating and cooling rates, and 5-minute isotherms at maximum and minimum temperatures. Every 20 cycles, a more detailed analysis was done with the same temperatures and isotherms, but with heating and cooling rates of 5 °C/min, to obtain the values of the melting and crystallisation temperatures and enthalpies.

The encapsulation ratio was calculated comparing the enthalpy/mass ratio obtained in the DSC analysis to that expected from the core bulk material, and also mathematically, according to the nuclei volume/ total particle volume ratio, where the shell thickness values were obtained from the TEM images.

The resistance of the encapsulating layer to high temperatures was tested by a high-temperature transmission electron microscope (HT-TEM, Philips CM 200) by obtaining images with the 70–300 °C range.

Encapsulation breakage was achieved using DSC, with a thermal cycle between 70 °C and 400 °C, and with 40 °C/min heating and cooling rates and 5-minute isotherms at maximum and minimum temperatures.

The specific heat of the nanofluid was obtained using DSC dynamic method. Applying a known heating rate to the sample the specific heat can be calculated, since the heat flux measured by the DSC is directly related to specific heat, sample mass and heat rate applied.

Thermal conductivity was measured using the transient hot wire technique (KD2Pro, Decagon Devices) for 50 °C and 100 °C. The samples were put in a vial and submerged in a thermostatic bath to ensure temperature stability within the measurements.

The composition details of the Sn/Pb alloy nePCM were obtained with a scanning transmission electron microscope (STEM FEI TALOS F200X) and an EELS system, which allows the composition of sample atom by atom to be determined.

4.3 RESULTS AND DISCUSSION

4.3.1 Self-nanoencapsulation by a metal oxide layer

Nanoparticle size distribution was evaluated for two commercial Sn nanoparticle types, one with a nominal size of 60–80 nm and the other with one of <300 nm, as seen in Figure 4.1. Depicted size distribution shows that the mean diameter of nanoparticles is larger than the value provided by the supplier, especially for the Sn 60–80 nm sample. Both samples particle size follows a lognormal distribution, centred on 103 nm for commercial 60–80 nm nanoparticles, and on 184 nm for commercial <300 nm ones. The presence of the shell covering the metallic nucleus is seen as a slightly paler layer in both images (Figure 4.1 (a and b)). The XRD performed for both samples (spectra are shown in Supplementary Figure 4.1) shows only crystalline pure Sn from the nePCM core, which proves the initially amorphous nature of these metal oxide shells.
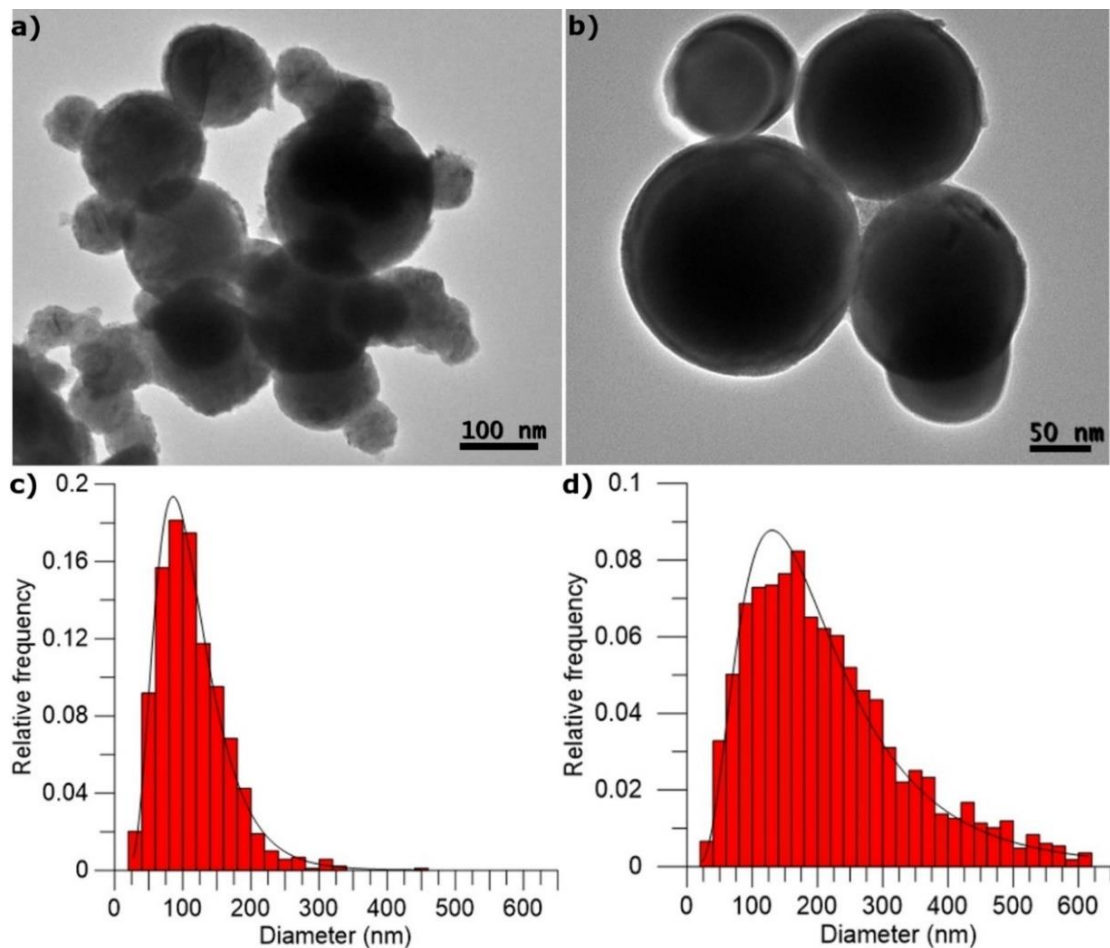
Figure 4.1. Comparison of the properties of the two samples, Sn of nominal size 60–80 nm and <300 nm. TEM image of Sn (a) 60-80 nm and (b) <300 nm. Size distribution of Sn (c) 60-80 nm and (d) <300 nm.
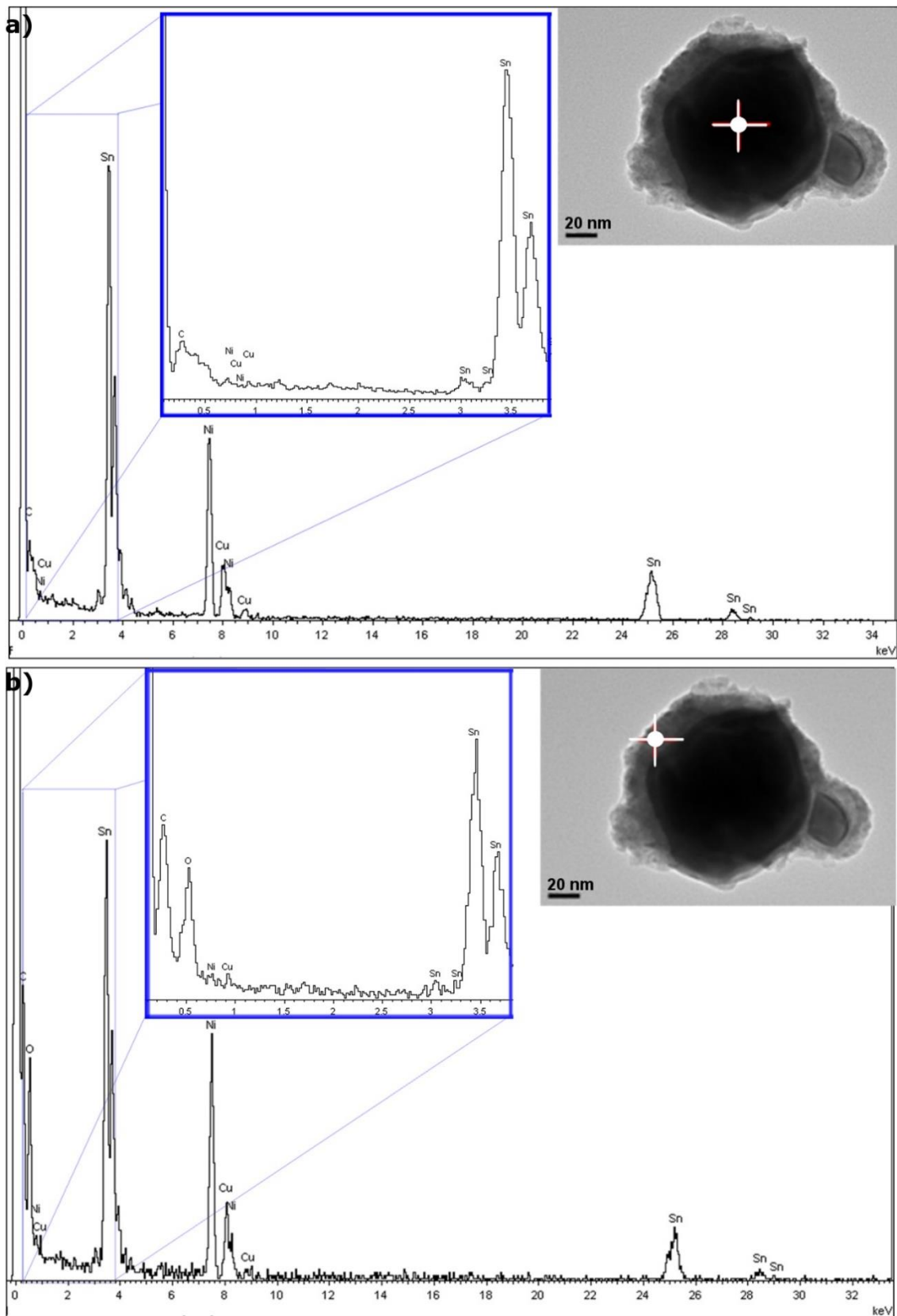
Figure 4.2. EDX analysis of the Sn nePCM: (a) of the core and (b) of the encapsulating shell (spot size: 10 nm).

The relationship of shell thickness with the nePCM particle diameter size was studied. Both measurements were calculated from TEM images for more than 175 particles. Only the shell thickness in the nePCM particles under 200 nm was measured as bigger particles were too

dense and casted a shadow that did not allow them to be identified in the TEM images. Regardless of nePCM size however, the shell thickness values still fell around 9.78 nm (see Supplementary Figure 4.2). Therefore from the TEM images analysis, nePCM shell thickness was found to be 9.78 ± 2.5 nm, regardless of particle size.

In Figure 4.2 it can be observed how the encapsulating layer in Sn nanoparticles is composed of Sn oxide, as their compositional analysis, performed with an EDX spot size of 10 nm, showed a higher content in oxygen than that of the nucleus.

Sn nanoparticles were exposed to high temperature (280 °C) for 3 hours in a nitrogen atmosphere to evaluate their response. Figure 4.3 shows how the initially amorphous oxide shell became partially crystalline when exposed to high temperature. Figure 4.3 (a) depicts a TEM image where crystalline planes can be seen. Figure 4.3 (b) shows the SnO peaks that corresponded to the nanoparticle shell which appeared in the XRD analysis.
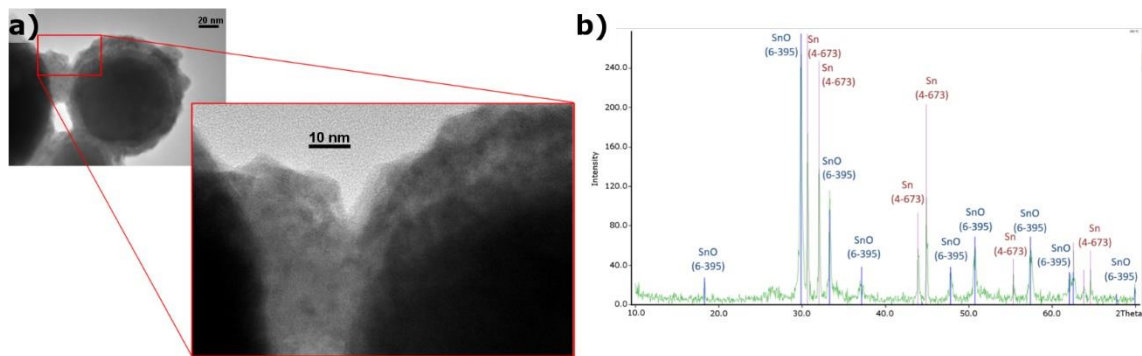
Figure 4.3. Encapsulating layer characterisation. (a) Detail of the TEM image of the oxide shell where a crystalline structure can be seen. (b) XRD analysis of the sample after exposure to high temperature (280 °C, 3 h).

4.3.2   Nanoencapsulation stability after thermal cycling and maximum working temperature

The phase-change characteristics of both nePCM and a piece of approximately 40 mg of bulk Sn were studied by thermal cycling. The comparison in Figure 4.4 (a) shows that the difference between both nePCMs and the bulk Sn melting points is almost negligible, with 229.5 °C for the bulk, 225.5 °C for the Sn 60–80 nm, and 232.1 °C for the Sn <300 nm. These results agree with the expected behaviour as the different melting temperatures depend on the size of nePCM[55]. However, a remarkable difference in their crystallisation temperatures was noted as the phenomenon known as supercooling appeared. This meant that the materials in the nucleus crystallised at much lower temperatures than those they melted at due to a small particle size and the absence of nucleation points. It was observed that the difference between the melting and crystallisation temperatures was only 2.3 °C for the bulk Sn, but 118.9 °C and 90.3 °C for the 60–80 nm and <300 nm Sn nanoparticles, respectively. Hence supercooling temperature was lower for the smallest particles, but was noticeable for both studied types[59].

It was also observed that phase-change enthalpies were considerably greater for the larger nePCM, with values of 48 J/g for the Sn < 300 nm sample compared to that of 18 J/g for the Sn 60–80 nm sample. This was expected as they presented a higher encapsulation ratio, which meant that a bigger part of the total mass of the sample was pure Sn nuclei, which melted and crystallised. By taking into account the enthalpy values obtained for both samples and for the Sn in bulk form (a phase-change enthalpy of 60 J/g), 30% encapsulation ratios for the Sn 60–80 nm and 80% ones for the Sn < 300 nm were obtained.

This trend was also observed when the encapsulation ratios for each sample were mathematically estimated, with values of 48 ± 8% of total encapsulation ratio for the Sn of nominal size 60–80 nm, and 68 ± 6% for the Sn of nominal size <300 nm. In this case, the total encapsulation ratio refers to the relation between the volume of nuclei and the total volume of nanoparticles, including a correction factor for the values of particles smaller than 120 nm in diameter according to the decrease they present in their phase-change enthalpies[55].
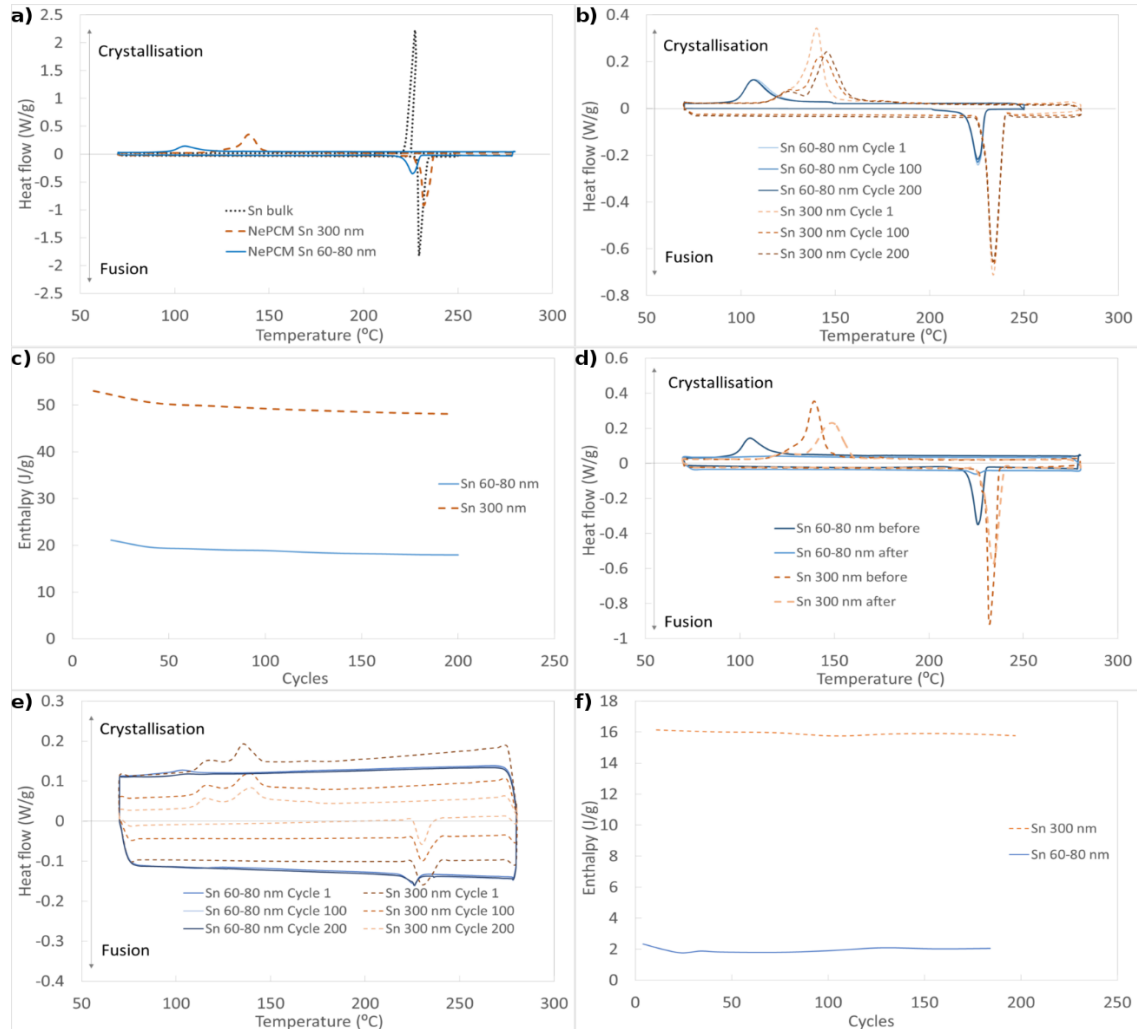
Figure 4.4. Differential scanning calorimetry (DSC) analysis of nanoencapsulation suitability and integrity. (a) Comparison of the properties of both nePCM samples with bulk Sn. Evolution of the (b) behaviour and (c) enthalpy of both samples (in powder) with thermal cycling. (d) Behaviour of samples before and after breakage. Evolution of the (e) behaviour and (f) enthalpy of both nanofluids composed of the Sn nePCM and TH66 with thermal cycling.

Figure 4.4 (b and c) illustrate the evolution of the nePCM in a powder form when thermal cycles are applied. The enthalpy values are slightly lower in the first 50 cycles, around 15% in Sn 60–80 nm and 9% in Sn < 300 nm, but become stable later. It is also noticed that while commercial 60–80 nm nePCM behaviour remains constant, the crystallising behaviour of the <300 nm particles varies from a single peak to two different ones. This is assumely due to changes in the samples nuclei diameter distribution.

Similar data are obtained from the analysis of the nePCM nanofluids, which consisted in a 30% mass loading of the nePCM in thermal oil Therminol 66, shown in Figure 4.4 (e and f). It can be observed that the stability in the enthalpy values is greater for the nanofluid than for the nePCM in a powder form, and remains practically constant for the <300 nm nanofluid sample.

Encapsulating shell resistance was tested and is shown in Figure 4.4 (d), where the phase-change enthalpies (corresponding to the peak area in each of the curves) clearly reduced after the breakage thermal cycle up to 400 °C. This drop in enthalpy values was 87% in the Sn 60–80 nm sample and 13% in the Sn < 300 nm one. This behaviour was expected as the covering shell breakage of some nePCM and their following exposure to air caused their nuclei to oxidise. Hence the pure material volume available to the phase change is reduced.
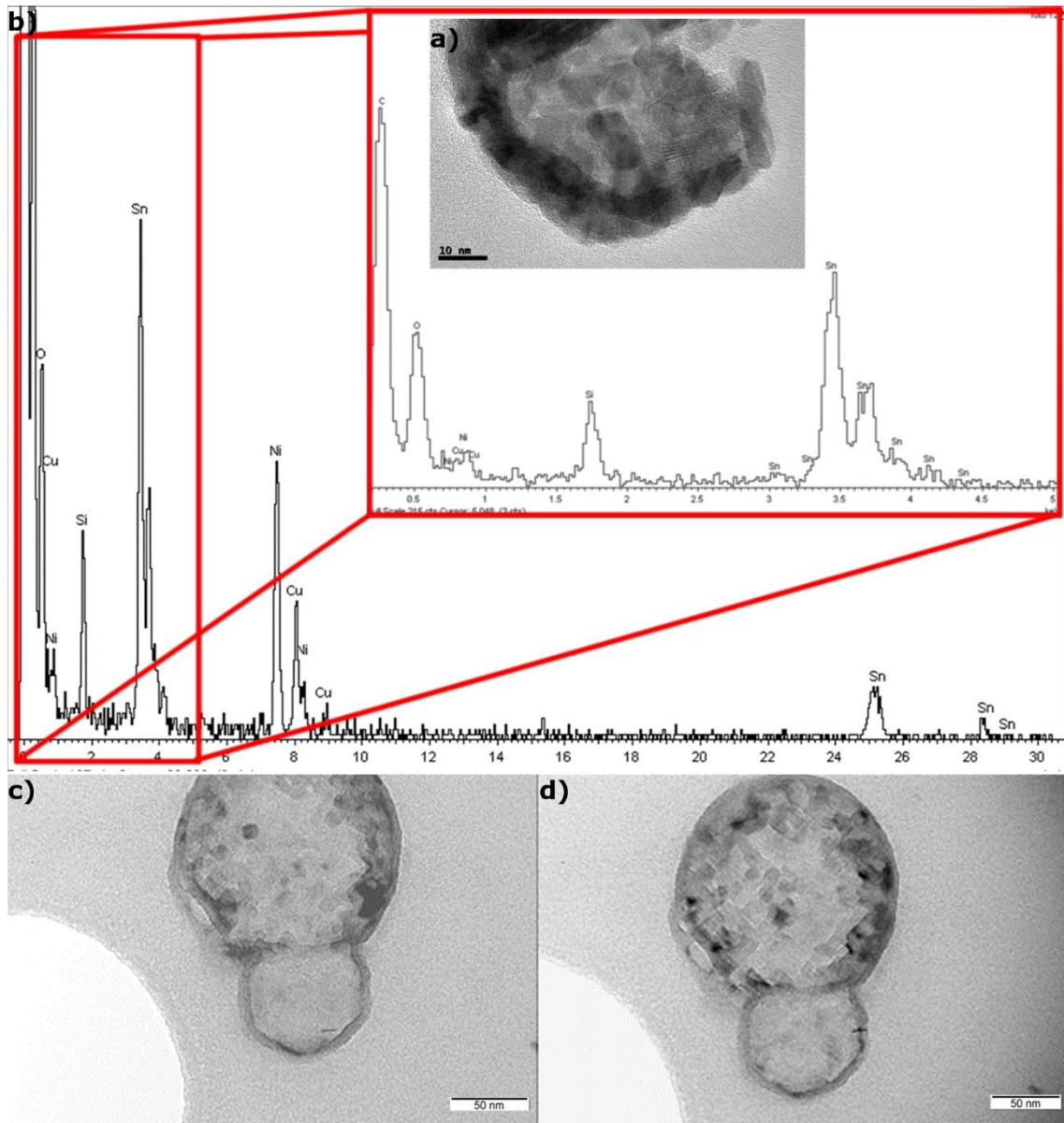
Figure 4.5. Integrity and breaking point of encapsulation. (a) TEM image and (b) EDX analysis of broken encapsulation after surpassing the breakage temperature, where the pure metal of the nucleus became SnO. High-temperature TEM images of Sn@SnO nePCM at (c) 70 °C and (d) 300 °C.

The breakage and oxidation of the nucleus when exposed to temperatures up to 400 °C is observed in Figure 4.5 (a), where the crystalline nature of the oxide can be seen in the former particle nucleus, and the higher content in oxide is shown in the EDX analysis in Figure 4.5 (b).

Nevertheless, encapsulation integrity was proved for 300 °C, as it can be seen in the HT-TEM images in Figure 4.5 (c and d), where the oxide that covers the shell remains unaltered at this temperature and no breakage is observed.

4.3.3   Performance comparison between base fluid and nePCM nanofluid

A comparison of behaviour between the base fluid and nanofluid with Sn < 300 nm was made in order to prove the thermal energy storage (TES) capacity and thermal conductivity increase of the latter. TES capacity is taken as the sum of the sensible heat and latent heat. In Figure 4.6 (a) it can be observed that there is an improvement in the performance of the nanofluid. This improvement depends on the cycling temperature range, since the latent heat enhancement by the addition of nePCMs has a bigger effect for smaller temperature increments, and as ΔT increases, the specific heat (sensible heat) has a stronger contribution than the phase-change enthalpy of the particles in the TES capacity.

Figure 4.6 (b) shows the experimental values of thermal conductivity improvement obtained for 50 °C and 100 °C, and their agreement with the predicted values by using Maxwell equation[41].
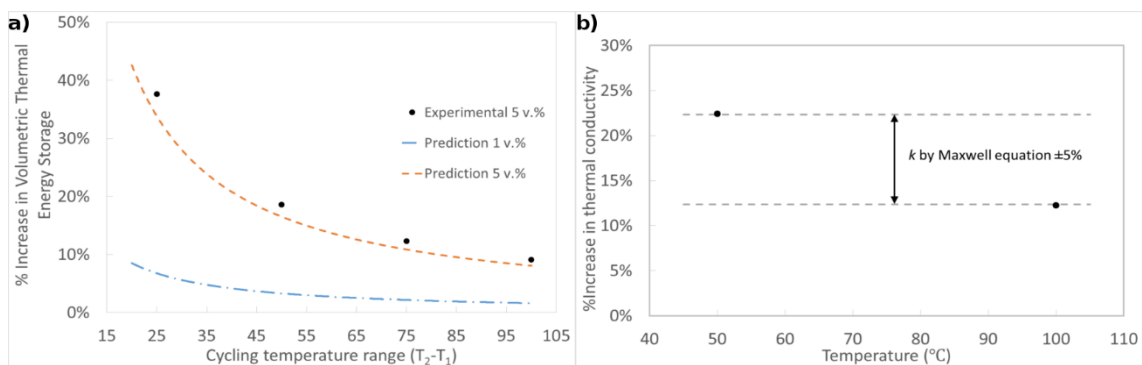
Figure 4.6. Comparison of nanofluid and base fluid performance. (a) Increase in volumetric thermal energy storage capacity for 1 v.% and 5 v.% loading of Sn < 300 nm nePCM in TH66 as a function of the cycling temperature range. Dotted lines correspond to predictions. Black points correspond to experimental measurements for the 5 v.% nePCM loading. (b) Experimental values of thermal conductivity for the base fluid and nanofluid with 5 v.% loading, and correlation with the values predicted by Maxwell equation.

4.3.4   NePCM supercooling control by using non-eutectic metal alloys

As previously explained, supercooling occurs in nePCM and results in crystallisation taking place at lower temperatures than melting. Although this feature can be interesting for thermal regulation applications, one way of avoiding supercooling by using non-eutectic metal alloys was investigated.

In-house metal alloy nanoparticles based on Sn and Pb were synthesised. Their composition is shown in the EELS analysis in Figure 4.7. Here, it can be observed that the nucleus contains the Sn/Pb alloy, whereas the oxide that forms the encapsulating shell is mainly Sn oxide.

According to the phase diagram in Figure 4.8 (a), for the non-eutectic alloys there is a range of temperatures within which a solid and a liquid phase co-exist. The remainders
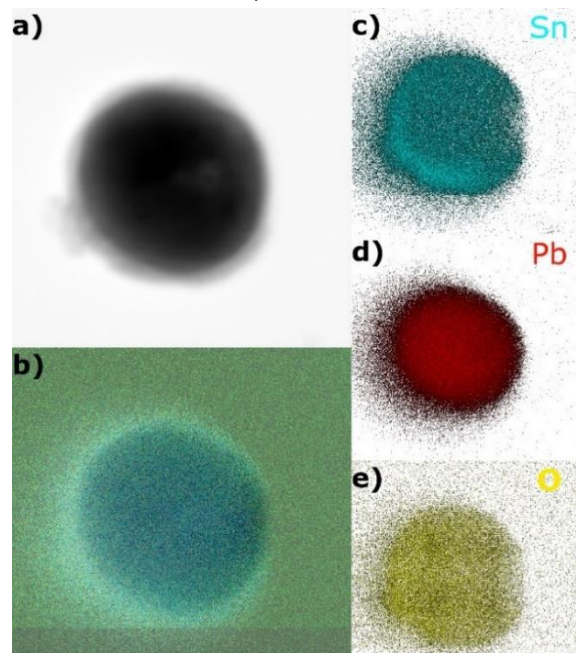
Figure 4.7. EELS image of a Sn/Pb alloy nanoparticle where the composition is observed: (a, b) general view of the nePCM. Composition of (c) Sn, (d) Pb and (e) O.

30

of this solid phase act as nucleation points for heterogeneous crystallisation, as opposed to the homogeneous nucleation that takes place in eutectic alloys or non-eutectic alloys when the whole nucleus is melted.

The alloy nePCM behaviour is seen in Figure 4.8 (b), along with thermal cycles with different maximum temperatures (between 190 °C and 250 °C). It can be noted that when nePCM nuclei do not completely melt crystallisation takes place at two different temperatures, first at a similar temperature to that of melting, and then at that which corresponds to the supercooling phenomenon.
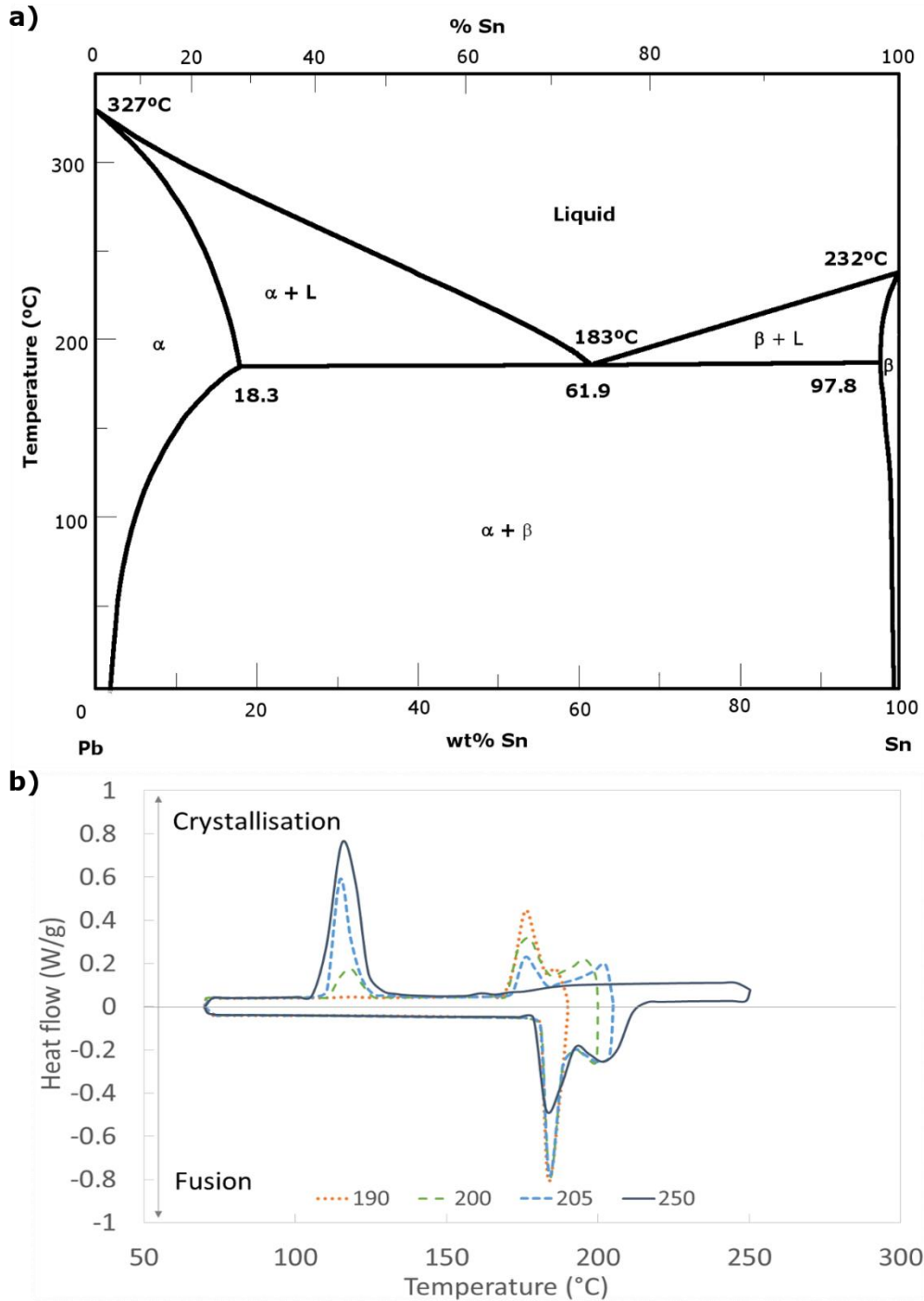
Figure 4.8. (a) Phase diagram of the Sn/Pb alloy and (b) DSC analysis of the Sn/Pb alloy thermal behaviour depending on the maximum temperature reached (between 190 °C and 250 °C).

It is also observed that the total crystallisation ratio which takes place at one temperature or another varies depending on how many of the nuclei melt. Thus, for higher temperature cycles, in which nuclei fusion is almost complete, most of the crystallisation takes place at the supercooling temperature, and only a small part occurs at a closer temperature to the melting one. As this trend is gradually inverted as fusion reduces, the cycles that reach lower temperatures show almost complete nuclei crystallisation at a similar temperature to the melting one, which avoids supercooling.

This behaviour is observed and quantified in Table 4.1, where the data of fusion and crystallisation enthalpies are shown. This table also shows the variation between both crystallisation peaks for different maximum cycle temperatures within the 190–250 °C range.

Here it is also shown the percentage of the total crystallisation enthalpy that takes place during the first crystallisation (ΔH_{cryst1}), with a temperature difference of around 9 °C with respect to the melting, and the second (ΔH_{cryst2}) that presents a temperature difference of 69 °C (between the melting and supercooled crystallisation). T_m, T_{cryst1} and T_{cryst2} refer to the melting temperature, and to the first and second crystallisation peaks, respectively.

Table 4.1. Summary of the melting and crystallising enthalpies of the Sn/Pb alloy depending on the maximum temperature reached (between 190 °C and 250 °C).

Max. cycle T (°C)	T_m (°C)	ΔH_{fusion} (J/g)	T_{cryst1} (°C)	ΔH_{cryst1} (J/g)	T_{cryst2} (°C)	ΔH_{cryst2} (J/g)	$\Delta H_{cryst1}/$ ΔH_{total} (%)	$\Delta H_{cryst2}/$ ΔH_{total} (%)
190.0	184.14	27.48	175.64	27.16	-	-	100.00	0.00
195.0	184.30	28.17	175.48	28.37	120.22	0.77	97.36	2.64
200.0	184.30	33.70	175.74	30.52	117.00	6.44	82.58	17.42
202.5	184.30	37.48	175.64	22.81	115.41	14.86	60.55	39.45
205.0	184.31	39.54	175.74	22.24	115.20	21.01	51.42	48.58
210.0	184.48	40.70	173.76	0.58	115.37	42.25	1.35	98.65
250.0	184.48	44.62	-	-	114.85	44.23	0.00	100.00

4.4 CONCLUSIONS

The suitability of a new nePCM type has been tested for its use in heat transfer nanofluids based on a synthetic thermal oil. The nanoparticles consist of a metallic nucleus covered by a metallic oxide shell that forms naturally during the fabrication process. This shell remains consistent throughout thermal cycling and prevents the material from the nucleus from leaking when in a melted state by resisting temperatures above the working temperature of the base fluid.

Addition of nePCM to a base fluid permits incremented heat capacity to be achieved due to the energy stored during the phase change, apart from the regular increment in thermal conductivity present in heat transfer nanofluids. The suitability of the metal oxide shell considerably lowers the costs to produce these nePCM compared with the techniques used to date.

A solution for the supercooling problem found in nePCM has also been studied. It consists in using non-eutectic metallic alloy nanoparticles in which the nucleus does not completely melt during the heating process. This leads to nucleation spots that allow crystallisation to happen at similar temperatures to melting ones.

4.5 SUPPLEMENTARY FIGURES
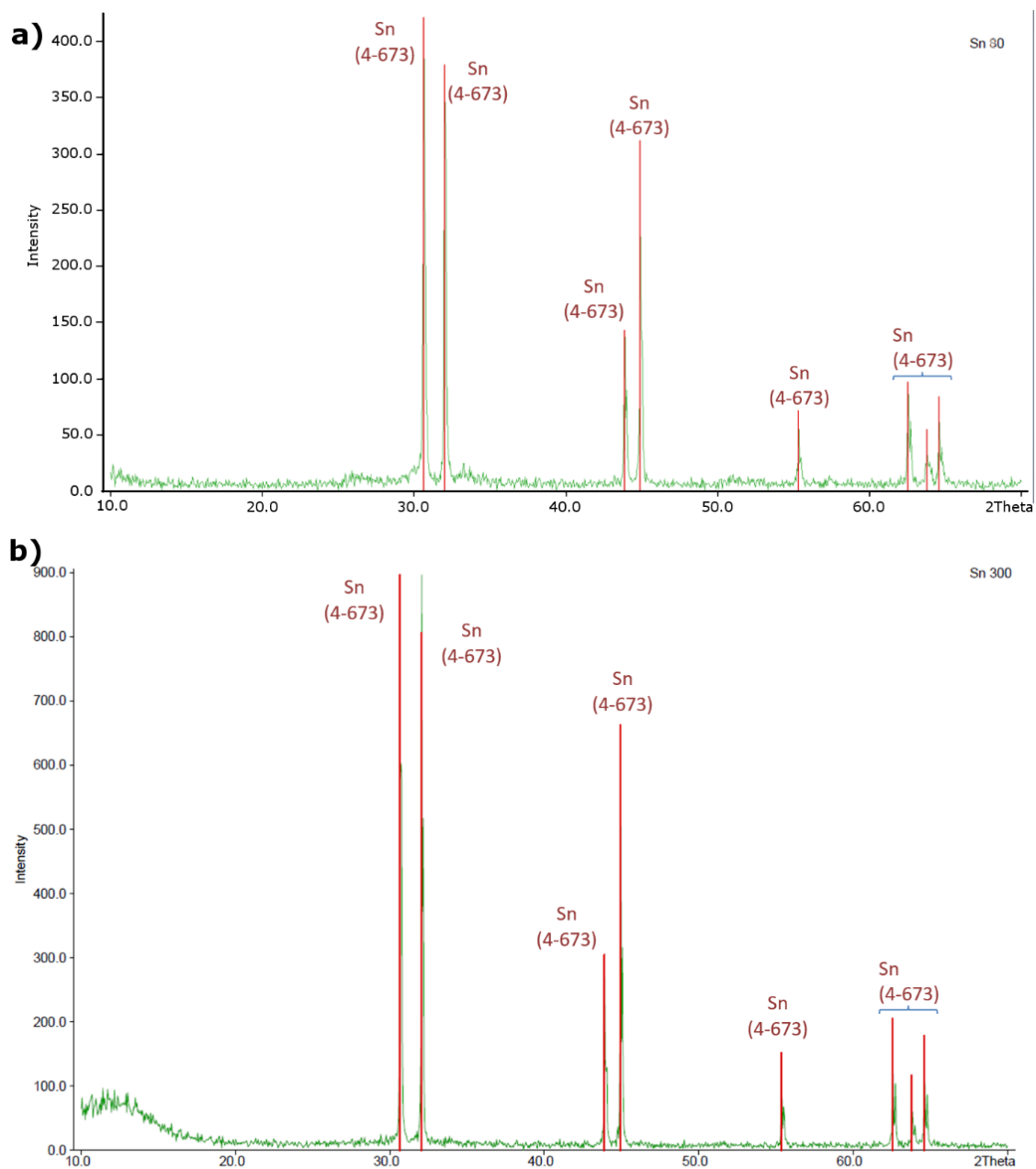
Supplementary Figure 4.1. XRD analysis of both nePCM samples studied before thermal treatment: (a) Sn of nominal size 60-80 nm, and (b) Sn of nominal size <300 nm.
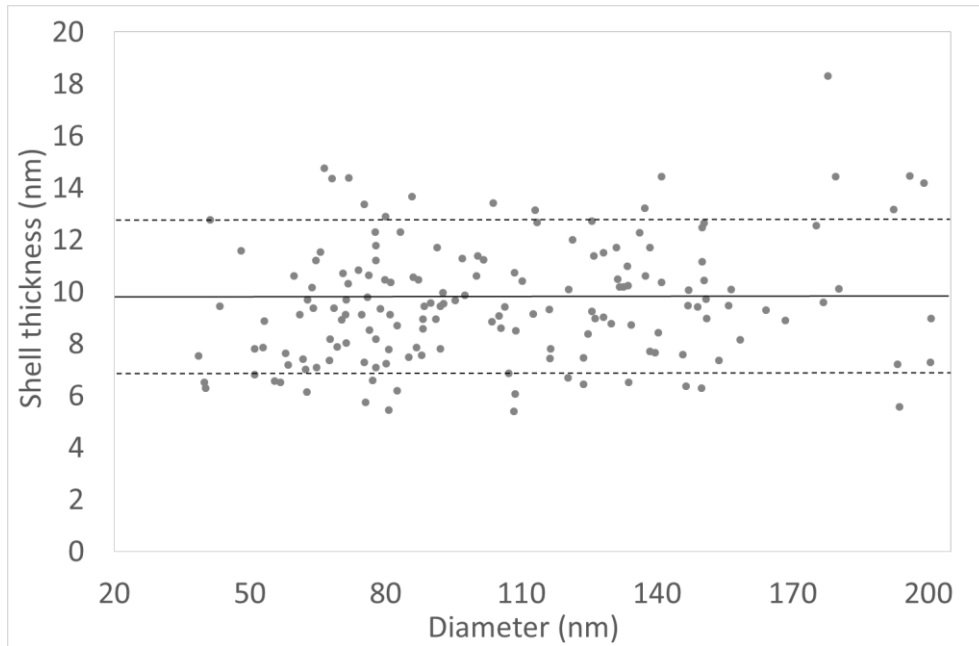
Supplementary Figure 4.2. Shell thickness vs. nePCM diameter distribution.

Chapter 5: THERMAL ENERGY STORAGE OF MOLTEN SALT-BASED NANOFLUID CONTAINING NANO-ENCAPSULATED METAL ALLOY PHASE CHANGE MATERIALS

The availability of thermal energy storage systems in concentrated solar power plants makes them suitable to handle the gap between energy supply and power demand. Increasing the total thermal energy storage capacity of the thermal energy storage materials used is of interest to improve their efficiency. In this work the thermal energy storage of the so called solar salt (60% NaNO$_3$ and 40% KNO$_3$) was improved by adding a phase change material composed of Al/Cu alloy nanoencapsulated with an aluminium oxide layer naturally formed when exposed to oxygen. The resistance of the oxide shell to thermal cycling up to 570 °C and its compatibility with the molten salt were proved. The specific heat and the total thermal energy storage were evaluated at different solid mass loads. Although the specific heat and thus the sensible heat storage decreases with solid content, the contribution of the phase change enthalpy and the latent heat storage can increase the total thermal energy storage up to a 17.8% at constant volume basis comparison. Besides, the thermal conductivity of the nanofluid was increased when adding the nanoparticles improving its heat transfer performance under some particular conditions

5.1 INTRODUCTION

Solar energy is one of the cleanest and cheapest energy resources that can be converted into thermal and electrical energy being eco-friendly. It has become the most important renewable energy source to reduce the consumption of fossil fuels and to mitigate Global Warming[60,61]. For high temperature applications, the solar radiation needs to be concentrated and the electricity generation can be achieved through concentrated solar power (CSP) plants. One of the features that make CSP plants different from other renewable technologies is the ability to include a thermal energy storage (TES) system in order to handle the intermittencies of solar availability and prevent the gap between energy supply and power demand[62].

Thermal energy storage can be achieved mainly by sensible heat storage and latent heat storage [63]. In sensible heat storage processes there is no phase change happening and materials experience a raise in temperature. The relation between the change in temperature and the stored heat is given by the specific heat of the TES material. In latent heat storage processes, the energy absorbed or released is stored by a phase transition at a constant temperature. TES materials used for latent heat storage are the so called phase change materials (PCMs) and the stored heat is given by the specific latent heat or phase change enthalpy [64–67].

Molten salts are widely used as heat transfer fluid (HTF) and TES materials in CSP plants[10,68]. Solar salt is the mixture of sodium and potassium nitrates (60:40 wt.% respectively) commonly used in this industry. Its higher decomposition temperature (550-600 °C) compared to that of water or thermal oils, makes it adequate for these high temperature applications, whereas its price is not excessive. However, its thermal properties such as thermal conductivity and specific heat are worse than those of water.

One of the actions gaining attention in the last years to increase the efficiency in the heat transfer and thermal storage systems currently present in these industrial processes is the use of salt-based nanofluids[22,26]. A nanofluid is a stable suspension of solid particles with nanometrical size used as HTF or TES material whose thermal properties have been enhanced[42]. The addition of nanoparticles to a base fluid implies an increment in the thermal conductivity of the nanofluid due to the higher thermal conductivity of the solid. Furthermore, although according to the mixture rule the specific heat of the nanofluid should decrease due to the lower specific heat of the nanoparticles, abnormal enhancements in the specific heat capacity of molten salts and ionic liquids have been reported[18–20,69–75,23,76,77]. This enhancement provides an increase in the sensible heat storage capacity of the TES material thus improving the efficiency of the storage system. The only salt-based nanofluid drawback is the increase in viscosity produced by the addition of the nanoparticles, which can lead to increments in pressure drop when used as HTF in dynamic conditions.

In order to further increase the total heat storage capacity of a TES material the use of nanoencapsulated phase change materials (nePCMs) was proposed[30,51–53,78]. To introduce these PCMs as the solid phase in a nanofluid, a core-shell structure is needed so the particles do not collapse into each other when in melted state, losing the advantages associated with their nanometric size. Therefore, nePCMs are composed of a PCM core and a covering shell with high melting temperature, resistant enough to prevent any leakage from the nucleus when it is in liquid state. The addition of a nePCM with high phase change enthalpy, capable of storing and releasing large quantities of energy during its melting and solidification processes

increments the total heat storage capacity of the nanofluids compared to the base fluid due to the contribution of the latent heat of the nanoparticles cores.

One of the main drawbacks of the use of nePCMs is the complexity in the synthesis process of the covering shell. The encapsulation of the PCM is achieved usually following a chemical route in which a polymeric or inorganic shell is produced[31,79]. However, authors have recently proposed the use of self-encapsulated metallic nePCMs[78]. Metals and alloys are used as latent heat storage materials due to their highest heat storage capacity per unit volume and thermal conductivity. The key feature of metals is that they undergo oxidation in contact with air easily. Although this could be considered as a drawback at a first sight, it was observed that the metal oxide nanolayer formed at the nanoparticle surface acts as a natural shell to encapsulate the metallic PCM, avoiding additional steps of encapsulation.

The present work proposes a nanofluid composed of a mixture of molten nitrates as the base fluid (solar salt) and nePCM consisting of Al/Cu alloy nuclei encapsulated by the metal oxide layer that is naturally formed when the nanoparticles are exposed to oxygen. The nePCM has been characterised and the suitability of the oxide shell as encapsulation has been proved for high temperature working conditions similar to those of possible industrial applications. The phase change enthalpy of the nePCM and the specific heat of the nanofluids were measured in order to evaluate the total heat storage capacity (contribution of both sensible and latent storage) for different concentrations of nanoparticles. A maximum enhancement of 10.6% at constant mass basis and 17.8% at constant volume basis was achieved for 10 wt.% of nePCM, demonstrating the improvement of the thermal performance of the fluid when adding the nePCM. Thermal conductivity was also measured and a maximum enhancement of 8.9% was achieved.

5.2 MATERIALS AND METHODS

5.2.1 Materials

The nanoparticles used and studied in this work were commercially obtained from Advanced Powder Technologies LLC. They consist on particles of an Aluminium-Copper alloy in an 80% Al-20% Cu weight percentage. They are produced by the wire explosion in inert gas method, what makes their size distribution wide, presenting particles that can reach from 20 up to 300 nm in diameter.

The base fluid used was a mixture of sodium and potassium nitrates, 60:40 wt.% respectively, commonly known as solar salt in the solar energy industry, where it is used as both TES material and HTF.

The nitrates were purchased from Labkem (Analytical grade ACS). They were weighted in the desired proportions and mechanically mixed in the laboratory with a mill. Any trace of humidity was previously removed by putting the nitrates in an oven at 100 °C for 20 min.

Nanofluids consisting of solar salt and Al/Cu nanoparticles with mass loadings of 0.5%, 1%, 1.5%, 5% and 10% were prepared. For that purpose, the nanoparticles were added to the previously mixed nitrates and mechanically blended. The commonly used dissolution method was avoided to prevent the full oxidation of the metallic nanoparticles cores.

5.2.2   Characterisation of Al/Cu nanoparticles

In order to fully characterise the Al/Cu nanoparticles, images were taken with a transmission electron microscope (TEM, JEOL-JEM 2100) and a scanning electron microscope (SEM, JEOL-JSM 6510). Analyses of these images were made to determine the morphology and size distribution of the nanoparticles, as well as the thickness of the encapsulating shell. The structure and chemical composition of the core and shell were studied using the same microscope, which includes High-Resolution and EDX (Oxford INCA) analysis modules.

Information of the phase change processes, such as the melting and crystallisation temperatures, phase change enthalpies, and their evolution through thermal cycling was obtained by differential scanning calorimetry analysis (DSC, DSC2 Mettler Toledo). A sample of around 13 mg of nanoparticles was analysed in a 40 μl aluminium crucible. 150 thermal cycles from 460 °C to 570 °C were performed under nitrogen atmosphere (25 ml/min N_2 flow rate), with 20 °C/min heating and cooling rates and 5 min isotherms at the maximum and minimum temperatures. More detailed analyses were performed every 20 cycles with the same characteristics but heating and cooling rates of 5 °C/min, in order to obtain more accurate values of the melting and crystallisation temperatures and enthalpies.

The specific heat of the nanoparticles was also measured by means of DSC tests. The method used was the areas method, which has been checked to provide better results than the dynamic or isostep methods[80]. In this method, a standard sapphire and the sample were submitted to consecutive isothermal segments with a 1 °C step and no heating stages amid. The DSC signal provided a peak, whose area was used to calculate the specific heat. Temperature steps were applied at 300 °C, 350 °C and 400 °C, with 5 min isotherms before and after the step. Tests were also carried out at a constant 25 ml/min N_2 flow rate. To ensure repeatability at least three samples were prepared. For each one, two cycles were run in order to obtain a mean value.

5.2.3   Characterisation of the nanofluids

A similar DSC analysis to that of the nanoparticles was performed over the nanofluid with Al/Cu at 10 wt.% using the same crucible. A sample of around 21 mg was submitted to 55 thermal cycles from 460 °C to 570 °C under nitrogen atmosphere, with 20 °C/min heating and cooling rates and 5 min isotherms at the maximum and minimum temperatures. 5 slow cycles in between to better observe the behaviour and evolution of the nanoparticles immerse in solar salt were performed at 5 °C/min heating and cooling rates.

The specific heat of the nanofluids was also measured following the same procedure stablished for the nanoparticles. The areas method was used with 1 °C step at 300 °C, 350 °C and 400 °C, with 5 min isotherms before and after the step. At least three samples of each nanofluid were prepared and two cycles were run for each one in order to obtain a mean value. The experimental error of the mean value was statistically obtained at a 95% of confidence level, with a mean error of 3.96% at 300 °C, 4.62% at 350 °C and 5.60% at 400 °C.

Thermal diffusivity was also measured by means of laser flash analysis (LFA, LFA427, Netzsch). In the LFA measurement, the diffusivity was determined by heating the front face of the sample by a laser with simultaneous record of the temperature profile on the rear face. Samples of around 91 mg where analysed in a platinum sample holder. The holder was previously coated with graphite to increase the absorption and emission of radiation. Thermal diffusivity was measured at 300 °C under nitrogen atmosphere.

Thermal conductivity of the nanofluids was calculated from these measurements using Equation 5.1:

$$k = \alpha * \rho * c_p \hspace{3cm} \textit{Equation 5.1}$$

where k is the thermal conductivity, α is the thermal diffusivity, c_p is the specific heat and ρ is the sample density which can be calculated from the mixture rule:

$$\rho = (1 - \phi)\rho_{bf} + \phi\rho_{np} \hspace{3cm} \textit{Equation 5.2}$$

where ϕ is the volume fraction, and ρ_{np} and ρ_{bf} are the densities of the nanoparticles and the base fluid respectively. The density of the molten solar salt was obtained from literature[10]:

$$\rho_{bf} = 2263.641 - 0.636 * T(K) \hspace{3cm} \textit{Equation 5.3}$$

5.3   RESULTS AND DISCUSSION

5.3.1   Nanoparticle characterisation

Al/Cu alloy nePCMs were first observed by means of TEM as shown in Figure 5.1 (a). The nanoparticles are mostly spherical with diameters around 85 nm. The presence of an external shell already existing as received was checked, avoiding the need of additional encapsulation steps. These shells have an almost constant thickness ranging from 6 to 8 nm as can be noticed in the micrograph. The encapsulation ratio was calculated as the nuclei volume/total particle volume ratio and a value of 0.532 was obtained.
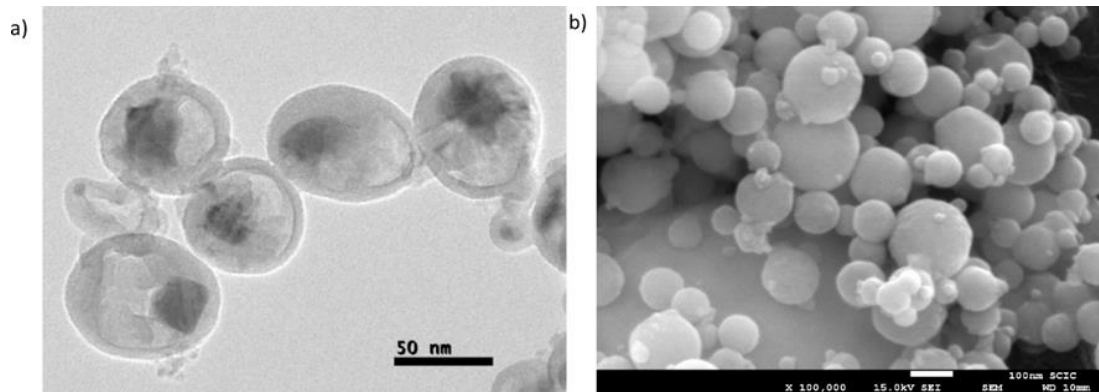
Figure 5.1. (a) TEM and (b) SEM micrographs of Al/Cu nePCM.

The nePCMs have also been observed by SEM (Figure 5.1 (b)) and more than 3200 diameters have been measured in order to obtain the particle size distribution depicted in Figure 5.2. It can be noticed that the diameters follow a lognormal trend, centred at 85 nm, with particles that can reach up to 300 nm.

EDX analysis confirmed that only aluminium, copper and oxygen were present in the sample as shown in Figure 5.3 (carbon and nickel are present from the sample holder). It was concluded that
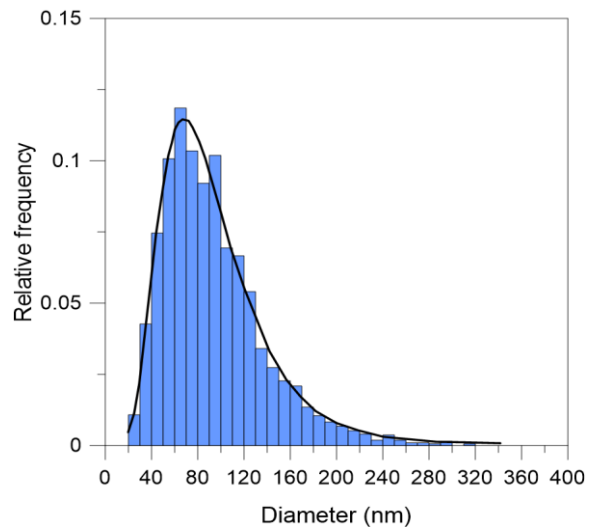
Figure 5.2. Nanoparticle size distribution measured by SEM.

nanoparticles are covered by an oxide shell naturally formed during the production process or when exposed to oxygen. As the aluminium is the main component of the alloy and it passivates faster than copper, the shell is composed of aluminium oxide. The natural formation of this covering oxide layer with high melting temperature creates an inert shell that prevents the nucleus material from leaking when melted. From the EDX analysis it was obtained that nanoparticles are composed of 47 wt.% of alumina shell and 53 wt.% of alloy core whose chemical composition is actually 56.6 wt.% Al and 43.4 wt.% Cu (0.754 Al - 0.246 Cu molar fraction).
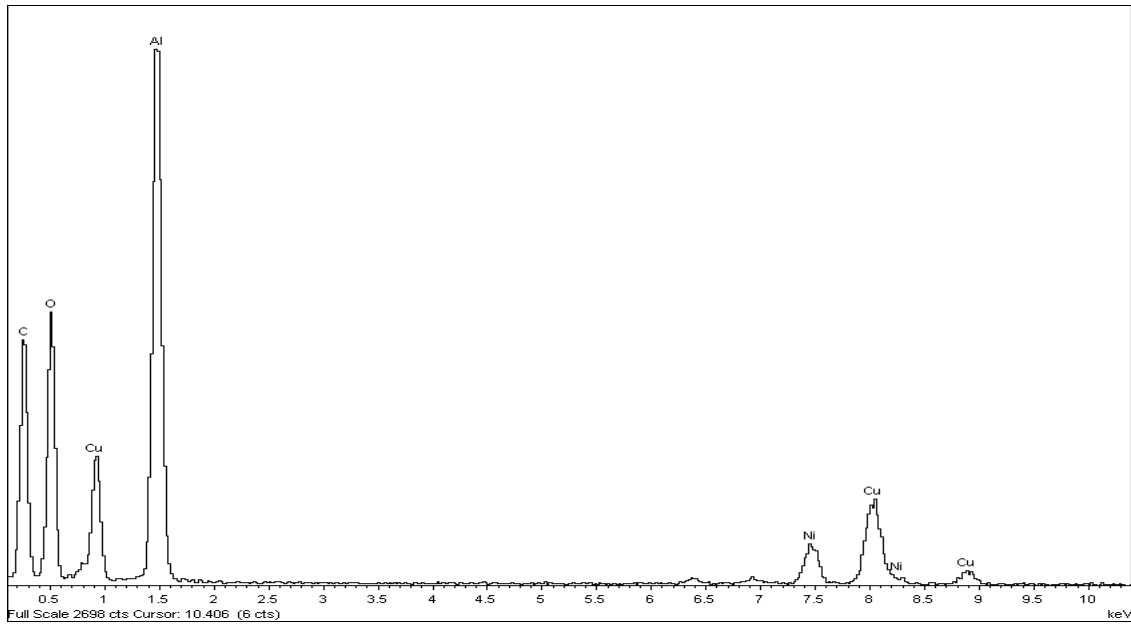
Figure 5.3. EDX analysis of Al/Cu nePCM.
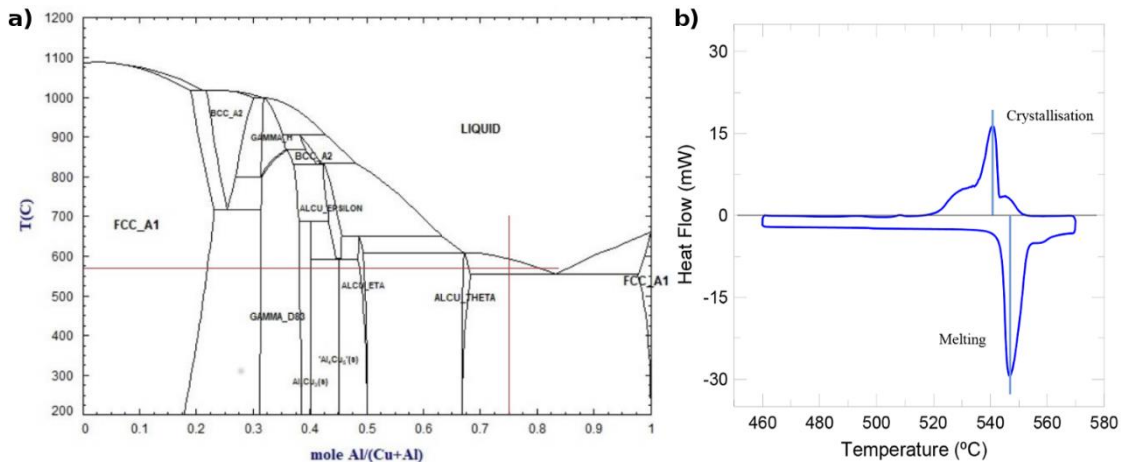
Figure 5.4. (a) Al/Cu phase diagram. (b) DSC analysis of Al/Cu nePCM with melting and crystallisation peaks marked.

5.3.2   Thermal cycling and latent heat of nePCM and nanofluids

Nanoparticles were submitted to DSC tests from 460 °C to 570 °C in order to obtain the phase change temperature and enthalpy. According to the phase diagram shown in Figure 5.4 (a), for the nanoparticle core composition obtained, the liquidus temperature is 547 °C while the solidus temperature is 585 °C. Therefore at 570 °C the core is not fully melted and a solid phase is still remaining together with the liquid phase. Results of DSC test in Figure 5.4 (b) provide a melting temperature of 546.74 °C in good agreement with the liquidus temperature

available while the crystallisation temperature provided is 540.95 °C. A slight difference between the melting and crystallisation temperatures (supercooling) can be noticed. This difference for Al/Cu alloy is smaller than for other metals because of the remaining solid phase that acts as a nucleation point for heterogeneous crystallisation to occur[78].
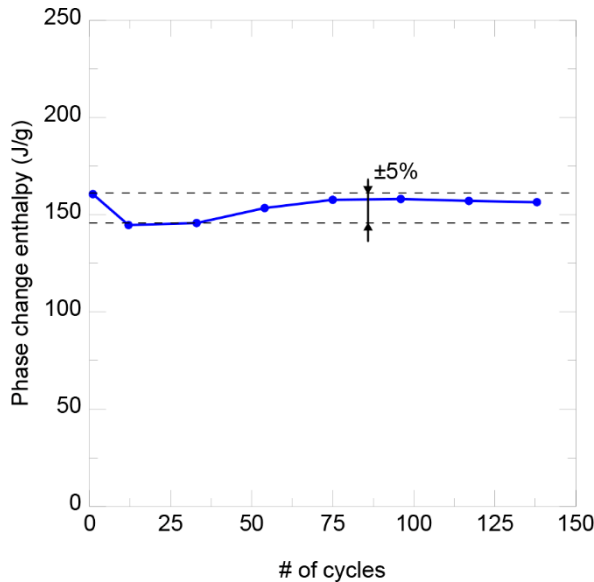
Figure 5.5. Evolution of the phase change enthalpy of the nePCM with thermal cycling.

The encapsulation resistance was tested through the evolution of the phase change enthalpy along 150 thermal cycles. The phase change enthalpy shown in Figure 5.5 corresponds to the melting peaks, as the width of the peak in the crystallisation is bigger and so it carries higher measurement errors. It is noticeable that there is a period of stabilisation of the nePCM in which the enthalpy apparently decreases during the first cycles, but this is just an artefact caused by a possible non-homogeneous powder-crucible contact. After that period the peaks adjust to their final shape, given that an increase in the values is registered after when the melting process is steady. The results corroborate that after this stabilisation period the melting enthalpy values are rather constant through the cycling and the encapsulating oxide shell stands for the thermal cycling with no change in the DSC curves. It was observed in previous works from the authors[78] that when the shell breaks the phase change enthalpy dramatically decreases, phenomenon not observed in this case.

In order to prove the thermal stability of the nePCM when dispersed in the molten salt, a nanofluid with 10% mass loading of nanoparticles was tested. Unlike specific heat, agglomeration of the nePCMs does not have an effect in latent heat, given that it is only dependent on the nuclei material available, i.e., on the mass of nePCMs present. The nanofluid with 10% mass loading was chosen for the tests since the values of phase change enthalpy are higher and thus, the measurement errors are minimised. 55 thermal cycles were performed in the sample and the effect of possible interactions between nanoparticles and base fluid on the performance of the nePCMs was checked through the evolution of the phase change enthalpy. The results of these tests are depicted in Figure 5.6. In Figure 5.6 (a) a negligible displacement of the melting peak is observed for the nePCM immersed in the molten salts. This, along with the stability of the phase change enthalpies observed in Figure 5.6 (b) proves that the interaction between the base fluid and the nanoparticles does not affect their thermal behaviour. Small variations of the phase change enthalpy are observed in Figure 5.6 (b). As previously observed for nePCMs, there is a stabilisation period in the first few cycles in which the latent heat decreases slightly. After this process, the values are constant within a 5% variability attributed to the measurement technique uncertainty. Therefore, the nePCM behaviour appears to be constant through thermal cycling and can be assumed to remain stable for the next cycles. These results show that the chosen combination of solar salt and Al/Cu nePCM is a compatible one for their use in thermal energy storage applications.
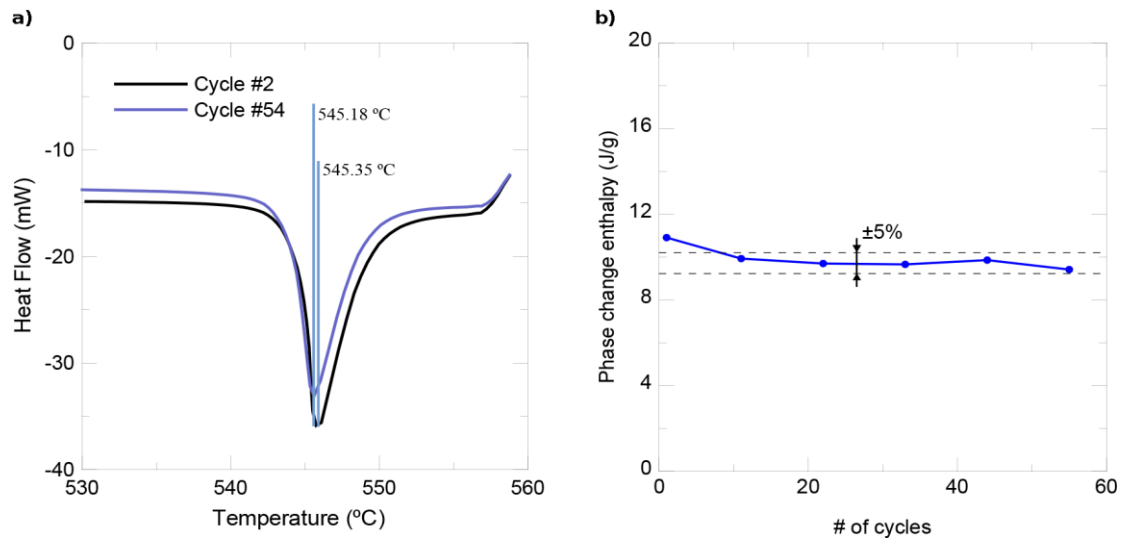
Figure 5.6. (a) DSC analysis of the nanofluid at 10% solid content at initial conditions and after 54 cycles. (b) Evolution of the phase change enthalpy of the nanofluid with thermal cycling.

5.3.3 Specific heat

Specific heat capacity of the pure molten salt, nePCM and the molten salt-based nanofluids was measured for different solid contents (0.5%, 1%, 1.5%, 5% and 10%) at three temperatures (300 °C, 350 °C and 400 °C). The absolute values obtained can be found in Table 5.1, and the specific heat enhancement is plotted in Figure 5.7. As a general rule the specific heat of the nanofluid is lower than that of the pure molten salt and decreases with solid content due to the lower value for the solid compared to the base fluid. However, an optimum value is achieved a 1.5%. This agrees with results previously found in literature, in which an abnormal enhancement is achieved at solid mass loads around 1%[69,81]. This phenomenon happens because of the nanoparticle-salt interactions that take place at the nanoparticle surface, mainly ionic exchange reactions, and depends on the available specific surface[23]. This specific surface increases with solid content up to reach a maximum value and then is reduced as the solid content is increased, due to agglomeration.
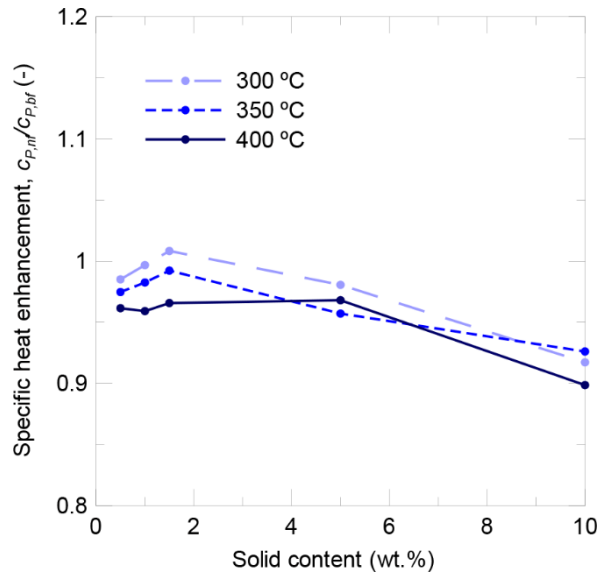
Figure 5.7. Evolution of specific heat enhancement with solid content and temperature.

The same trend is observed for all the temperatures tested and it can be concluded from the absolute values in Table 5.1 that the specific heat is almost constant with temperature and differences lay within the experimental error.

Specific heat of the nanofluids was theoretically calculated applying the mixture rule:

$$c_{p,nf} = w * c_{p,np} + (1 - w) * c_{p,bf}$$

Equation 5.4

where w is the solid mass fraction, $c_{p,nf}$, $c_{p,np}$ and $c_{p,bf}$ are the specific heat values of the nanofluid, nanoparticle and base fluid respectively.

The relative error, ε_r, between theoretical, $c_{p,th}$, and experimental, $c_{p,exp}$, results were calculated as follow:

$$\varepsilon_r = \frac{|c_{p,th} - c_{p,exp}|}{c_{p,th}} * 100 \qquad \text{Equation 5.5}$$

Specific heat of the nanoparticles was calculated according to the composition obtained for the core and shell structure by means of the specific heat values for Al, Cu and Al_2O_3 found in the handbook[82]. Theoretical and experimental results are in good agreement thus corroborating the chemical composition of the nanoparticles.

For the nanofluids, comparing the values obtained from the equation with the ones experimentally measured (Table 5.1), it can be deduced that the mixture rule fails to predict the abnormal enhancement as well as the values for higher concentrations and temperature, but shows a good agreement in the other conditions.

Table 5.1. Specific heat values for nePCM, base fluid and nanofluids at different solid content and temperature.

T (°C)	300			350			400		
Sample	$c_{P,exp}$ (J/g·K)	$c_{P,th}$ (J/g·K)	ε_r (%)	$c_{P,exp}$ (J/g·K)	$c_{P,th}$ (J/g·K)	ε_r (%)	$c_{P,exp}$ (J/g·K)	$c_{P,th}$ (J/g·K)	ε_r (%)
nePCM	0.895	0.898	0.39	0.919	0.920	0.07	0.930	0.941	1.20
Solar salt (SS)	1.503	1.495	0.56	1.503	1.503	0.02	1.549	1.512	2.46
SS+0.5%Al/Cu	1.481	1.500	1.29	1.465	1.500	2.34	1.489	1.546	3.66
SS+1%Al/Cu	1.498	1.497	0.08	1.477	1.497	1.37	1.486	1.543	3.71
SS+1.5%Al/Cu	1.516	1.494	1.45	1.491	1.494	0.19	1.496	1.540	2.85
SS+5%Al/Cu	1.474	1.473	0.09	1.438	1.474	2.40	1.499	1.518	1.23
SS+10%Al/Cu	1.379	1.442	4.41	1.392	1.445	3.66	1.392	1.487	6.41

5.3.4 Total energy density storage

The total energy density storage of the nanofluids can be expressed as the summation of the sensible heat storage of the mixture and the latent heat storage due to the melting of the nePCM, as shown in Equation 5.6 and Equation 5.7.

$$q_{total} = q_{sensible} + q_{latent} \qquad \text{Equation 5.6}$$

$$q_{total} = m * c_p * \Delta T + m * \Delta H_{fusion} \qquad \text{Equation 5.7}$$

The total energy density storage enhancement provided for the nanofluid compared to the base fluid was calculated by means of the following equation:

$$\Delta q_{total} = \frac{m_{nf}\left(c_{p,nf} * \Delta T + w * \Delta H_{fusion,np}\right)}{m_{bf}\left(c_{p,bf} * \Delta T\right)} =$$
$$= \frac{\rho_{nf} * V_{nf}\left(c_{p,nf} * \Delta T + w * \Delta H_{fusion,np}\right)}{\rho_{bf} * V_{bf}\left(c_{p,bf} * \Delta T\right)} \qquad \text{Equation 5.8}$$

The thermal energy storage enhancement was compared assuming constant mass ($m_{nf} = m_{bf}$) and constant volume ($V_{nf} = V_{bf}$) of the TES material at the same working temperature (close to the phase change). Results can be seen in Figure 5.8 (a and b), where the increase with mass loading of nePCMs is depicted for different temperature ranges in the region of the melting temperature of the nePCM. In both cases, at low concentrations the thermal energy storage decreases due to the decrease of the sensible heat and the small contribution of the latent

heat. However, as the solid content increases and thus the latent heat storage contribution becomes of importance the total thermal energy storage is increased. In the graph, it can be also observed that the largest improvements are achieved for the smallest temperature ranges because around the melting temperature the energy stored by the latent heat is higher than the sensible heat. For wider working temperature ranges and high nePCM concentration, sensible heat storage becomes the predominant process and the thermal energy storage enhancement decreases. A maximum enhancement of 10.6% at constant mass basis comparison and 17.8% at constant volume basis comparison can be achieved using the nanofluid containing nanoencapsulated phase change material.
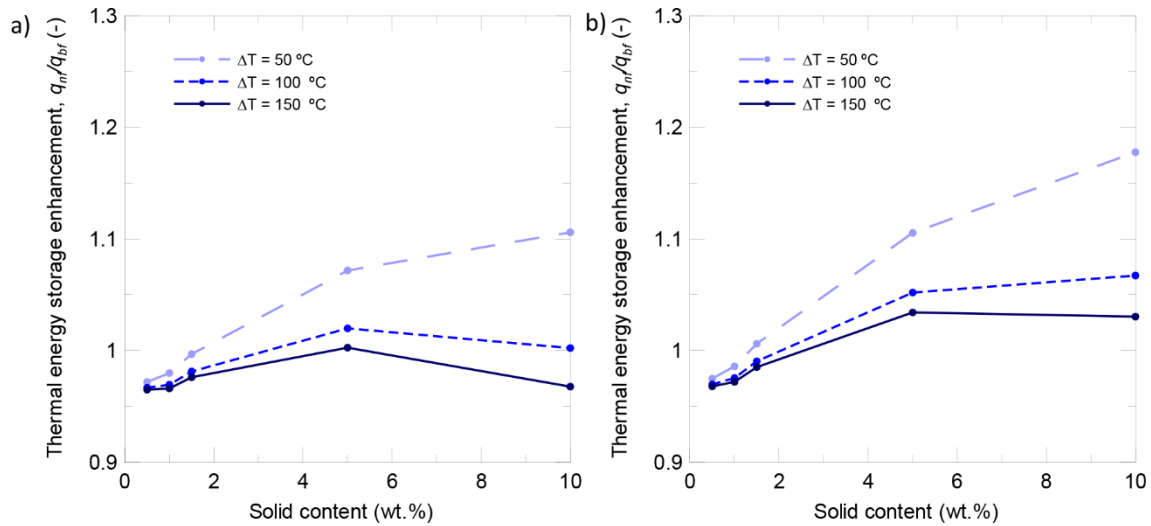
Figure 5.8. Evolution of thermal energy storage enhancement with solid content and temperature step at (a) constant mass basis and (b) constant volume basis comparison.

The enhancement achieved in the total thermal energy density storage of the solar salt has an economical and environmental impact. In general, the use of TES systems in CSP plants is attractive because allows to increase annual electricity generation compared to no backup with less greenhouse gas emissions[83]. If TES backup is compared to backup using a natural gas-fired heat transfer fluid heater, the former results in lower annual operation and maintenance costs per unit electricity sold. Also the levelized cost of energy (LCOE) of the plants is less sensitive to variability in nitrate salt pricing than variability in natural gas pricing. Therefore, the increase in the thermal storage and backup capacity can lead to an increase of the electricity generation avoiding the costs due to the need of using natural gas heaters. On the other hand, if the storage capacity of the TES material is higher, the same backup can be obtained reducing the mass or volume of salt thus reducing the cost of the material and the facilities containing it.

5.3.5   Thermal conductivity and heat transfer

Thermal diffusivity of the salt-based nanofluids was experimentally measured at 300 °C. Values obtained for the thermal conductivity are shown in Table 5.2. It can be observed that the addition of nanoparticles increases the thermal conductivity up to an 8.9% maximum. However, the thermal conductivity enhancement decreases with solid content in contrast to that predicted by the Maxwell model. At high concentrations, the abnormal results obtained indicate that the samples are not stable and the agglomeration of nanoparticles leads to a change in the nanofluid composition and properties on the measurement spot thus providing

thermal conductivities even lower than the pure salt. The same trend with solid content and temperature can be found in the literature[75].

Theoretical values were calculated by means of the equation for effective conductivity of Maxwell's model[11]:

$$k_{nf} = \frac{k_{np} + 2k_{bf} + 2(k_{np} - k_{bf})\phi}{k_{np} + 2k_{bf} - (k_{np} - k_{bf})\phi} k_{bf}$$

Equation 5.9

where ϕ is the volume fraction of nanoparticles and k_{nf}, k_{np} and k_{bf} are the thermal conductivities of the nanofluid, nanoparticle and base fluid respectively. Thermal conductivity of the nanoparticles was calculated according to the composition obtained for the core and shell structure by means of the thermal conductivity values for Al, Cu and Al_2O_3 found in the handbook[82] obtaining a result of 166.43 W/m·K.

The relative error, ε_r, between theoretical, k_{th}, and experimental, k_{exp}, results were calculated as follow:

$$\varepsilon_r = \frac{|k_{th} - k_{exp}|}{k_{th}} * 100$$

Equation 5.10

It can be also concluded from Table 5.2 that the Maxwell's model equation can predict the experimental results with less than a 6% of error for lower concentrations. Only for the highest concentrations the error obtained is high confirming the agglomeration of nanoparticles and bad experimental results mentioned above.

Table 5.2. Evolution of thermal diffusivity and thermal conductivity with solid content at 300 °C.

Sample	α (mm²/s)	ρ (kg/m³)	k_{exp} (W/m·K)	k_{th} (W/m·K)	ε_r (%)	k_{nf}/k_{bf} (-)
Solar salt (SS)	0.155	1899.2	0.441	0.450	1.98	-
SS+0.5%Al/Cu	0.170	1904.4	0.480	0.453	5.92	1.09
SS+1%Al/Cu	0.163	1909.4	0.465	0.457	1.87	1.06
SS+1.5%Al/Cu	0.156	1914.7	0.453	0.460	1.67	1.03
SS+5%Al/Cu	0.148	1951.6	0.424	0.486	12.69	0.96
SS+10%Al/Cu	0.121	2007.3	0.335	0.526	36.39	0.76

Regarding the heat transfer performance of nanofluids, the heat transfer coefficient (*h*) can be calculated from the Nusselt number:

$$Nu = \frac{h * D}{k}$$

Equation 5.11

For laminar flow regimen the Nusselt number is considered to be constant (*Nu* = 3.66 for circular pipes) and thus the increase in the heat transfer coefficient is directly proportional to the thermal conductivity enhancement. However, for turbulent flow regime the Nusselt number depends on the Reynolds and Prandtl numbers which depend in turn on the thermal conductivity, specific heat and viscosity. Although a more in depth analysis is needed to evaluate the heat transfer performance, the use of nanofluids with enhanced thermal conductivity has proved to increase the heat transfer coefficient when working at constant Reynolds number[46]. Therefore, thermal conductivity increases of molten salt-based nanofluids can be beneficial to improve its heat transfer performance under certain working conditions.

An approach to this analysis is shown in Table 5.3, where the heat transfer coefficient ratio has been used as the figure of merit to evaluate the heat transfer performance. Thus, for a

turbulent flow with the heat transfer coefficient described by the Dittus-Boelter equation, the ratio has been evaluated as:

$$\frac{h_{nf}}{h_{bf}} = \frac{Mo_{nf}}{Mo_{bf}} = \left(\frac{\rho_{nf}}{\rho_{bf}}\right)^{0.8} \left(\frac{c_{p,nf}}{c_{p,bf}}\right)^{0.4} \left(\frac{\eta_{nf}}{\eta_{bf}}\right)^{-0.4} \left(\frac{k_{nf}}{k_{bf}}\right)^{0.6} \qquad \textit{Equation 5.12}$$

where *Mo* is the Mouromtseff number[84], used in literature as an indicator of the heat transfer coefficient enhancement of nanofluids based on their physical parameters[85,86].

In order to resolve Equation 5.12, the density has been calculated from the density of pure components, specific heat and conductivity have been measured experimentally (Table 5.1 and Table 5.2), and the viscosity has been theoretically evaluated using the Einstein equation[87]. In Table 5.3 it is observed that the heat transfer performance is improved for the nanofluids with the smaller nePCM loads (0.5 wt.%, 1 wt.% and 1.5 wt.%) but it actually decreases for the higher ones. However, further research is needed as the Einstein equation is valid for dilute suspensions but usually fails to predict the viscosity of high concentrated samples.

Table 5.3. Evolution of heat transfer performance with solid content at 300 °C.

Sample	ρ (kg/m^3)	c_p (J/gK)	k (W/mK)	η (mPa·s)	Mo_{nf}/Mo_{bf}
Solar salt (SS)	1899.2	1.503	0.441	3.650	-
SS+0.5%Al/Cu	1904.4	1.481	0.480	3.673	1.046
SS+1%Al/Cu	1909.4	1.498	0.465	3.697	1.031
SS+1.5%Al/Cu	1914.7	1.516	0.453	3.720	1.018
SS+5%Al/Cu	1951.6	1.474	0.424	3.887	0.966
SS+10%Al/Cu	2007.2	1.379	0.335	4.139	0.814

5.4 CONCLUSIONS

A nePCM consisting on an Al/Cu metallic alloy nanoparticles with core-shell structure, in which the shell is a naturally formed layer of aluminium oxide, has been tested for its use in thermal energy storage applications. The nanoparticles have been proved to remain unaltered through thermal cycling, keeping their latent heat characteristics and resisting working temperatures common for the solar energy industry.

Nanofluids based on solar salt and Al/Cu nePCM with different concentrations have been characterised and compared to the base fluid alone in terms of specific heat, total thermal energy storage and thermal conductivity. Variations in the specific heat of the nanofluids have been observed, presenting in general a decrease of the values respect to solar salt, as expected from the mixture rule. However, although the sensible heat storage decreases the total energy storage can be increased thanks to the contribution of the latent heat storage of the nePCM. As the solid content is increased, the latent heat storage can overcome the sensible heat decrement and maximum energy storage of 10.6% at constant mass basis and 17.8% at constant volume basis can be achieved at 10 wt.% of nePCM for a working temperature range of 50 °C around the melting point. Besides, the addition of nanoparticles can increase the thermal conductivity of the nanofluid and improve its heat transfer performance under some particular conditions.

In conclusion, a nanofluid based on molten solar salt containing Al/Cu nePCM can be used as improved TES material showing chemical compatibility with the solar salt through thermal cycling. This technology has a positive economic and environmental impact.

Chapter 6: COLLOIDAL STABILITY OF MOLTEN SALT-BASED NANOFLUIDS: DYNAMIC LIGHT SCATTERING TESTS AT HIGH TEMPERATURE CONDITIONS

The use of molten salt-based nanofluids as heat transfer fluids or thermal energy storage materials to increase the efficiency of concentrated solar power plants has gained attention due to the use of the renewable energies against Global Warming. One of the issues of interest is the colloidal stability of the nanoparticles dispersed in ionic media like molten salts. In this work a new experimental set-up to measure the particle size distribution of molten salt-based nanofluids by means of dynamic light scattering was developed. The colloidal stability of silica and Al/Cu nanoparticles dispersed in solar salt (NaNO$_3$-KNO$_3$) was experimentally measured for the first time. Silica nanoparticles were dispersed in water, calcium nitrate tetrahydrate and solar salt, and the formation of micrometrical agglomerates was observed when molten salts were used as base fluid due to the high ionic strength of the medium and the reduced Debye length. The influence of the nanoparticle composition was proved to be also important. For the Al/Cu metal alloy nanoparticles the agglomerates formed were smaller than for silica. Besides, even though both nanoparticles settle after 4 h in static conditions, only Al/Cu nanoparticles recover the initial particle size distribution when they are mechanically redispersed.

6.1 INTRODUCTION

Solar energy has become the most important renewable energy source to reduce the consumption of fossil fuels and to mitigate Global Warming[60,61]. For high temperature applications, the solar radiation needs to be concentrated and the electricity generation can be achieved through concentrated solar power (CSP) plants. One of the features that make CSP plants different from other renewable technologies is the ability to include a thermal energy storage (TES) system in order to handle the intermittencies of solar availability and prevent the gap between energy supply and power demand[62].

Molten salts are widely used as heat transfer fluid (HTF) as well as TES materials in CSP plants[10,68]. Solar salt is the mixture of sodium and potassium nitrates (60:40 wt.% respectively) commonly used in this industry. However, its thermal properties such as thermal conductivity and specific heat are worse than those of water. One of the actions gaining attention in the last years to increase the efficiency of the systems currently present in these industrial processes is the use of salt-based nanofluids to increase the thermal conductivity and specific heat of the molten salts[19,22,23,26,69,75]. Recently, the addition of nanoencapsulated phase change materials (nePCM) has been proposed to increase the overall thermal energy storage capacity thanks to the contribution of the latent heat of the nePCM[30,53,78].

A nanofluid is a suspension of solid particles with nanometrical size whose key property is its stability. Stability in colloid science is used not only in the thermodynamic sense but also in a strictly colloidal sense. Colloidally stable means that the colloidal particles do not settle or do not agglomerate at a significant rate[88]. Because of the small particle size of nanoparticles the displacement due to the Brownian motion overcomes the Stokes sedimentation providing stable suspensions.

For conventional nanofluids using non-ionic liquids as base fluid such as water, glycols or thermal oils, the DLVO (Dejarguin-Landau-Verwey-Overbeek) theory can be used to predict the stability of the nanofluids by knowing the total energy of interaction between two particles[89–91]. In the range of sizes of nanofluids, the particle-surface-to-particle-volume ratio is so high that all the interactions are controlled by short-range forces like Van der Waals attraction and surface forces. When nanoparticles come into contact, they will remain together unless a longer-range repulsive force acts to prevent particles from approaching each other. In aqueous media electrostatic repulsion is preferred. Electrostatic interactions between particles are due to the presence of surface charges appearing when particles are suspended in water. In non-aqueous media or dispersions of non-polar solids in aqueous media, steric repulsion is needed. In this mechanism, repulsion is achieved by means of the adsorption to the particle surface of polymeric chains or non-ionic surfactants that extend into the surrounding medium. However, the preferred and most effective stabilisation mechanism involves electrosteric repulsion. In this case, both electrostatic and steric repulsion are combined, with the help of the addition of charged polymeric chains. Stabilisation of nanofluids is performed by means of the addition of ionic surfactants (cationic or anionic) that generate a charged medium surrounding the polymeric chains adsorbed to the particle surface.

Studies of ionic liquids such as high-temperature inorganic molten salts and low-temperature organic salts (also known as IL) have shown that traditional stabilisation mechanisms cannot explain the colloidal stability in this kind of highly concentrated electrolytes due to the strong electrostatic screening[92–94]. Therefore, for ionic liquids the stability depends on the chemical affinity between nanoparticle and base fluid. Indeed, it has been observed that stable salt-

based nanofluids can be produced for systems in which a new bonding is formed at the nanoparticle-fluid interface and the repulsive-oscillatory force of ion structuring exceeds both the van der Waals and the double-layer electrostatic contributions by far.

One of the challenges when working with molten salt-based nanofluids is the direct measurement of the colloidal stability in molten state at high temperature[62]. Experimental techniques available include measurement of the evolution of nanoparticle size distribution with time by means of dynamic light scattering (DLS) and the evolution of the light transmission through the sample at a fixed position. These techniques have been applied successfully for water and thermal oil-based nanofluids[86,95–97]. However, the measurements were performed at low temperature (< 60 °C) due to the requirements of the available equipment.

Up to date colloidal stability of molten salt-based nanofluids has been mainly determined by means of visual observation of the nanofluid kept in a furnace for very long periods of time. Alternatively, it can be evaluated through the measurement over time of different physical properties influenced by the nanoparticles dispersion. Jo and Banerjee[98] checked the stability of a nanofluid sample by measuring its specific heat capacity for five consecutive melting–crystallisation cycles, and no differences were found among them. Another method used to evaluate the settling of nanoparticles consists in keeping the molten salt-based nanofluid in a vial during a prolonged period of time at high temperature. After the solidification of the nanofluid, samples from the top and the bottom of the vial can be taken to measure and compare their specific heat capacity[69].

In this work, a new experimental set-up composed of an external, portable DLS system and a high temperature cuvette compatible with molten salts has been developed to measure the particle size distribution of the nanoparticles suspended at high temperature conditions up to 500 °C. In order to calibrate the device, silica nanoparticles were first dispersed in water and calcium nitrate tetrahydrate (melting point 42.7 °C) and the results were compared to measurements carried out in a commercially available equipment working up to 90 °C. Then, solar salt-based nanofluids were prepared and the colloidal stability of silica and Al/Cu nanoencapsulated phase change material was measured. The influence of the base fluid and the chemical composition of the nanoparticle were evaluated showing the instability of the nanoparticles in ionic fluids. Al/Cu nanoencapsulated phase change material showed the best behaviour as the initial particle size distribution is recovered when the nanofluid is mechanically redispersed after 4 h in static conditions.

6.2 MATERIALS AND SAMPLE PREPARATION

Different combinations of nanoparticles and base fluids were used for the production of nanofluids. Three nanofluids with silica nanoparticles were created using distilled water, $Ca(NO_3)_2$ and Solar salt as the base fluids. A different nanofluid containing solar salt and nanoparticles consisting of a metallic Al/Cu alloy was also prepared.

The nanoparticle concentration used for all the nanofluids was 0.46% in volume. Despite being a rather high loading for DLS measurements, this was tested to be a suitable concentration for measuring particle size and clustering behaviour being the solid load similar to real nanofluid applications.

The silica used for the nanofluids was obtained from a commercial suspension (Ludox SM-30, 30 wt.% suspension in water, Sigma Aldrich). These are particles well dispersed in water with a narrow size distribution. Three different nanofluids were prepared with silica nanoparticles. For the one using water as the base fluid, the corresponding volume of silica solution was added to 100 ml of distilled water to obtain the desired concentration of 0.46 v.%. The nanofluid was then dispersed using an ultrasonic probe (Sonopuls HD2200, Bandelin, HF-output of 200 W and HF-frequency of 20 kHz) during 3 min at 100%. It was previously tested that these conditions are optimal for homogenisation of samples of this volume with high energy input systems[91]. The improvements after this time are negligible and it avoids excessive heating of the fluid due to the sonication.

For the synthesis of the $Ca(NO_3)_2$-based nanofluid, the nitrate (Calcium nitrate tetrahydrate, ACS reagent, 99-103%, Sigma Aldrich) was previously left overnight in an oven at 80 °C in order to avoid any possible moisture, since its deliquescence is very high. The melting point of the nitrate is 42.7 °C and it can be handled in liquid phase at relatively low temperatures. The silica in solution was added to the molten nitrate and mixed with a magnetical stirrer and then put back in the oven to remove the water contained in the Ludox suspension. After that, it was let cool down to 60 °C in order to be able to use the ultrasonic probe while it remained in melted state. The nanofluid was sonicated during 3 min at 100%.

Solar salt is the name given to the mixture of $NaNO_3$ and KNO_3 commonly used in the solar thermal industry. $NaNO_3$ (Analytical grade ACS, Labkem) and KNO_3 (Extra pure, Scharlau) were mixed in a 60:40 wt.% proportion and the nanoparticles were added and hand-mixed. In the case of the silica nanofluid, the mixture was introduced in an oven at 100 °C to remove the water from the Ludox suspension. The nanoparticles were dispersed in both nanofluids (containing silica and Al/Cu nanoparticles) by melting the mixture at 300 °C and using a mechanical stirrer that consists of a rotating engine connected to a blade. The mixtures were stirred for 10 minutes at 1000 rpm and then immediately cooled in the form of pellets.

Al/Cu nanoparticles were commercially obtained from Advanced Powder Technologies LLC. They consist of particles of an Aluminium-Copper alloy in an 80%Al - 20%Cu weight percentage. They are produced by the wire explosion in inert gas method, what makes their size distribution wide, presenting particles that can reach from 20 up to 300 nm in diameter.

For the zeta potential measurements, nanoparticles were dispersed in an aqueous solution containing 1% of dissolved solar salt. Dispersion was made by applying 1 min of sonication with the ultrasound probe aforementioned. The pH value was modified adding NaOH and HCl solutions at 10 wt.%.

6.3 EXPERIMENTAL TECHNIQUES

6.3.1 TEM

The silica and Al/Cu primary nanoparticles were observed using transmission electron microscopy (TEM) imaging. Images were taken with an electronic microscope (TEM, JEOL-JEM 2100) operating at an accelerating voltage of 200 kV. The morphology and the primary particle size were studied. These images were then processed to measure the diameters of over 1000 particles and to obtain the particle size distribution.

6.3.2 DLS

The stability of the nanofluids has been analysed using two different dynamic light scattering systems. This technique measures the light scattered by the particles due to their Brownian motion, and associates its intensity with their size.

The silica nanofluids with water and $Ca(NO_3)_2$ as base fluids have been measured with a Malvern ZetaSizer Nano. This device is commonly used to measure particle size distributions in colloidal suspensions and nanofluids by means of dynamic light scattering (DLS). The equipment is composed of a laser, that illuminates the cell containing the sample, and a detector that acquires the intensity of the light scattered by the particles suspended. Both the laser and detector are enclosed in the device, and the hydrodynamic diameter is calculated based on the intensity of the scattered light at 173°. ZetaSizer has an incorporated heating system that allows the samples to be heated up to 90 °C. Samples of 1 ml are tested in a quartz cell and data is acquired in three sets of 90 seconds each. The distributions of those three datasets are then compared to check their similarity and averaged.

In order to measure the particle size distribution of molten salt-based nanofluids at high temperature conditions a new system was developed. A DLS device VASCO FLEX particle size analyser (Cordouan Technologies) consisting of an external laser head that contains the light emitter and receiver was used (65 mW-658 nm fiber pigtailed laser). The light registered corresponds to backscattering with an angle of 170°. In order to heat up and control the temperature of the samples, a high temperature cuvette was designed. It consists of a cylindrical stainless steel cuvette with two fused quartz windows on the sides with a 20 ml sample volume. A heating ring is installed around the cuvette and two K-thermocouples are used to control the temperature on the wall of the cuvette and inside the fluid. The maximum working temperature of this system is 500 °C. A camera and lighting system is also available to take images of the fluid evolution inside the cuvette. A more detailed scheme of this experimental set-up can be observed in Figure 6.1.

For the calibration of the new DLS system, water and calcium nitrate silica nanofluids were simultaneously measured with the ZetaSizer and the VASCO FLEX DLS systems respectively at 25 °C and 80 °C. Stability of the solar salt-based nanofluids was also studied with VASCO FLEX DLS system. Particle/cluster size was measured periodically during a 4-hour period for each of the samples, in order to observe the aggregation and sedimentation of the particles.

A refractive index of 1.46 and a viscosity of 23.093 cP were used for $Ca(NO_3)_2$ at 80 °C. For solar salt a refractive index of 1.41 and a viscosity of 8.5 cP were used based on previous measurements.
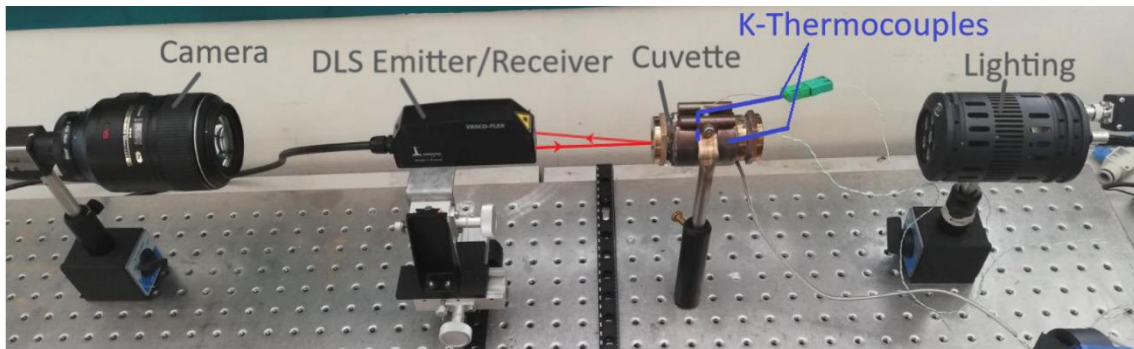
Figure 6.1. Experimental set-up for external high temperature DLS measurements.

6.3.3   Zeta potential

The zeta potential was measured at 25 °C using a Zetasizer Nano ZS (Malvern Instruments Ltd., UK) from the electrophoretic mobility of particles when an electric field is applied. This velocity is measured using laser Doppler velocimetry (LDV) and the zeta potential is obtained through the Henry equation.

6.4   RESULTS AND DISCUSSION

6.4.1   External dynamic light scattering system set-up and configuration

Initially, the VASCO FLEX external DLS system has been calibrated at low temperature in order to ensure the reliability of the results obtained at high temperature conditions. For that purpose, a comparison of the results obtained from the external system coupled to the heated cuvette and the closed DLS system, Malvern ZetaSizer, widely used in literature, has been carried out. Different nanofluids based on silica nanoparticles have been analysed. These particles were commercially obtained and present a narrow size distribution centred on 25 nm. Two different nanofluids were initially synthesised using water and $Ca(NO_3)_2$ as base fluids, with nanoparticle volume loadings of 0.46%.

The results obtained from these analyses are depicted in Figure 6.2 and presented in Table 6.1. All the samples were measured in both DLS systems. The nanofluid based on water was studied at room temperature and at 80 °C, whereas the one based on $Ca(NO_3)_2$ was only analysed at 80 °C, since the melting temperature of calcium nitrate tetrahydrate is 42.7 °C.
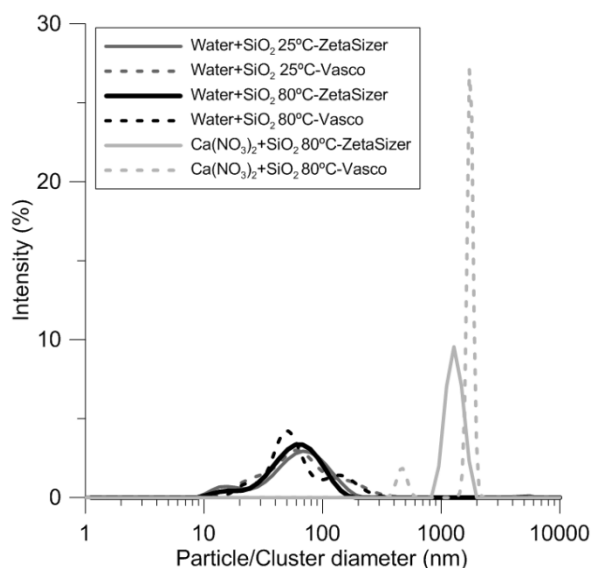
Figure 6.2. Particle size distributions of water and $Ca(NO_3)_2$-based silica nanofluids.

In Figure 6.2, it is observed that the particle distributions obtained in water nanofluids are almost identical for both DLS systems and that the differences for both temperatures are negligible. Both results obtained for the $Ca(NO_3)_2$ are also very similar. However, it should be taken into account that the longer stabilisation times in the ZetaSizer and the better resolution of the VASCO FLEX cause a smaller peak to be measured with the latter but not with the former.

In Table 6.1, $D_{i,50}$ of all the samples is compared. $D_{i,50}$ refers to the hydrodynamic diameter for which 50% of the scattered light comes from particles or particle clusters smaller than it. Small deviations exist among the measurements of all of the nanofluids studied. Thus, the reliability of the external DLS measuring system has been proven for both aqueous and ionic medium, as well as for different temperatures.

However, a great deviation is present between different base fluids, and particles are noticeably more aggregated within the nitrate salt. This phenomenon is due to the ionic charge of the medium and its influence on the colloidal stability of the nanoparticles suspended in it as it will be discussed later.

Sample	$D_{i,50}$ (nm) VASCO FLEX	$D_{i,50}$ (nm) ZetaSizer	Error (%)
Water+SiO$_2$ 25ºC	61.83	60.40	2.37
Water+SiO$_2$ 80ºC	56.36	60.80	7.30
Ca(NO$_3$)$_2$+SiO$_2$ 80ºC	1647.66	1590.00	3.63

6.4.2   Colloidal stability

There are several forces that determine the stability of nanofluids. Among them, Stokes sedimentation due to gravity and diffusivity due to Brownian motion can be used to calculate the colloidal stability limit of a suspension[24]. The colloidal stability limit is the critical size of a particle or particles cluster for which the displacement due to the Brownian motion equals the one due to the Stokes sedimentation. Thus, if they have bigger dimensions than the colloidal limit the Stokes sedimentation becomes predominant and the particles will settle being the nanofluid not stable through time. The diffusion of a particle due to Brownian motion can be calculated through Equation 6.1:

$$X = \left[t \frac{k_B T}{3\pi\eta a} \right]^{1/2} \qquad \text{Equation 6.1}$$

where t is time in seconds, k_B is Boltzmann's constant, T is temperature in Kelvin, η is the viscosity of the suspending fluid, and a is the particle radius.

On the other hand, the displacement due to the Stokes sedimentation can be calculated as shown in Equation 6.2:

$$X = \frac{2a^2 \left(\rho_{np} - \rho_{bf} \right) g t}{9\eta} \qquad \text{Equation 6.2}$$

where ρ_{np} is the density of the nanoparticle, ρ_{bf} is the density of the base fluid and g is the acceleration due to gravity.

The intersection between both parameters determine the colloidal limit for a particular combination of particle and base fluid, as it can be observed in Figure 6.3, where they have been calculated for different nanofluids including combinations of water, Ca(NO$_3$)$_2$ and solar salt as base fluids and silica and Al/Cu nanoparticles for the latter. The temperatures chosen vary according to the base fluid, being 25 °C and 80 °C for the water-based nanofluids, 80 °C for the Ca(NO$_3$)$_2$-based one, and 250 °C and 300 °C for the solar Salt. All the calculations have been made for a time of 300 s.

In Figure 6.3 (a), it is noticed that the colloidal limit in water is smaller for higher temperatures. Attending also to Figure 6.3 (b, c and d), it is concluded that the colloidal limit is higher for the silica nanoparticles immersed in ionic liquids (circa 400 nm for both Ca(NO$_3$)$_2$ and solar salt) than in water, and also that it is smaller for the Al/Cu nanoparticles than the silica ones in solar salt. Therefore, further stability will depend significantly on the cluster size achieved in the production process of the nanofluid.

Silica and Al/Cu metal alloy nanoparticles were used to analyse the influence of the base fluid and the nanoparticle composition on the colloidal stability. TEM micrographs of the nanoparticles are shown in Figure 6.4 in which the primary particle size can be observed.
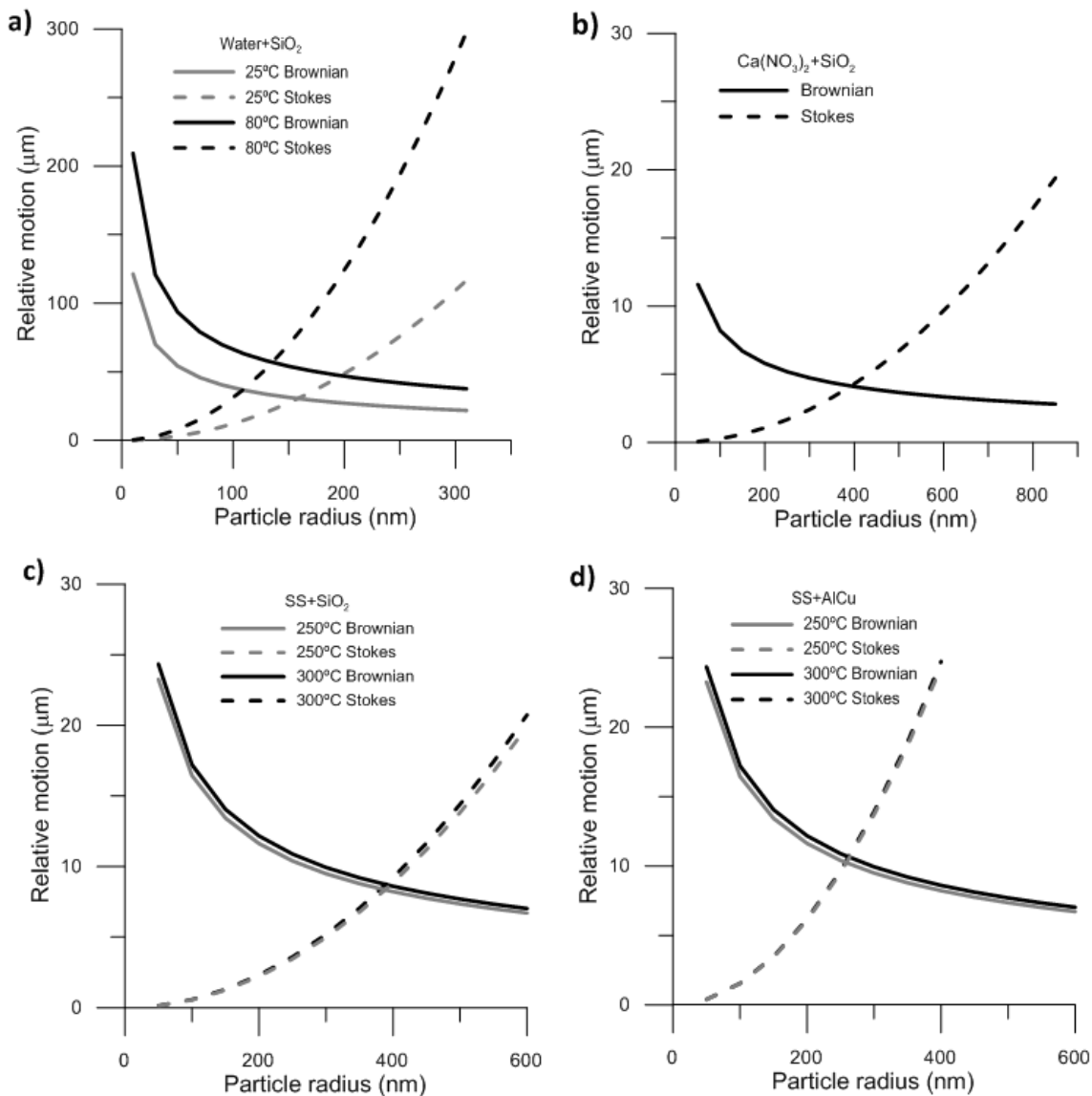
Figure 6.3. Colloidal stability limit of the nanofluids. Brownian motion and Stokes sedimentation influence on (a) water-SiO$_2$ nanofluids, (b) Ca(NO$_3$)$_2$-SiO$_2$ nanofluid, (c) solar salt-SiO$_2$ nanofluid and (d) solar salt-Al/Cu nanofluid.
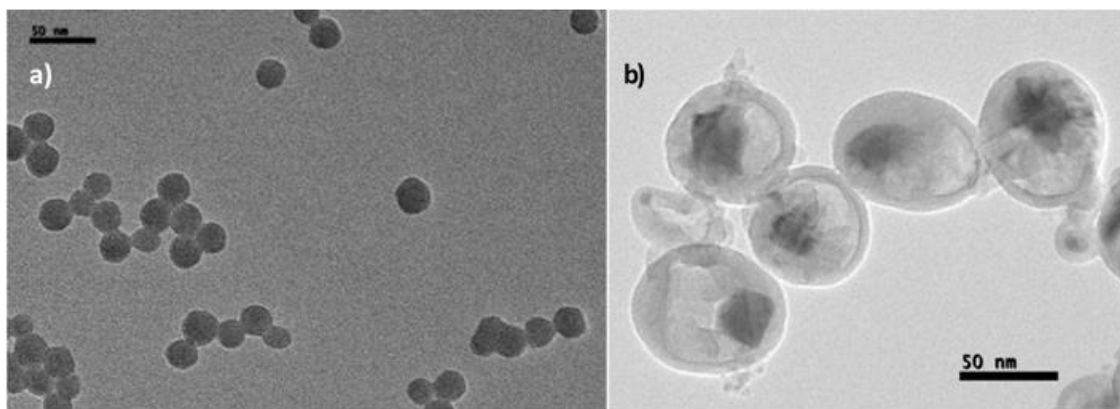
Figure 6.4. TEM micrographs of (a) SiO$_2$ and (b) Al/Cu nanoparticles.

Initially, experimental DLS measurements have been made for the silica nanoparticles immersed in three different base fluids in order to determine the influence of the latter in particle agglomeration.

The particle size distribution of the primary silica nanoparticles alone has also been studied by TEM imaging. In Figure 6.5, the results of this study are presented. It can be noticed that the initial size of the particles analysed by TEM imaging ranges from 12 to 36 nm, whereas the diameters detected in all the nanofluids are bigger. This feature shows that there is a certain amount of agglomeration for all the base fluids, but also that it is considerably higher for molten salts than for water. Regarding the nanofluid based on solar salt, it is also observed that some particle clusters are presumably out of the measuring range, as they are bigger than 10000 nm.
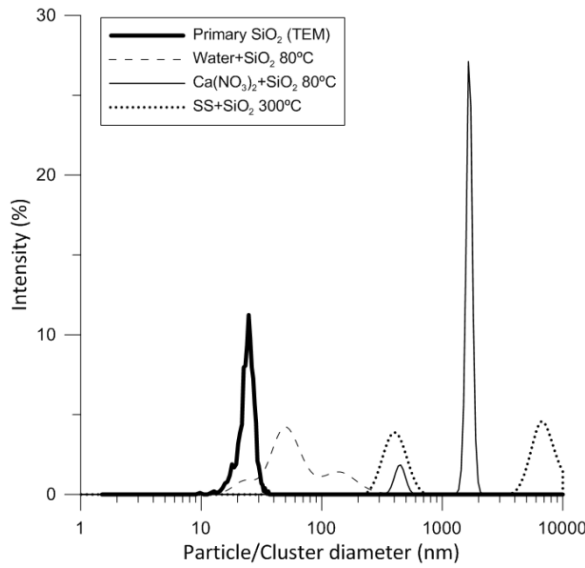
Figure 6.5. Particle size distributions of silica nanoparticles as purchased (measured by TEM micrograph analysis) and dispersed in different base fluids (DLS)

The agglomeration state achieved when the same nanoparticles are dispersed in different base fluids can be explained from the interaction forces acting on the solid-fluid system. For all the nanofluids tested that contain silica nanoparticles, the Van der Waals attraction forces depending on the Hamaker constant (A_{eff} = 6.3·10^{-21} J) will be similar, while the electrostatic repulsion forces, depending on the surface charge and the thickness of the electrical double layer (Debye length), will be the ones causing the final agglomeration state.

In Table 6.2, some parameters related to the electrical double layer thickness are compared to the sizes obtained in the DLS analysis. According to Debye-Hückel theory, an electrical double layer is formed whenever a solid-liquid interface exists as shown in Figure 6.6[99]. These are structures that appear in the solid surface, since the ions are ordered around it in the first layer due to surface charge phenomena and in the second layer because of the attraction of these first layer ions, electrically screening them. The existence of this double layer of ions surrounding every particle can be of use for stability purposes, as there are repulsion forces between the ions in the external layers of different particles. Overlap of the electrical double layers associated with two surfaces leads to an increase in the ionic concentration. The osmotic pressure that results from the increased concentration acts to push the surfaces apart.

In Table 6.2, the electrical double layer thickness has been then calculated according to the Equation 6.3[100]:

$$\kappa^{-1} = \left[\frac{\varepsilon\varepsilon_0 RT}{F^2 2I}\right]^{1/2}$$

where κ^{-1} is the double layer thickness, ε is the dielectrical constant of the medium, R is the ideal gas constant, T is the absolute temperature, F is Faraday's constant and I is the ionic strength of the medium.

The ionic strength of the medium, for molten salt-based nanofluids was calculated by means of the following equation:

$$I = \frac{1}{2} \sum c_i * z_i^2$$

<div align="right">*Equation 6.4*</div>

where c_i is the concentration of the ions present and z_i is their ionic charge.

For water-based nanofluids containing small amounts of electrolytes already present in the water, the empirical equation from Griffin and Jurinak[101], which permits to obtain the ionic strength from electrical conductivity measurements is:

$$I = 0.013 * EC$$

<div align="right">*Equation 6.5*</div>

Table 6.2. Electrical conductivity, ionic strength, Debye length and cluster size of the different nanofluids.

Sample	EC (mS/cm)	I (mol/L)	κ^{-1} (nm)	D_i (nm)/*Intensity* (%) Peak #1	Peak #2
Water+SiO$_2$ 25ºC	0.605	0.008	3.425	61.83/3.2	-
Water+SiO$_2$ 80ºC	1.140	0.015	2.397	51.39/4.2	142.11/1.4
Ca(NO$_3$)$_2$+SiO$_2$ 80ºC	6.540	31.128	0.017	451.46/1.9	1647.66/27.1
SS+SiO$_2$ 300ºC	-	20.910	0.023	392.99/3.9	6595.95/4.5

It is observed that as the ionic strength of the medium increases, the thickness of the electrical double layer decreases, and so the particles are more likely to agglomerate. This is in accordance with the size data obtained from DLS analyses, where a drastic increase in the clusters sizes can be noticed for the molten salt-based fluids, in which the ionic strength is greatly superior to that of water. It can also be observed that for divalent salts (Ca^{+2}) the ionic strength is higher and therefore the Debye length is lower leading to the formation of micrometrical agglomerates mainly. For the solar salt (monovalent salts) nanoparticles agglomerate having similar intensities and thus population of nanometrical and micrometrical clusters.
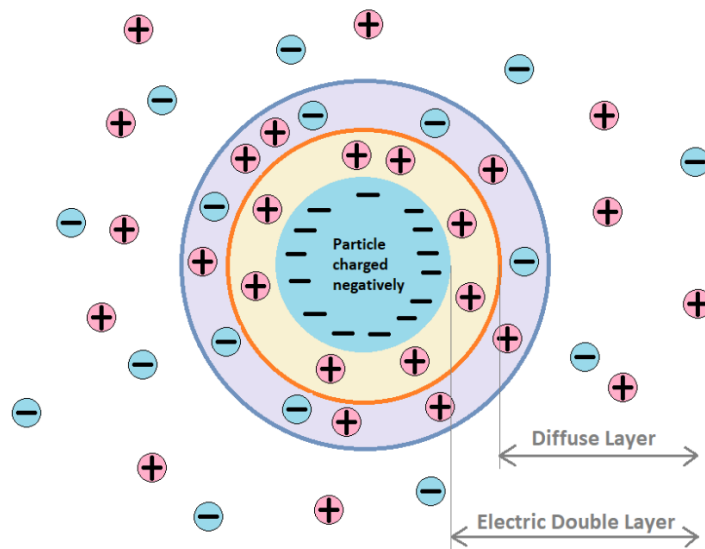
Figure 6.6. Electric double layer diagram. The negatively charged particle is surrounded by positive ions in the first layer so the particle appears to be neutrally charged from far away.

Furthermore, the evolution of agglomeration has been tested for the two nanofluids based on solar salt in order to compare the effect of the different nanoparticles on the stability. The fluids have been periodically analysed during 4 hours. The nanofluids have been mechanically redispersed after the test to check if it was possible to recover the initial particle size distribution. These analyses are depicted in Figure 6.7, Figure 6.8 and Figure 6.9.
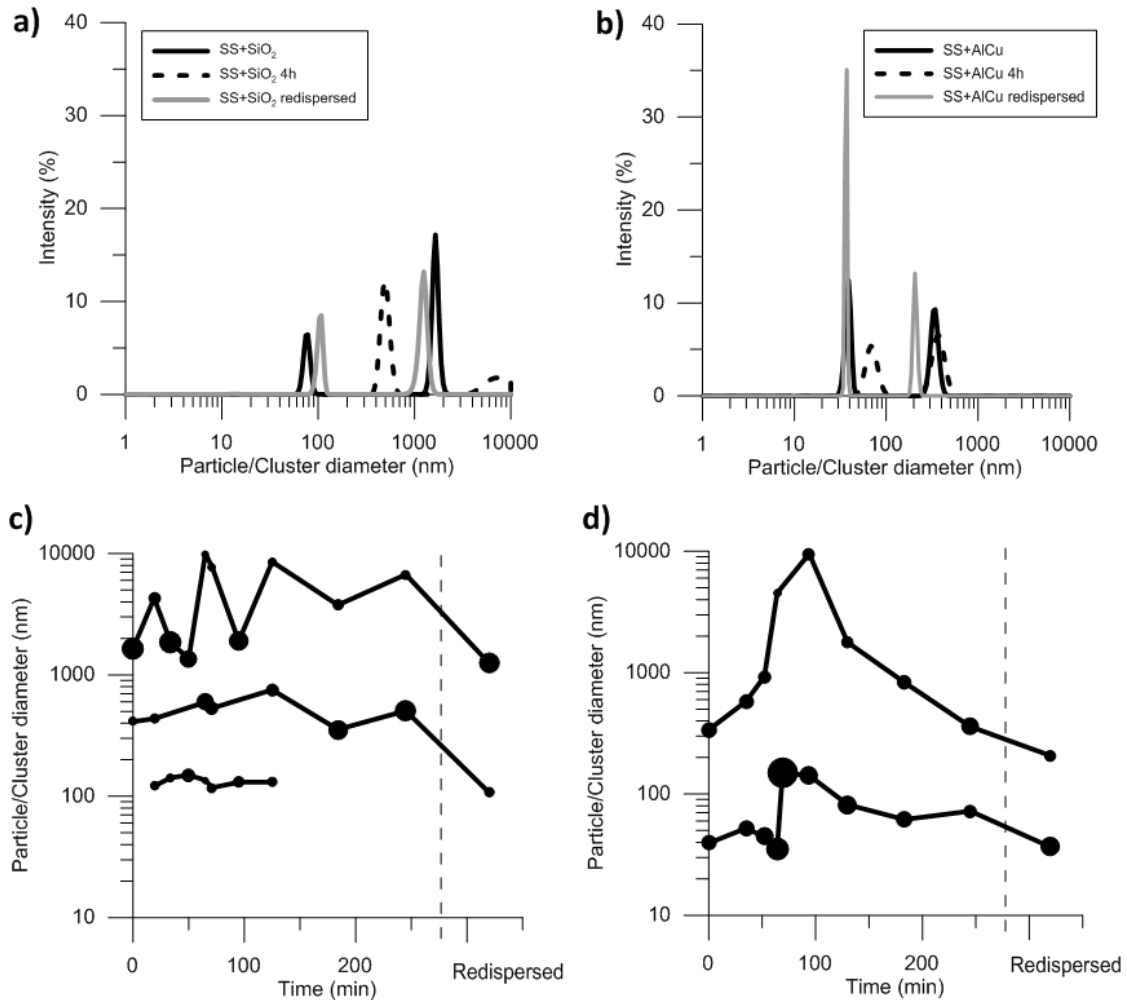
Figure 6.7. Evolution of particle size distributions through time and with redispersion for (a) and (c) SS-SiO₂ and (b) and (d) SS-Al/Cu at 250 °C.

In Figure 6.7 (a and b), the initial, final and after redispersion particle size distributions for both nanofluids at 250 °C are shown. It can be noticed that the cluster sizes are generally bigger in the silica nanofluid than for the Al/Cu. In both cases, clusters of nanoparticles whose size is bigger than the stability limit previously obtained are initially present indicating that nanoparticles will settle and the nanofluid will not be stable. In addition, it can be deduced from the figure that part of the clusters in the silica nanofluid after 4 h are above 10000 nm, so they do not appear in the analysis until they are redispersed, their size becomes smaller and they can be detected again by the DLS system.

Figure 6.7 (c and d) show the evolution of the main peaks of the size distribution through time and after redispersion. As the size distributions were not monomodal and a mean particle size cannot be used, it was plotted the size of the peaks obtained at any measured time. Bigger bubbles correspond to higher intensity peaks detected, namely, a higher number of clusters of that size. It is observed that for the silica nanofluid the clusters are generally bigger. It also

57

should be taken into account that when peaks appear around the limit of 10000 nm, part of the clusters are out of the measurement range, so the DLS equipment is only able to detect the smaller ones, leading to artefacts in which the apparent size of the sample is smaller. This artefacts can be observed around 100 min, where it seems like the highest peak of the size distribution has decreased, but it is only due to the biggest clusters falling out of the measurement range. On the other hand, the nanofluid with Al/Cu nanoparticles presents smaller sizes in general, although there is an increase starting at 45 minutes. Although both nanoparticles lead to unstable nanofluids, the one containing Al/Cu presents smaller cluster sizes and the agglomeration rate is lower. Besides, after the redispersion, both nanofluids effectively reduce the cluster sizes very close to the initial state, proving that mechanical stirring and the high shear conditions applied are suitable to break bigger agglomerates into smaller ones instead of promoting agglomeration.
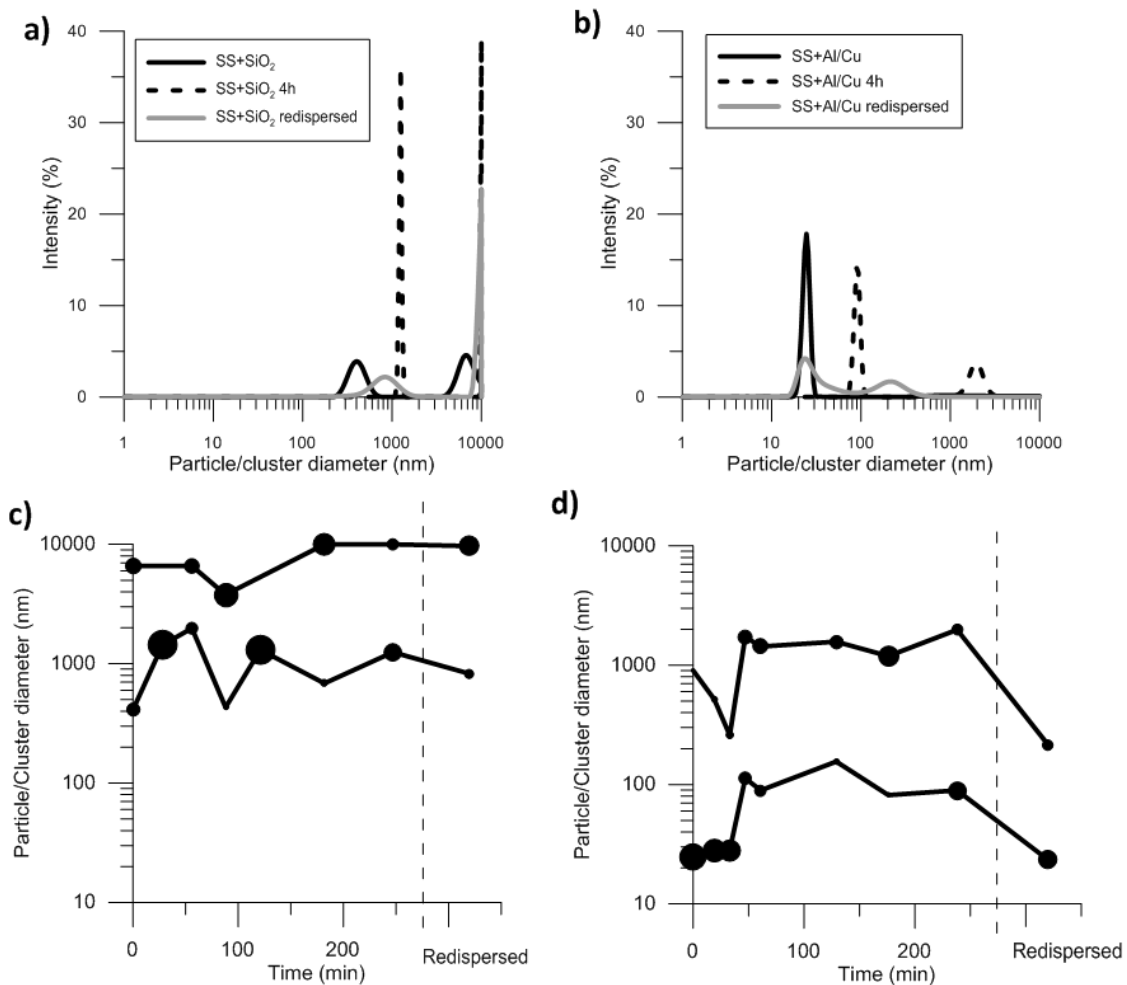
Figure 6.8. Evolution of particle size distributions through time and with redispersion for (a) and (c) SS-SiO₂ and (b) and (d) SS-Al/Cu at 300 °C.

In order to study the influence of the temperature on the stability, the same analysis has been done for the solar salt-based nanofluids at 300 °C. The results are depicted in Figure 6.8. In Figure 6.8 (a and b), similar results to the obtained at 250 °C are registered. The silica cluster sizes are initially bigger than the Al/Cu ones, and this difference is higher than for the lower temperature. Also, the amount of clusters with sizes above 10000 nm after 4 h is assumed to be bigger than for 250 °C, based on the higher intensity of the peak for this size. As expected, at higher temperature the fluid viscosity decreases while the Brownian motion is increases

promoting the contact and agglomeration of the nanoparticles. In Figure 6.8 (c and d), smaller clusters are registered for the nanofluid with Al/Cu nanoparticles, although there is an increase starting at 45 minutes, when most of the clusters appear to have sizes around 1500 nm. This increase was also registered for the nanofluid at 250 °C. The Al/Cu nanofluid presents also at 300 °C a lower agglomeration rate than the silica one. Finally, after the redispersion, the Al/Cu nanofluid effectively reduces the cluster sizes very close to the initial state, which does not occur in the silica nanofluid.

It is obvious that the chemical composition of the nanoparticle influences the solid-liquid interactions leading to different behaviours in stability. The two main parameters influencing the interaction forces that depend on the nanofluid composition are the Hamaker constant (related to attractive force) and the particle surface charge or zeta potential (related to electrostatic repulsive force)[102,103]. Regarding the Hamaker constant, its value for silica nanoparticles can be found in the literature but in the case of the Al/Cu nanoparticles it is difficult to determine. Although the core of the nanoparticles is composed by a known alloy, nanoparticles are encapsulated by an oxide shell as observed in Figure 6.4. This shell is assumed to be composed mainly of aluminium oxide and formed naturally by passivation of the metal but no exact composition and properties can be obtained to determine the nanoparticle behaviour. Therefore, real values for the Hamaker constant and the Van der Waals attractive force cannot be obtained but they are expected to be different due to the different chemical composition of the nanoparticles.
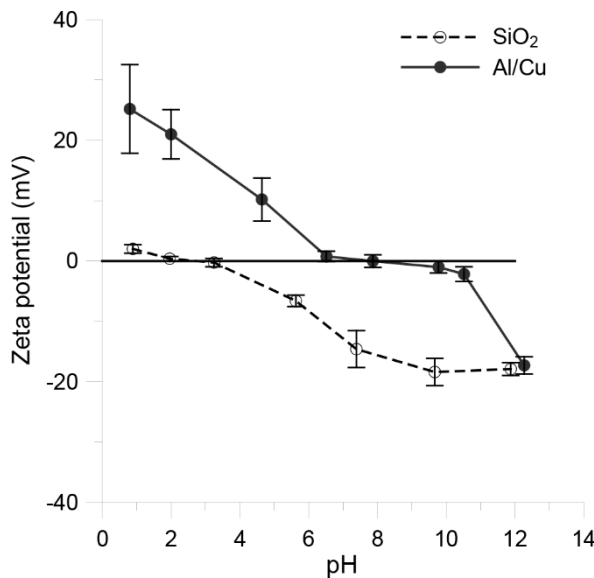
Figure 6.9. Evolution of zeta potential with pH for SiO$_2$ and Al/Cu dispersed in 1% solar salt aqueous solution.

Regarding the particle surface charge, the zeta potential and the point zero charge (or isoelectric point) of the nanoparticles also depends on the particle composition. From the best of the authors knowledge it is not possible to measure the zeta potential of nanoparticles dispersed in molten solar salt due to the high melting point. In spite of this the effect of the composition on the zeta potential behaviour was measured dispersing both nanoparticles in an aqueous solution containing a 1% of solar salt dissolved. It is known that the presence of electrolytes produces a screening effect reducing the surface charge so both nanoparticles were tested under the presence of small concentrations of salt. In Figure 6.9 the evolution of the zeta potential for both samples with pH is shown. For silica nanoparticles the isoelectric point was achieved at pH values close to 2, similar to that found in the literature. For the Al/Cu nanoparticles the isoelectric point was found at pH values close to 7 indicating that the surface composition is formed mainly of aluminium oxide whose values reported in the literature are close to 8. The differences found in the isoelectric point leads to a different behaviour and stability when dispersed in the same fluid media. It can be also observed that for the higher charged conditions (extreme pH values) the Al/Cu nanoparticles present a sharp slope with higher zeta potential than the silica ones and thus the stability is expected to be higher in agreement with

the DLS measurements. In addition, it has to be mentioned that the production process of both nanofluids is different. Thus, the initial agglomerate size distribution is also different.

This lack of stability can also be observed by the traditional method of direct visualisation as shown in Figure 6.10. Pictures of the cuvette were taken with the nanofluid at the initial stage, after 4 h and after the redispersion at 300 °C. When the particles are suspended in the fluid and well dispersed, the nanofluids look uniform and, in the case of the Al/Cu, completely dark. As the particles agglomerate and start to settle, they move to the bottom of the cuvette and the fluid above becomes clearer. Finally, after the redispersion, the nanofluids should look homogeneous and similar to the initial stages as it can be noticed for both nanofluids, although only the Al/Cu nanofluid recovers its initial particle size distribution.
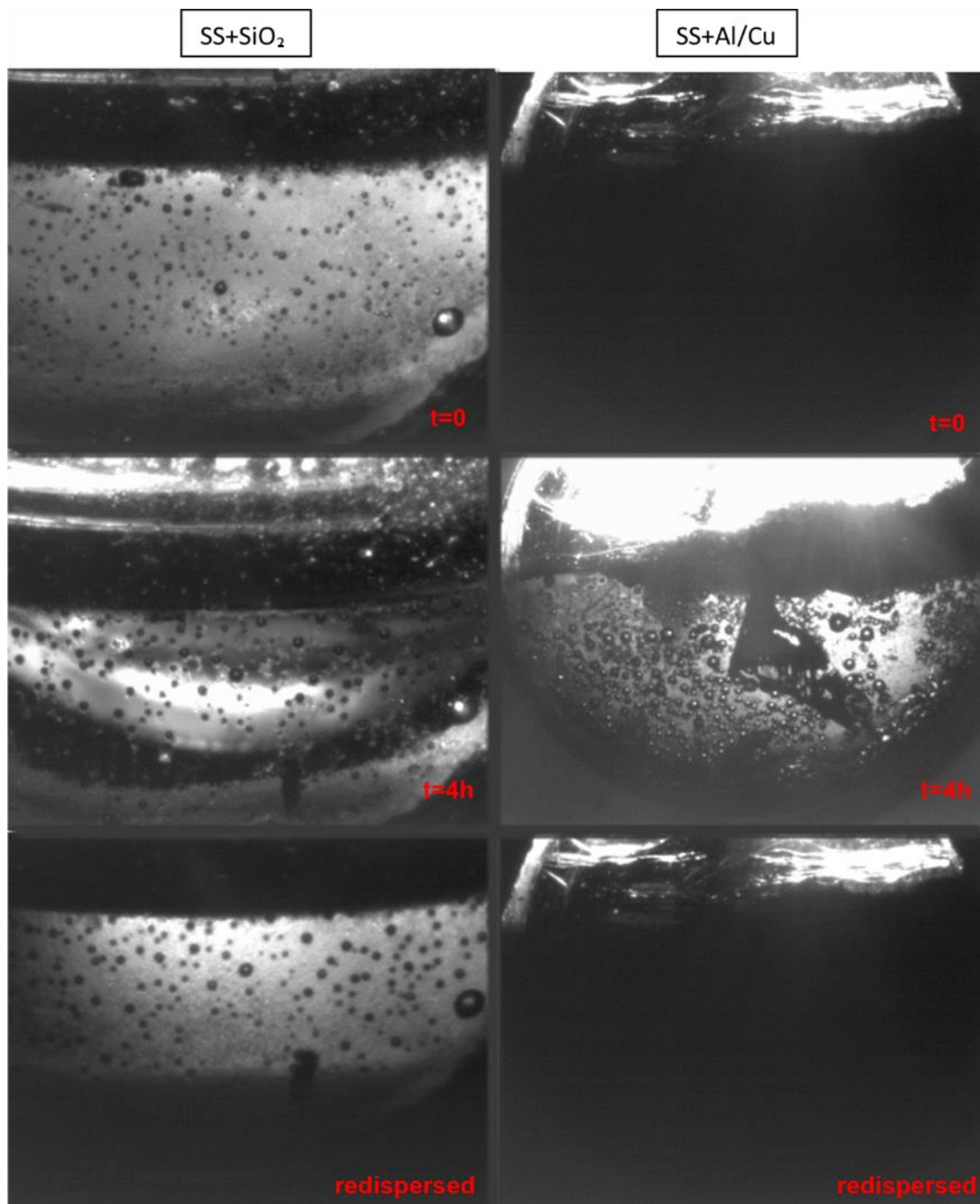
Figure 6.10. Evolution of nanofluid visual sedimentation through time and with redispersion at 300 °C.

6.5 CONCLUSIONS

A new system suitable to measure the particle size distribution of nanoparticles suspended in a base fluid at high temperature conditions was set-up and calibrated. The system is composed of an external DLS device and a new cuvette specially designed to work up to 500 °C and compatible with molten salts.

The particle size distributions of silica nanoparticles dispersed in water and calcium nitrate tetrahydrate were measured from room temperature to 80 °C and compared to experimental results obtained in a low temperature DLS equipment commonly used in the literature. The good agreement between the results from both systems corroborate the suitability of the new high temperature DLS for the measurement of molten salt-based nanofluids.

This device has allowed the measurement of the colloidal stability of molten salt-based nanofluids for the first time. It was observed how silica nanoparticles agglomerate when dispersed in the different based fluids which have been tested: water, calcium nitrate and solar salt. The high ionic strength of the molten salts and the reduced Debye length lead to the formation of agglomerates due to the importance of the attraction forces over the electrostatic repulsion.

The evolution of the particle size distributions of molten solar salt containing silica and Al/Cu nanoencapsulated phase change material was measured for 4 h and after mechanical redispersion of the nanofluid at two different temperatures, 250 °C and 300 °C. For both nanofluids, there are initial agglomerates bigger than the colloidal stability limit previously calculated, which indicates the settling of the agglomerates. Stability curves and imaging over time corroborate the lack of stability of both nanofluids, although their initial particle size distributions were recovered after mechanical redispersion at 250 °C. Besides, the Al/Cu nanofluid presented smaller agglomerates than the silica nanofluid, it also shows lower agglomeration rate and the initial particle size distribution was recovered after redispersion of the sample at 300 °C.

Chapter 7: IMPROVED THERMAL ENERGY STORAGE OF NANO-ENCAPSULATED PHASE CHANGE MATERIALS BY ATOMIC LAYER DEPOSITION

Renewable energy has become of great interest over the past years in order to mitigate Global Warming. One of the actions gaining attention is the enhancement of the thermal energy storage capacity of concentrated solar power plants. The addition of nanoencapsulated phase change materials (core-shell nanoparticles) to the already used materials has been proposed for that purpose, due to the possibility of increasing thermal storage through the contribution of both core latent heat and sensible heat. In this work, atomic layer deposition has been used to synthesise SiO_2 and Al_2O_3 nanoscale coatings on tin nanoparticles. The multi-encapsulated phase change materials have been characterised in terms of chemical composition, crystalline structure, particle size, thermal stability and thermal storage capacity. $Sn@Al_2O_3$ nanoparticles present the best thermal behaviour as they show the lowest reduction in the phase change enthalpy over 100 cycles due to the oxidation barrier of the coating. Moreover, the specific heat of both nanoparticles and solar salt-based nanofluids is increased, making the nanoencapsulated phase change material suitable for thermal energy storage applications.

7.1 INTRODUCTION

The general trend in the energy field is moving towards renewable energy. One of the key issues for its use is improving the possibilities for energy storage, in order to overcome the intermittencies of availability of the energy sources[60,104]. In the case of concentrated solar power (CSP) plants, the most featured mechanism for this purpose is the installation of a thermal energy storage (TES) system based on two tanks of molten salts, one hot and one cold, that can keep the plant active when there is no sunlight available[63,105].

Also very important in the storage of thermal energy is the use of phase change materials (PCMs)[106–108]. These materials have high phase change enthalpies, that is to say, they absorb a considerable amount of energy in order to melt, and this energy remains stored within the material until it is released to the medium again when the PCM solidifies. Among the different kinds of existing PCMs, metals and metallic alloys generally present some advantages. Besides high latent heat, they normally have high thermal conductivity, which makes energy charge and discharge cycles faster[109].

Although the most studied applications for PCMs so far are as TES technologies in solar thermal and waste heat energy, their interest is increasing in other industrial areas such as thermal regulation in photovoltaic-thermoelectric systems, products that require low-temperature storage, electronic parts that are temperature-sensitive, energy saving in thermoregulated building materials or textiles, etc.[110].

Regarding their use in energy storage, one way to introduce metallic PCMs as a heat storage medium within the current TES technologies, such as molten salts storage in CSP, is the use of nanofluids with PCMs as nanoparticles dispersed in the salts. Nanofluids are colloidal suspensions of nanometric particles, which allow to partially include the physical properties of a solid, while keeping the transport properties of the fluid to a certain extent. The key issue with nanofluids is that, given the small size of the particles, they can remain suspended within the fluid instead of settling, as the Brownian motion can overcome gravity forces[25,42].

Therefore, a nanofluid containing molten salts as the base fluid and metallic PCMs as the solid nanoparticles could serve as an enhanced way of thermal storage, contributing with the addition of the latent heat storage provided by the nanoencapsulated PCM (nePCM) cores. Moreover, in this application, metallic nanoparticles also present the advantage of their high density, which allows for considerable improvements in the thermal properties (that depend on the mass loading), without excessively increasing the viscosity (that depends on the volumetric concentration). Besides the latent heat storage capacity, the addition of nanoparticles to molten salts has been proved to increase the sensible heat storage capacity of the mixture due to the interactions between the nanoparticle and the fluid[22,23,69]. For this reason, both the phase change enthalpy and specific heat of the nanoparticles and nanofluids need to be optimized for thermal storage applications.

However, it must be considered that in order to use a PCM as the solid phase in a nanofluid the nanoparticles must have a core-shell structure, i.e., the PCM must be encapsulated by a high melting point material, which will prevent the different particles from collapsing into each other when the PCM is melted[31,32,111]. Metallic nanoparticles usually present a native thin oxide layer formed by passivation in contact with air, which can serve as self-encapsulation in some cases[78,112]. Nevertheless, further oxidation of the cores material can occur due to interactions with the base fluid or when the particles are exposed to high temperatures or thermal cycling,

decreasing the energy stored through latent heat by the nePCMs. Therefore, this work deals with the possibility of engineering a multi-layered encapsulation of the particles, synthesising a second nanoscale coating of an insulating material using atomic layer deposition.

Atomic layer deposition (ALD) is a gas-phase deposition technique[113] that has been utilised for the alteration of surface properties of both micron- and nano-sized metallic particles with minimal influence of their bulk properties. The uncoated nanoparticles are cyclically exposed to two gaseous precursors that chemisorb on their surface. A purging step is needed to remove the unreacted molecules after every exposure to the different precursors in order to avoid undesired gas-phase reactions between them. Hence, the deposition process is highly controlled, and films of a few nanometres whose thickness can be tuned by varying the number of cycles of precursor exposure can be synthesised. Processing of transition (Ni[114–119], Fe[116,117,120–123], Cu[116,123] and Co[116]) and post-transition metal particles (Al[117,124–126], Zn[117] and W[127] has been reported through ALD. Several oxide (Al_2O_3[114–117,119–121,123,127], TiO_2[116,118,122], SnO_2[124,125], Fe_2O_3[126], and ZnO[125]), nitride (BN[117]) and composite (Al_2O_3/ZnS[120] and AlN/TiO_2[122]) ALD coatings have been deposited; for an overview see Miikkulainen et al.[128]. Different ALD processes have different values for the growth-per-cycle (GPC). For the case of Al_2O_3 synthesised using trimethylaluminium (TMA) and water the values range between 0.1-0.2 nm[127]. Due to the oxidation avoidance prerequisites, relatively mild processing conditions in terms of temperature (up to 350 °C) and co-reactant reactivity (mostly H_2O or H_2O_2) are preferred. Agitated reactor vessels such as fluidised beds[114,129] and rotary reactors [123,127] provide favourable coating conformality and uniformity characteristics as compared to viscous flow[125] or flow-type[118] reactors.

In this work, the aim is to deposit SiO_2 and Al_2O_3 coatings on commercial Sn nanoparticles with a thin SnO_x passivating layer by using fluidised bed ALD. The presence of the nanolayer and its chemical composition were determined in order to evaluate the performance of the ALD technique to coat this kind of material. Finally, the performance of the ALD coatings, which are meant to prevent the further oxidation of the nePCM cores when exposed to working conditions, such as interaction with the base fluid or thermal cycling, has been tested through thermal characterisation of the enhanced nePCMs and the solar salt-based nanofluids containing them.

7.2 MATERIALS AND METHODS

7.2.1 Materials

Commercial Sn nanoparticles of nominal size <300 nm were purchased from US Research Nanomaterials, Inc. These nanoparticles were produced by the electro-physical fumed combined with strong airflow injection method. The phase change enthalpy and temperature for bulk Sn are 59.2 kJ/kg and 232 °C respectively.

Regarding the ALD process, the Al precursor, trimethylaluminium (TMA), was purchased from Akzo Nobel HPMO in a 600 ml stainless steel bubbler canister. The Si precursor, silicon tetrachloride ($SiCl_4$), was purchased from Sigma-Aldrich. Demineralised water was used as a co-reactant for both SiO_2 and Al_2O_3 ALD. All the precursors were contained in stainless steel bubblers and used as received.

For the synthesis of the solar salt-based nanofluids, a mixture of sodium and potassium nitrates, in a 60:40 wt.% proportion was used. The nitrates were purchased from Labkem

(Analytical grade ACS), weighted in the desired proportions and mechanically blended with the nanoparticles in a 1 wt.% concentration. Any trace of humidity from the salts was previously removed by placing the nitrates in an oven at 100 °C for 20 min.

7.2.2   ALD experiments

The coating experiments were carried out in an atmospheric-pressure fluidised bed reactor, consisting of a glass column with an internal diameter of 2.6 cm and a height of 50 cm. The reactor was placed on a double-motor vibration table (Paja PTL 40/40–24) operated at a frequency of 40 Hz to assist the fluidisation of the nanoparticles. Two stainless steel distributor plates with pore size of 37 µm, placed at the bottom and the top of the column, were used to ensure a homogeneous gas distribution and to prevent any particle leakage from the reactor, respectively. The ALD precursors, i.e., TMA, $SiCl_4$ and H_2O, were kept at room temperature. The precursors were delivered to the reactor through two separate lines using nitrogen (N_2, 99.999 v.%) as a carrier gas; a third line for the purging gas was also connected to the reactor. The lines were kept at 30 °C above the bubbler temperatures to prevent any precursor condensation by using heating tapes placed around them. The reactor was heated by an infrared lamp with a feedback control to maintain the desired reaction temperature of 40 °C. The temperature of the powder bed was monitored by a type-K thermocouple inserted in the reactor. The off-gas of the fluidised bed was led through a series of washing bubblers containing mineral oil (Kaydol) to trap unreacted precursors and reaction by-products, and NaOH solution to neutralise chloride compounds arising from $SiCl_4$. The precursor bubblers, the lines, the reactor and the washing bottles were contained inside a closed cabinet. In case of Al_2O_3 ALD, the cabinet was blanketed with nitrogen and operated at an O_2 concentration below 6% as a safety measure. An ALD cycle consisted of sequential exposures of $SiCl_4$–N_2–H_2O–N_2 for SiO_2 ALD, and TMA-N_2-H_2O–N_2 for Al_2O_3 ALD. Table 7.1 shows the exposure times for each precursor step. In each experiment, 20 g of Sn nanopowder were loaded in the reactor and fluidised with a flowrate of 1 NL/min. Each deposition process was run for 50 cycles. At the end of the 5th, 10th and 25th cycles, the experiment was stopped, and around 1 g of powder was sampled and stored for characterisation.

Table 7.1. Experimental parameters of the ALD process.

ALD Process	Reaction Temperature (°C)	Precursor Exposure Time (min)	Number of cycles
SiO₂ ALD	40	0.5 ($SiCl_4$) -5 (N_2) -1 (H_2O) -5 (N_2)	5, 10, 25, 50
Al₂O₃ ALD	40	1 (TMA) -5 (N_2) -1 (H_2O) -5 (N_2)	5, 10, 25, 50

7.3   CHARACTERISATION TECHNIQUES

7.3.1   Scanning electron microscopy, SEM

A general view of the different samples was obtained with a scanning electron microscope (SEM, JEOL-JSM 6510). The morphology and size of the nePCMs was observed and their composition was analysed using the integrated EDX module (Oxford INCA).

7.3.2   Field emission transmission electron microscopy, TEM

A field emission transmission electron microscope JEM 2100F (JEOL) operating at an accelerating voltage of 200 kV was used for the visualisation of the size, morphology and film thickness of the different nePCMs.

The microscope comprises a high resolution CCD camera (SC200, GATAN), and is equipped with a STEM unit with the bright field imaging detector and the high-angle annular dark-field (HAADF) detector, which enables the observation of contrast in phases with different atomic numbers. Chemical characterisation can also be performed by the EDX X-Max 80 detector (Oxford Instruments) to determine the elemental composition of the coated nanoparticles.

7.3.3 Inductively coupled plasma mass spectrometry, ICP-OES

The mass loading of Al and Si in the coated samples was measured by inductively coupled plasma optical emission spectrometry (ICP-OES). Approximately 30 mg of the sample were destructed in 4.5 ml 30% HCl +1.5 ml 65% HNO3 + 1 ml 40% HF using a microwave oven. The destruction time in the microwave oven was 60 min at maximum power. After destruction, the samples were diluted to 50 ml with MQ H_2O. The destructed samples were analysed with a PerkinElmer Optima 5300DV and PerkinElmer Optima 4300DV (PerkinElmer, Waltham, MA, USA) optical emission spectrometers to determine the content of Al and Si, respectively.

7.3.4 Fourier-transform infrared spectroscopy, FT-IR

The chemical composition of the different samples was analysed using a FT/IR-6200 spectrometer (Jasco) with a spectral window of 4000–400 cm^{-1} in transmission mode. A small amount of sample (~1 wt.%) was mixed with KBr (IR spectroscopy grade, Scharlab SL), grounded and pressed into pellets of 13 mm of diameter.

7.3.5 X-ray powder diffraction, XRD

The composition and crystalline structure of the nePCMs with different coatings was analysed using a Bruker D8 X-ray diffractometer with Cu Kα radiation by studying the angles from 2θ = 5° to 2θ = 80° with a 0.02° step. Spectra were registered at 30 °C, after 30 min at 280 °C and again after cooling down to 30 °C in order to determine the possible changes in the crystalline structure of the nePCMs when subjected to high temperature and thermal cycling.

7.3.6 Dynamic light scattering, DLS

The particle size distribution of the different nePCMs suspended in water was studied with a VascoFLEX particle size analyser (Cordouan Technologies). The device consists of an external laser head that contains the light emitter and receiver (65 mW-658 nm fiber pigtailed laser). The light registered corresponds to backscattering with an angle of 170°. In order to measure the particle size distribution closer to the primary size, avoiding the formation of agglomerates, a very dilute suspension was prepared with 32 mg of each nePCM added to 40 ml of distilled water. The nanofluids were sonicated during 5 min (Sonopuls HD2200, Bandelin electronic GmbH & Co.) and DLS measurements were carried out in a quartz cuvette of 2 ml. Three measurements were taken of each sample to ensure repeatability.

7.3.7 Thermogravimetric analysis, TGA

Changes on the oxidation state have been studied for all the nePCMs with thermogravimetric analysis. A TGA 1 (Mettler Toledo) was used with air atmosphere. The temperature of each sample was kept at 70 °C for 5 min, then raised to 280 °C at a 5 °C/min rate, and held at 280 °C for 30 min, while measuring all the changes in mass taking place. Approximately 20 mg of sample were introduced in an aluminium crucible for each test.

7.3.8 Differential scanning calorimetry, DSC

Information about the melting temperatures and phase change enthalpies of the nePCMs was obtained by differential scanning calorimetry (DSC2, Mettler Toledo). Samples of around 20 mg

were analysed in 40 µl aluminium crucibles. They were studied from 70 °C to 280 °C and back to 70 °C with heating and cooling rates of 5 °C/min and 5 min isothermal steps at the minimum and maximum temperatures. The samples were also subjected to thermal cycling, repeating this program 100 times. All these tests were performed under inert atmosphere, with a constant 25 ml/min N_2 flow rate.

The nePCMs were also subjected to 5 thermal cycles under air atmosphere to evaluate the influence of oxygen exposure on the thermal properties.

Heat impact resistance of the nePCMs was studied by submitting the samples to fast thermal cycles. Two initial cycles from 70 °C to 280 °C and back to 70 °C with heating and cooling rates of 5 °C/min and 5 min isothermal steps at the minimum and maximum temperatures were applied to check the initial behaviour. Then they were subject a similar cycle with heating and cooling rates of 100 °C/min. The samples were then exposed to air atmosphere, so if there was any leakage of the cores pure Sn it would oxidise, and later, two more slow thermal cycles were applied to observe the possible alterations in the nePCMs melting behaviour. This procedure was then repeated reaching a maximum temperature of 450 °C in the fast cycle.

The specific heat of the nePCMs and nanofluids based on their mixture with solar salt was also measured with DSC. The areas method[80] was used to study specific heat at 80 °C and 180 °C, when solar salt and nePCMs are still in solid state, at 280 °C, when both solar salt and the nePCMs cores are in molten state, and back at 180 °C, when the nePCMs cores are still melted due to supercooling but the solar salt has already solidified. A standard sapphire was tested prior to each sample, using the same cycle procedure, with a 1 °C step at each of the temperatures studied and 5 min isotherms before and after the step. All the specific heat tests were carried out with a constant 25 ml/min N_2 flow rate. In order to ensure repeatability at least three samples were prepared of each nePCM/nanofluid. For each one, two cycles were run in order to obtain a mean value. The experimental error was statistically obtained at a 95% of confidence level, with a mean error of 6.87% for the nePCMs and of 2.58% for the solar salt-based nanofluids.

A summary of the characterisation methods used can be found in Table 7.2.

Table 7.2. Summary of the tests performed over each sample.

			Sample						
Experiment	**Sn**	**Sn@SiO₂**				**Sn@Al₂O₃**			
# cycles	**0**	**5**	**10**	**25**	**50**	**5**	**10**	**25**	**50**
SEM + EDX	●				●				●
TEM + EDX (linear)	●				●		●		●
ICP-OES	●	●	●	●	●	●	●	●	●
FT-IR	●				●				●
XRD	●				●				●
DLS	●		●		●		●		●
TGA	●		●		●		●		●
Thermal cycling (5 cycles in air)	●		●		●		●		●
Thermal cycling (100 cycles, N₂)	●				●				●
Heat impact resistance	●				●				●
Specific heat	●				●				●
Specific heat with solar salt	●				●				●

7.4   RESULTS AND DISCUSSION

7.4.1   Morphology, encapsulation and chemical composition

The different nePCMs were visualised using SEM. In Figure 7.1, a general overview of the samples is depicted. It is observed that the particles are spherical in all the cases and the encapsulation process after 50 ALD cycles has no effect on the morphology of the particles.
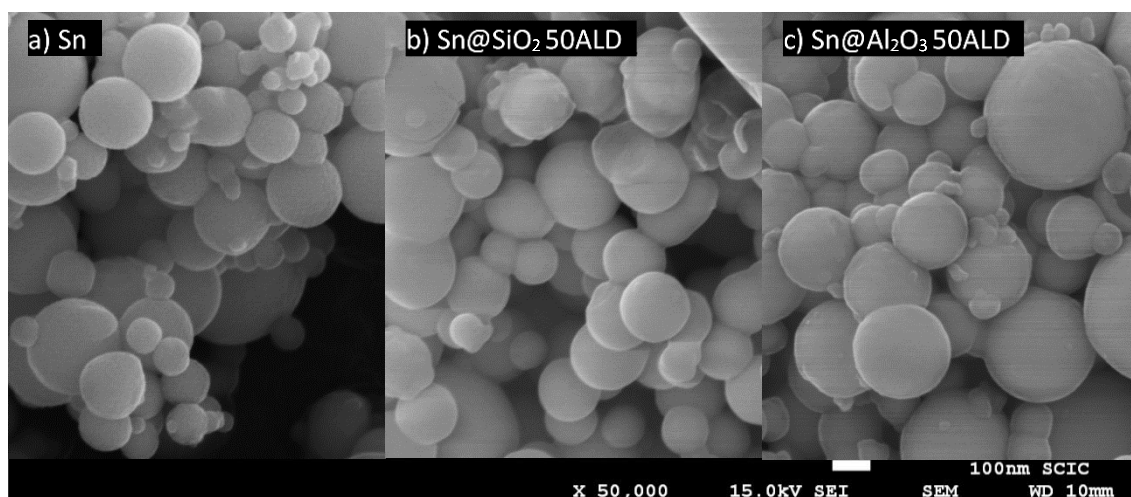

Figure 7.1. SEM micrographs of the nePCMs of (a) Sn, and (b) Sn@SiO₂ and (c) Sn@Al₂O₃, both after 50 ALD cycles.

Besides, Figure 7.2 shows the EDX analyses of all the nePCMs including the original Sn nanoparticles that already presented a passivation layer of SnO_x before the ALD coating. The peaks shown in light grey are corresponding to elements belonging to the SEM sample holder such as C, and N, and the Pt coating needed to run the analysis. Thus the elements composing the samples are determined to be Sn and O, in Figure 7.2 (a) corresponding to Sn nePCMs; Sn, Si and O, in Figure 7.2 (b), corresponding to the SiO_2 coated Sn nePCMs; and Sn, Al and O, in Figure 7.2 (c), corresponding to the Al_2O_3 coated Sn nePCMs. In Figure 7.2 (b), peaks corresponding to Cl also appear, attributed to a small quantity of residue from unreacted ALD precursors ($SiCl_4$).

The morphology of the SiO_2 and Al_2O_3 coatings on the Sn particles after 50 ALD cycles was studied using TEM. The multi-encapsulated particles can be observed in Figure 7.3, where the newly deposited material can be seen apart from the already present Sn cores and SnO_x passivation layer. A linear EDX analysis was performed for every nePCM, showing the composition of the different layers. Figure 7.3 (a) shows a particle of 200 nm with a Sn core, a SnO_x passivation film of 12 nm, and a second SiO_2 ALD film of 8 nm. In Figure 7.3 (b), the same dimensions can be observed for the particles coated with Al_2O_3, with a thickness of 10 nm of Al_2O_3 in this case. Such SiO_2 and Al_2O_3 film thicknesses translate into GPCs of 0.16 nm and 0.2 nm, respectively, which are in agreement with the values reported in literature[127,130]. Both oxide ceramic coatings of SiO_2 and Al_2O_3 are very conformal, and fully confine the nePCM with a constant layer thickness.

In addition to the EDX analysis, the presence of SiO_2 and Al_2O_3 on the coated nePCMs was also confirmed by FT-IR. As can be seen in Figure 7.4, after the coating process new peaks appear in the infrared spectra corresponding to the SiO_2 and Al_2O_3 bonds[131]. In particular, the signatures of SiO_2 are featured by the two peaks in the wavenumber range of 1125–1200 cm⁻¹, while Al_2O_3 gives the stretching at 912 cm⁻¹, characteristic of Al–O[132].

69
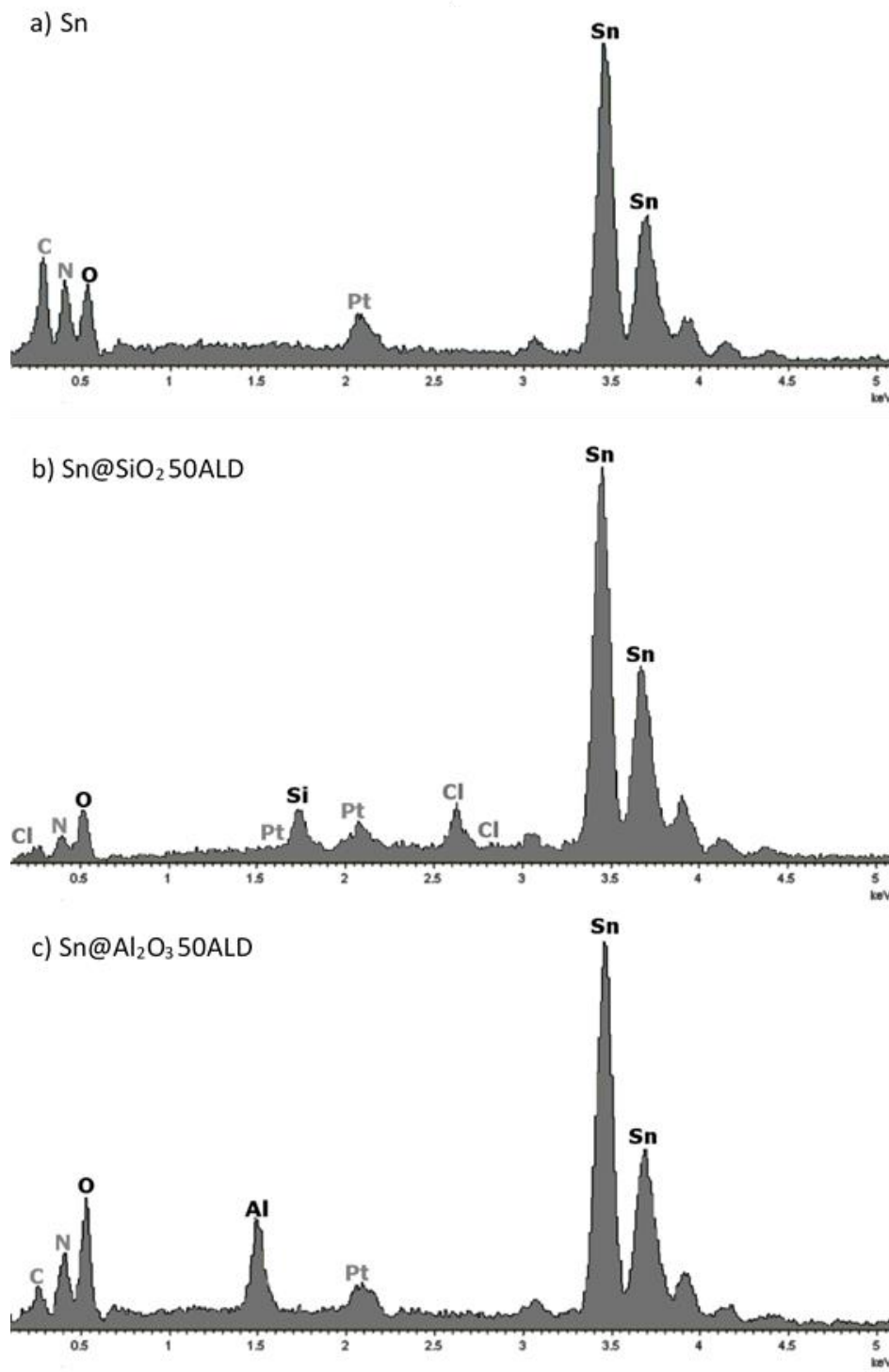
Figure 7.2. EDX analysis of the nePCMs of (a) Sn, (b) Sn@SiO₂ after 50 ALD cycles and (c) Sn@Al₂O₃ after 50 ALD cycles.

The composition of the ALD coated samples was studied with ICP-OES. The mass percentages of Al and Si were measured and converted to Al_2O_3 and SiO_2 mass percentages using stoichiometry relations. The results of this analysis are plotted in Figure 7.5. The weight content of both SiO_2 and Al_2O_3 in the multi-coated nePCMs linearly increases with the number of cycles. In particular, the maximum fraction of Al_2O_3 and SiO_2 in the samples after 50 ALD cycles was 3 wt.% and 1.3 ± 0.3 wt.%, respectively.
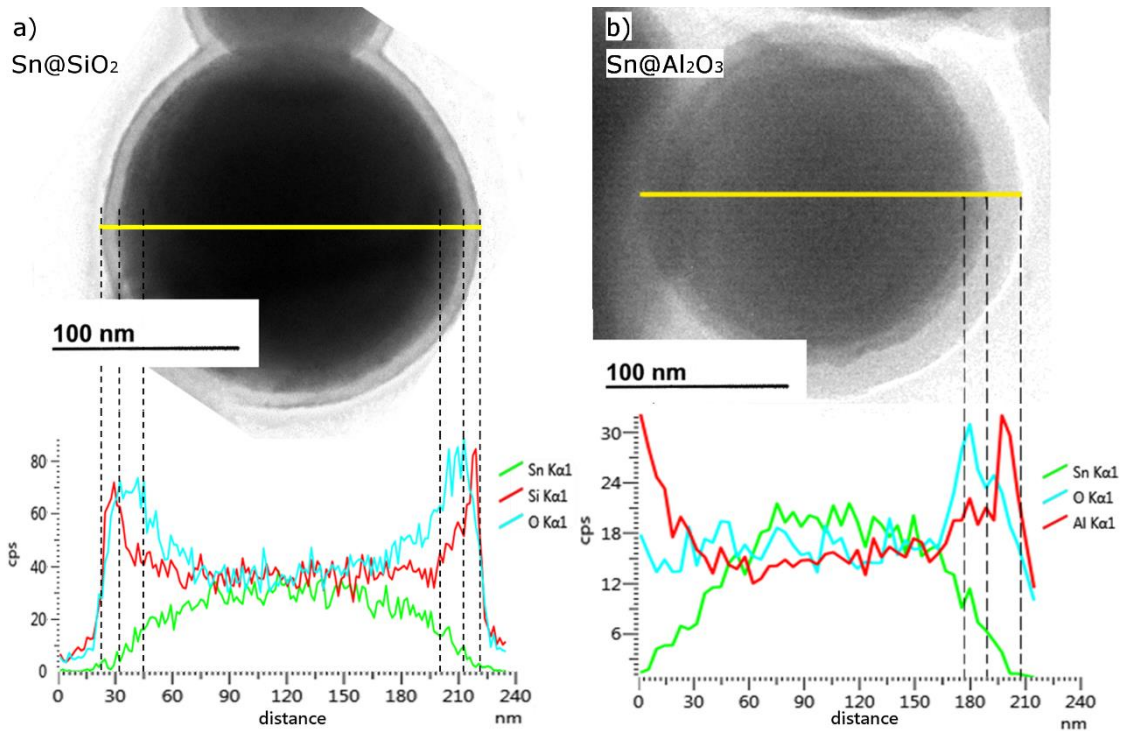
Figure 7.3. TEM images and EDX analysis of (a) SiO$_2$ and (b) Al$_2$O$_3$ coated Sn nePCM.
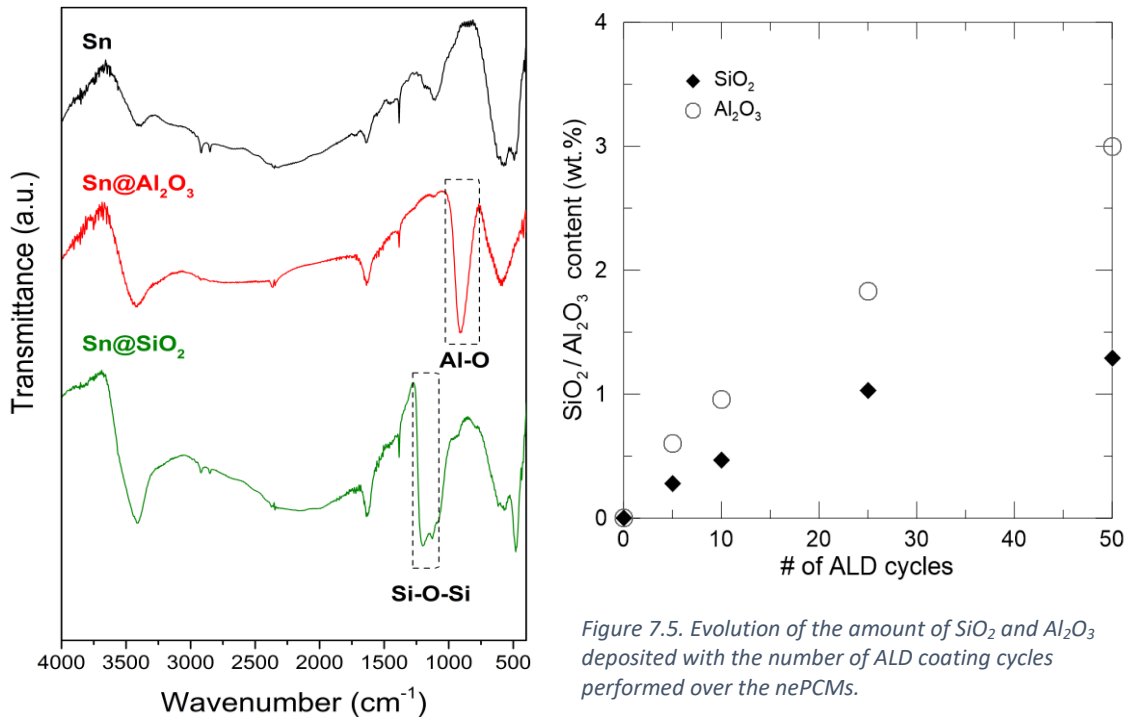
Figure 7.4. FT-IR spectra of the different nePCMs.

Figure 7.5. Evolution of the amount of SiO$_2$ and Al$_2$O$_3$ deposited with the number of ALD coating cycles performed over the nePCMs.

The different crystallographic phases present in the Sn@SiO$_2$ and Sn@Al$_2$O$_3$ samples were studied by X-Ray diffraction. The samples were analysed initially at 30 °C, then the temperature was raised to 280 °C, and then they were analysed again at 30 °C. The results of the diffraction are shown in Figure 7.6.

71
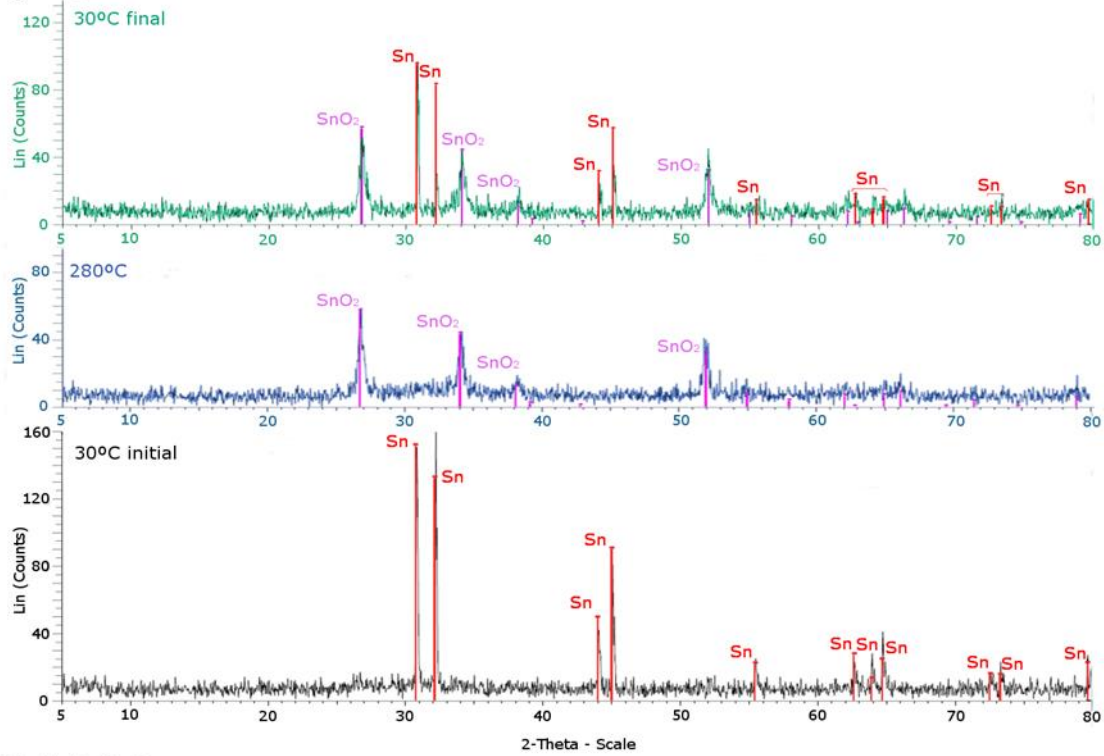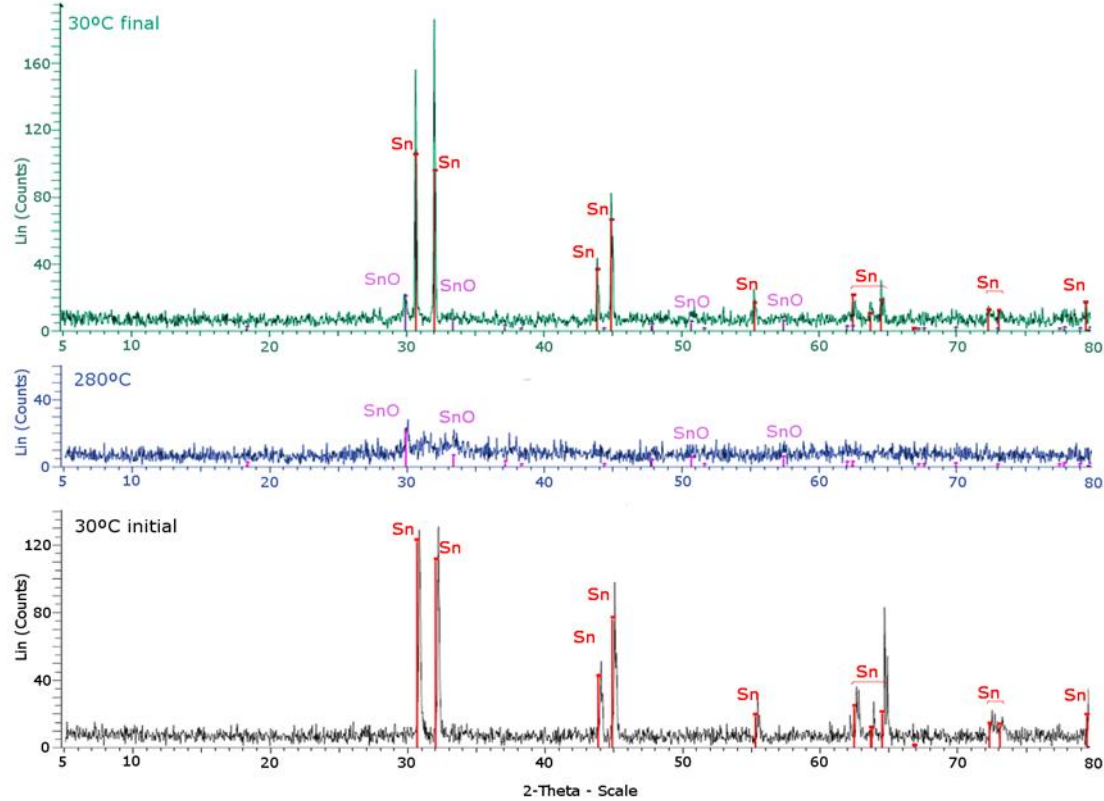
Figure 7.6. XRD diffractograms of the (a) SiO₂ and (b) Al₂O₃ coated nePCMs.

For the Sn@SiO₂ nePCMs, it can be observed that initially only the peaks belonging to pure Sn cores appear, therefore it is crystalline, while the SnO_x and SiO_2 of the multi-layered encapsulation are amorphous. After the heating of the sample at 280 °C, the core material is melted, and thus it does not appear in the diffractogram. However, it can be noticed that the

SnO$_x$ layer has crystallised and its structure is that of SnO$_2$, unlike that of the initial Sn@SnO particles[78]. This change on the oxidation state is assumed to take place due to the SiO$_2$ coating, since it does not occur for the Al$_2$O$_3$ coated nePCMs. Finally, after the sample was cooled back down to 30 °C, both Sn and SnO$_2$ peaks appear, while SiO$_2$ is still amorphous.

The results obtained for the Sn@Al$_2$O$_3$ nePCMs are similar. Initially, only the Sn cores are crystalline at 30 °C. After heating the sample at 280 °C the tin oxide layer crystallised to SnO, and both Sn and SnO spectra are present after the cooling down of the sample to 30 °C. Therefore, it can be determined that both the SiO$_2$ and the Al$_2$O$_3$ coatings deposited on the Sn nePCMs are amorphous.

7.4.2 Particle size

The possible alterations of the nePCMs size or sintering of the nePCMs during the ALD process was studied by dispersing a very small amount of the different samples in water and analysing the suspensions with DLS. The particle size distribution of the nePCMs coated with 10 and 50 ALD cycles was measured to assess the effect of the processing time on the particles. Figure 7.7 shows the results of the DLS analysis. The particle size distribution of all of the samples studied, regardless of the coating or the number of cycles, show two different intensity peaks. The first one corresponds to particles of around 180 nm, the mean diameter of the

Figure 7.7. Particle size distribution of the nePCMs in water.

Sn nePCMs[78]. The second one ranges from 600 to 800 nm, and it corresponds to clusters of particles. However, this peak is also present for the Sn nePCMs before the coating process, therefore it corresponds to the agglomeration of the particles because of attractive forces. Moreover, the difference between the mean peak sizes of the samples coated for 10 and 50 cycles is minimal, proving the ALD coating process did not impact the size or the agglomeration state of the nanoparticles.

7.4.3 Thermal stability

In order to test the thermal stability of the multi-coated nePCMs, a TGA analysis on air was performed on the samples. Their behaviour when exposed to a progressive increase of temperature from 70 °C and a posterior isotherm at 280 °C is shown in Figure 7.8.

It is observed that the Sn nePCMs sample loses some mass at the beginning, likely corresponding to impurities present on the commercial nanoparticles (e.g. additives like anti-agglomerants commonly used in industrially produced powders). Above 200 °C the mass starts to increase in a rather constant way. This is a sign that the nePCMs cores are oxidizing further than the initial passivation layer of SnO. This mass uptake would be a drawback for the application of these materials as a latent heat storage medium when in contact with air.

For the ALD coated nePCMs, an initial weight loss is also present. Apart from the previously mentioned impurities of the commercial nanoparticles, some residual products can be present

after the ALD coating, e.g. chlorine compounds from SiCl$_4$ after the SiO$_2$ coating (presence of Cl has been detected in the EDX analysis performed and shown in Figure 7.2), and carbonaceous species from TMA after the Al$_2$O$_3$ ALD. Precursor ligand leftovers that result in a small weight loss when subject to TGA have been previously reported in the literature[133,134]. However, the weight percentage of these impurities is very low (i.e., 0.3% mass loss difference between Sn and Sn@SiO$_2$ nePCMs), especially when compared to the deposition rates of the coating films previously shown in Figure 7.5. By optimising the deposition conditions, especially with regard to the second ALD half-reaction step, the influence of residual compounds of the precursor molecule on the coating quality could be further reduced.
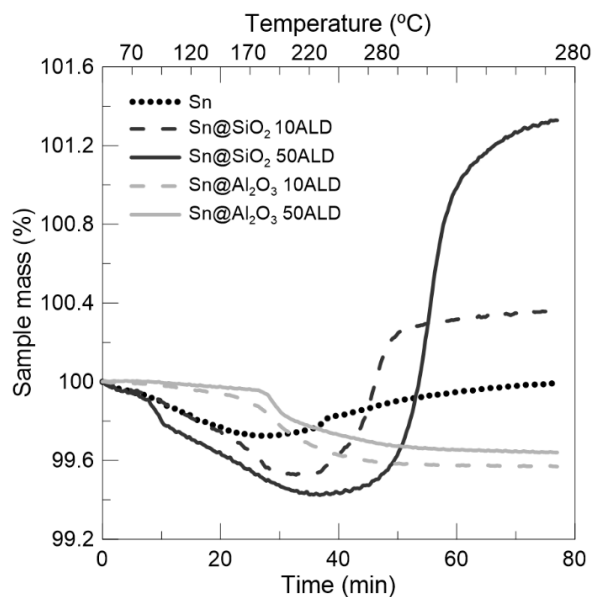
Figure 7.8. TGA analysis of the different nePCMs.

After the initial weight loss, a more prominent mass gain than that of Sn nePCMs can be observed in the isothermal segment at 280 °C for the SiO$_2$ coated nePCMs. Although this could be initially attributed to the oxidation of the cores as in the previous case, it has also been observed in the XRD analysis in Figure 7.6 that the tin oxide present in the Sn@SiO$_2$ nePCMs is SnO$_2$ instead of SnO. Therefore, this mass gain taking place can be related to the change on the oxidation state.

As for the Sn@Al$_2$O$_3$ samples, the behaviour of the samples during the isothermal segment at 280 °C is very stable, which indicates that the cores are not oxidizing and therefore the latent heat due to the melting of the cores remains constant.
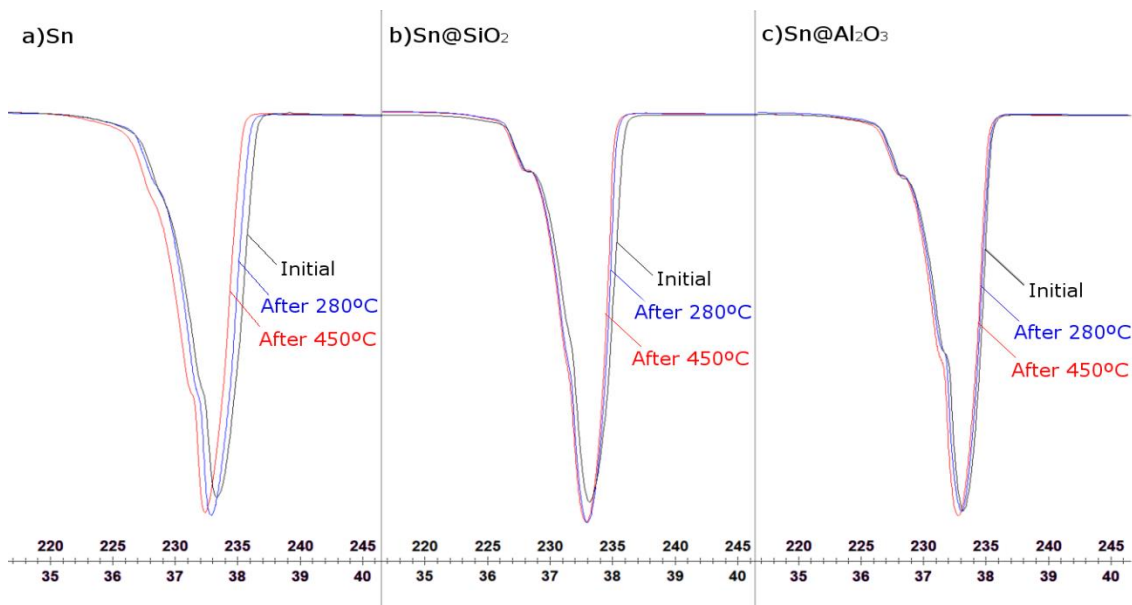
Figure 7.9. Heat impact resistance analysis. Comparison of the samples fusion peaks after thermal cycles of 100 °C/min up to 280 °C and 450 °C.

Heat impact resistance of the nePCMs was also tested. The samples were subject to two fast thermal cycles (with heating/cooling rates of 100 °C/min), first up to 280 °C, and later up to 450 °C to check if the encapsulation could resist. In Figure 7.9, a comparison between the initial fusion peaks and the peaks after these heat impact cycles is depicted for each nePCM. The variation present in the fusion peaks of Sn is very small, although a certain displacement appears. However, if the nePCM could not withstand the thermal cycle applied, that would result in the breakage of the encapsulations and leaking of the core material, which would oxidise in contact with air causing a notable decrease in the fusion enthalpy that is not observed for any of the samples. The differences observed between the initial and after the heat impact for the Sn@SiO$_2$ and Sn@Al$_2$O$_3$ samples are even smaller, which indicate that the nePCMs can resist fast temperature changes without losing their properties.

7.4.4 Thermal energy storage capacity

The latent heat of the nePCMs was analysed by means of DSC. A complete cycle of fusion and solidification within N$_2$ atmosphere of each of the samples after 50 ALD cycles can be observed in Figure 7.10 (a). It is noticed that the fusion temperature corresponding to the downward peak is constant for all samples studied, and thus not affected by the ALD process. This is also reflected in the values of the phase change enthalpies (Table 7.3), which are smaller for the multi-coated nePCMs. This behaviour was expected since this property depends on the ratio of pure Sn per gram of nePCM, which decreases after the samples are coated with SiO$_2$ or Al$_2$O$_3$. However, this decrease is not that significant, especially in the case of the Sn@Al$_2$O$_3$ sample.

In Figure 7.10 (b) a complete cycle of fusion and crystallisation after 100 thermal cycles is depicted for each of the samples. It is observed that the fusion temperature remains the same after the cycling and there are no significant changes in the overall curves thus confirming the stability of the samples to thermal cycling.

Regarding the crystallisation temperatures, clear differences can be noticed among the samples. The difference between the fusion and crystallisation temperatures is known as supercooling and depends to a great extent on the material and size of the PCM[52,78]. This difference occurs due to the lack of nucleation points for crystal growth during solidification, and, in this case, both Sn and Sn@Al$_2$O$_3$ have a similar crystallisation point, while Sn@SiO$_2$ shows a smaller value. One possibility for nucleation points are the imperfections in the
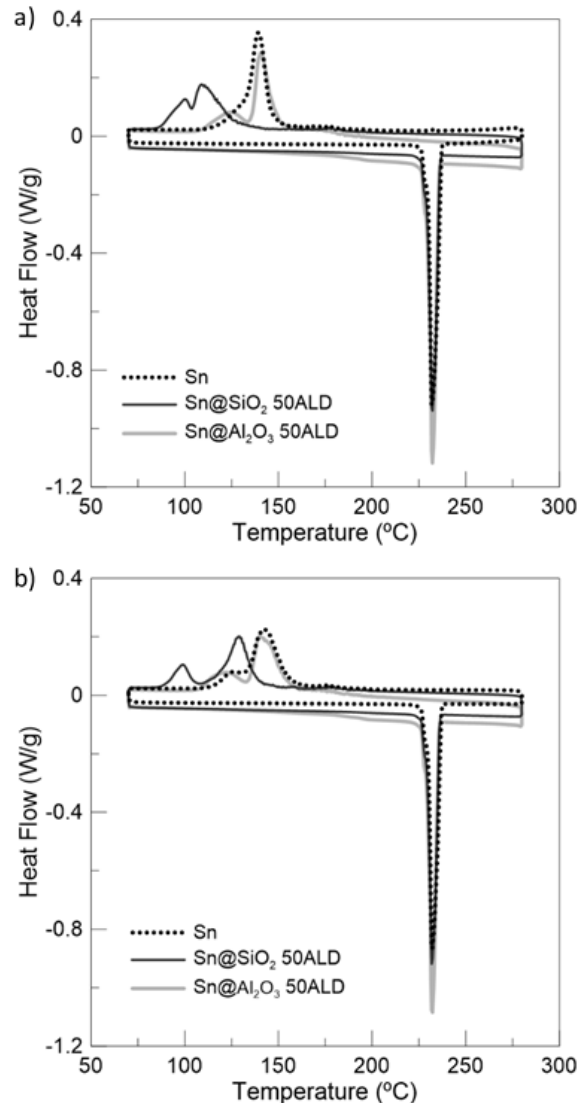
Figure 7.10. DSC fusion-crystallisation comparison of (a) 1st cycle and (b) 100th cycle.

interface between the nePCM core and the SnO_x layer. The difference in the temperatures could be the result of the different oxidation state of the passivation layers of the Al_2O_3 and SiO_2 coated nePCM (SnO and SnO_2 respectively), which could contain a lower number of defects in the structure for the SnO_2 interlayer, favouring the heterogeneous nucleation of the Sn crystals.

Table 7.3. Phase change data from the 1st cycle of DSC analysis of the nePCMs.

Sample	Phase change enthalpy (J/g)	Fusion Temperature (°C)	Crystallisation Temperature (°C)
Sn	52.99	232.00	139.48
Sn@SiO₂ 50ALD	48.71	232.75	123.38
Sn@Al₂O₃ 50ALD	51.74	232.99	143.22

The stability of the nePCMs to thermal cycling and the suitability of the different ALD coatings as an oxidation barrier were tested by subjecting the samples first to 5 thermal cycles up to 280 °C within an air atmosphere containing oxygen, and later, by exposing them to 100 cycles in an inert N_2 atmosphere. The evolution of the phase change enthalpy with the number of thermal cycles is plotted in Figure 7.11 and Figure 7.12, respectively.

In Figure 7.11, corresponding to the thermal cycling in air, it is noticeable that the SiO_2 coatings, instead of preventing the oxidation of the cores and loss of phase change enthalpy, seem to slightly promote it when compared to the uncoated Sn nePCM. However, Sn@Al_2O_3 samples show an enhancement in the resistance to oxidation, especially the one subjected to 50 ALD cycles, in which the phase change enthalpy remains almost constant during the 5 cycles, meaning that no oxidation of the pure Sn core is taking place even under oxidising conditions.

In Figure 7.12, corresponding to the 100 thermal cycles conducted under nitrogen, both ALD coated nePCMs show higher thermal stability than the uncoated Sn nePCMs. The decrease of the phase change enthalpy of the Sn nePCM, up to 7%, is considerably reduced in both Sn@SiO_2 and Sn@Al_2O_3 samples.
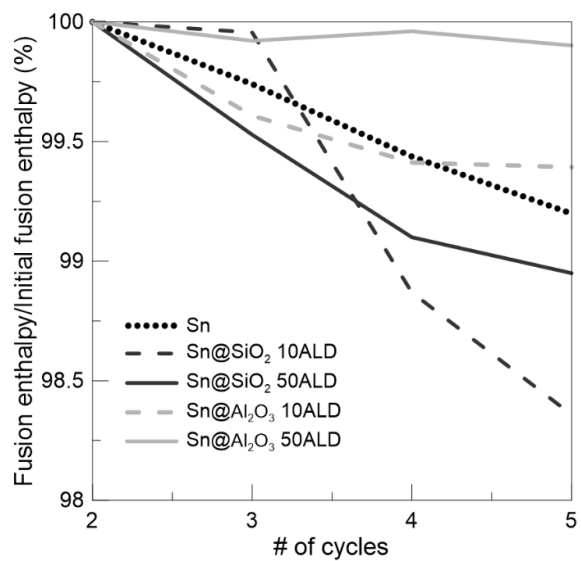
Figure 7.11. Evolution of the phase change enthalpy with thermal cycling in air atmosphere.
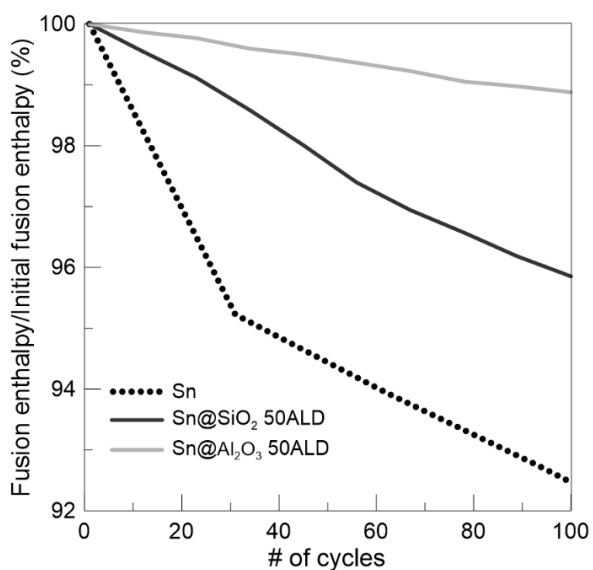
Figure 7.12. Evolution of phase change enthalpy with thermal cycling in nitrogen atmosphere.

The Sn@Al$_2$O$_3$ sample shows the best resistance to oxidation against thermal cycling, losing only a 1.1% of the initial phase change enthalpy, already higher than the previously obtained for the Sn@SiO$_2$ (4.1%).

Therefore, the nePCMs coated with Al$_2$O$_3$ present an overall enhancement in the oxidation resistance when exposed to thermal cycling, which implies a better performance of the nePCMs as a mean of latent heat storage in nanofluids.

Finally, the effect of the nePCMs on the specific heat of a solar salt-based nanofluid has been studied, since it is directly related to the sensible heat storage capacity of the material that is complementary to the latent heat. Figure 7.13 shows the values of the specific heat (c_p) of the different nePCMs and their nanofluids, prepared with a 1 wt.% concentration of particles and solar salt (SS) as the base fluid, along with their standard deviation. The variations in specific heat of the multi-coated nePCMs with respect to Sn nePCMs, and of solar salt-based nanofluids with respect to the base fluid alone are also shown in Table 7.4.
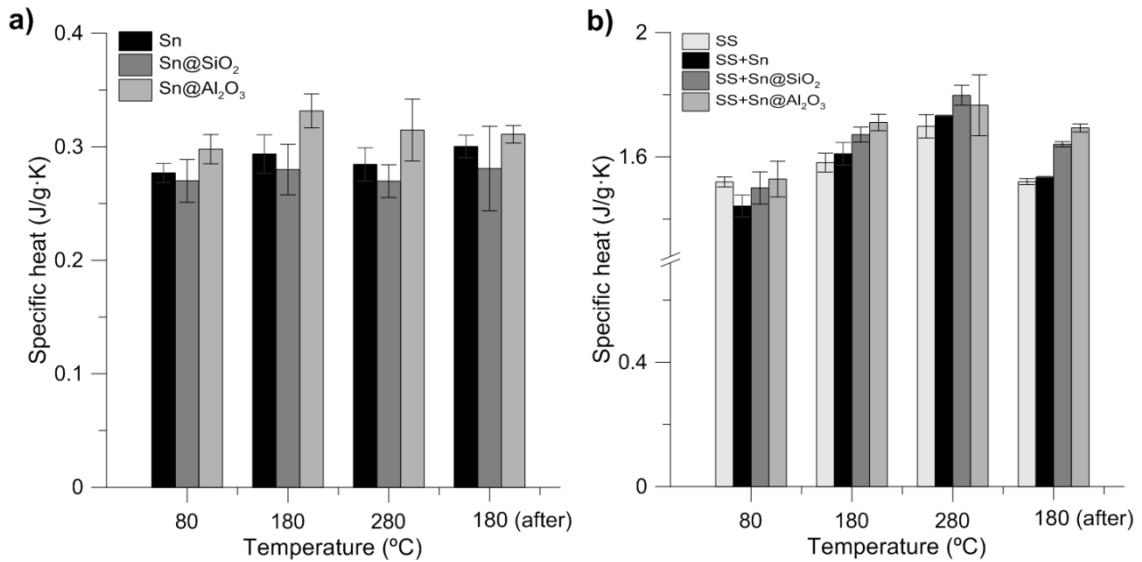
Figure 7.13. Specific heat of (a) nePCMs and (b) solar salt-based nanofluids at 1 wt.%.

The variations of the specific heat of the ALD coated nanoparticles are in a range from −6.5 to +12.9%, with opposite effects of the coating material. Whereas the SiO$_2$ coating seems to have a detrimental effect for the Sn@SiO$_2$ at every temperature studied, the effect of the Al$_2$O$_3$ coating in the Sn@Al$_2$O$_3$ samples is positive, where the specific heat increases by around 10% when increasing temperature.

Table 7.4. Specific heat variation for the nePCMs and the nanofluids at 1 wt.%.

T (°C)	80	180	280	180 (after)
Sample	Variation	Variation	Variation	Variation
Sn	-	-	-	-
Sn@SiO$_2$	-2.52%	-4.67%	-5.18%	-6.52%
Sn@Al$_2$O$_3$	+7.56%	+12.92%	+10.65%	+10.79%
SS	-	-	-	-
SS+ Sn	-5.09%	+1.79%	+2.02%	+0.99%
SS+ Sn@SiO$_2$	-1.26%	+5.69%	+5.88%	+7.93%
SS+ Sn@Al$_2$O$_3$	+0.62%	+8.16%	+3.99%	+11.38%

In the case of the nanofluids, all of the combinations show enhanced specific heats with respect to that of the solar salt, for the temperatures above 100 °C. This enhancement is greater than what could be expected from the mixture rule, as it has been previously observed in the literature for nanofluids based on molten salts[22,23,69]. The enhancement is also higher for the multi-coated nePCMs with respect to the nanofluid containing the uncoated Sn nePCMs through all the temperature range studied, which means that not only the sensible heat storage will not be damaged by the addition of the multi-coated nePCMs, but it can present an enhancement of up to 11.4%.

Thermal energy storage capacity is defined as the addition of sensible heat storage and latent heat storage. For any TES material it can be calculated as:

$$q_{total} = q_{sensible} + q_{latent} = m \cdot c_P \cdot \Delta T + m \cdot \Delta H \qquad \text{Equation 7.1}$$

where *m* refers to the mass of the material, c_p to its specific heat, *ΔT* to the temperature step studied, and *ΔH* to its phase change enthalpy.

The enhancement of the thermal energy storage of the nanofluids with respect to the base fluid alone has been calculated using the values of specific heat and fusion enthalpy of the nanofluids and the base fluid alone, previously measured, according to Equation 7.2.

$$\Delta q_{total} = \frac{m_{nf}\left(c_{P,nf} \cdot \Delta T + \Delta H_{nf}\right)}{m_{bf}\left(c_{P,bf} \cdot \Delta T + \Delta H_{bf}\right)} = \frac{\rho_{nf} \cdot V_{nf}\left(c_{P,nf} \cdot \Delta T + \Delta H_{nf}\right)}{\rho_{bf} \cdot V_{bf}\left(c_{P,bf} \cdot \Delta T + \Delta H_{bf}\right)} \qquad \text{Equation 7.2}$$

where the subscript *bf* refers to the base fluid properties, *ρ* is the density and *V* is the volume.

The thermal energy storage enhancement was compared assuming constant mass ($m_{nf} = m_{bf}$) and constant volume ($V_{nf} = V_{bf}$) of the TES material (nanofluid and base fluid, respectively) at the same working temperature (including the phase change) and with a mass loading of nePCMs of 1 wt.%. The results are presented in Table 7.5, where it is observed that the addition of nePCMs improves the thermal energy storage capacity for all the cases studied, due to a combination of the enhancement in the specific heat when adding nePCM and to the contribution of latent heat. Temperature steps of 150 °C, 180 °C and 200 °C have been studied according to working cycles possible in a real application. It can also be noticed that the higher increments are for the nanofluids containing the ALD coated nePCMs, that present a higher specific heat value and thus a higher sensible heat contribution than the combination of solar salt with Sn nePCMs. It is also remarkable that the enhancement is always higher for the ALD coated Sn@Al$_2$O$_3$ nePCMs, which in addition to the previously observed enhanced thermal stability will result in a promising alternative to the commonly used TES materials.

Table 7.5. Thermal energy storage enhancement of the nanofluids compared to the base fluid (SS).

Nanofluid	Constant mass			Constant volume		
	ΔT = 150°C	ΔT = 180°C	ΔT = 200°C	ΔT = 150°C	ΔT = 180°C	ΔT = 200°C
SS+ Sn	+0.28%	+0.36%	+0.41%	+1.05%	+1.13%	+1.18%
SS+ Sn@SiO$_2$	+6.63%	+6.77%	+6.86%	+7.33%	+7.48%	+7.56%
SS+ Sn@Al$_2$O$_3$	+9.42%	+9.64%	+9.77%	+10.12%	+10.35%	+10.47%

7.5 CONCLUSIONS

Multi-coated nePCMs consisting of Sn@SnO$_x$ nanoparticles coated with SiO$_2$ and Al$_2$O$_3$ have been synthesised by atomic layer deposition. The suitability of ALD to deposit uniform and conformal coatings with thicknesses of approximately 8 nm of SiO$_2$ and 10 nm of Al$_2$O$_3$ on the nanoparticles after 50 coating cycles was proved. The oxidation state of the native tin oxide on the nePCMs changed due to the ALD coating on the Sn@SiO$_2$ samples from SnO to SnO$_2$ when subject to high temperatures, while it remained as SnO in the Sn@Al$_2$O$_3$. Both SiO$_2$ and Al$_2$O$_3$ coatings were amorphous and retained their structure up to 280 °C. The resistance to the oxidation of the Sn core of the nePCM improved with the ALD coatings when the samples were subject to thermal cycling in nitrogen. This enhancement is especially high for Sn@Al$_2$O$_3$ samples, which also showed an enhanced resistance to oxidation under thermal cycling in an oxidising atmosphere. This results in an enhanced stability of the latent heat storage capacity of the nePCMs, which can be of use in nanofluids for thermal energy storage. The sensible heat storage capacity of the ALD coated nePCMs was tested by preparing nanofluids based on solar salt. The nanofluids prepared with the nePCM coated with 50 cycles of SiO$_2$ and Al$_2$O$_3$ showed an increase on their specific heat up to 11.4%. This, combined with the previously stated contribution of the nePCMs to latent heat, will translate into an overall enhanced thermal energy storage capacity of the nanofluids when the nePCM are coated, especially in the case of Al$_2$O$_3$ coated nanoparticles which allow for enhancements of up to 10.5% with respect to the solar salt.

Chapter 8: GENERAL DISCUSSION AND CONCLUSIONS

This thesis deals with different possibilities of thermal fluids for their use in the solar thermal energy industry. In particular, the focus has been in improving the thermal conductivity and thermal storage capacity of commonly used fluids by the addition of nanoencapsulated phase change materials. The nanofluids synthesised as a consequence are suitable for their use in medium- and high-temperature applications, providing a better thermal performance than their base fluids, which could result in a size reduction of the plant where they are used, or the improvement of its energy production capacity. The case of thermal energy storage is a key issue in the topic of renewable energies, since they usually present intermittencies in the availability of the energy source, which makes especially important the presence of a storage mechanism. Therefore, the increases of the thermal storage capacity resulting from the use of nanofluids could mean a significant advance for the future of concentrated solar power.

In this work, a compendium of four different journal articles is presented, each one dealing with different challenges related to the use of nePCMs in high temperature nanofluids for thermal applications. These challenges could be divided in three different categories: the synthesis of nanofluids that present an enhancement in thermal properties and their characterisation, the dealing with the particularities of the use of phase change materials at nanoscale, and the study of the issues associated with nanofluids at high temperatures. All three of these categories are extremely related through the different chapters in this thesis. For example, a nanofluid containing nePCMs cannot be thermally characterised if the compatibility between the nanoparticles and base fluid, and the resistance of the encapsulating shell to thermal processes (such as cycling) have not been ensured.

Some of the traditional challenges faced in the development of nanofluids based on nePCMs were met through the elaboration of this thesis. Among them, the complexity in the synthesis

of an encapsulation in order to have a core-shell structure in nePCMs was simplified by using metallic nanoparticles that already have a passivation oxide coating naturally formed during their production process or when they are exposed to air. On the other hand, the issue of supercooling was also dealt with, establishing non-eutectic metallic alloys as a good method to control this phenomenon. The achievement of these goals is listed next in detail:

- Naturally formed metallic oxide encapsulation can act as a suitable encapsulation method of pure metal cores in nePCMs. This lowers the cost of production since an oxide nanolayer is already present in many metallic nanoparticles due to passivation taking place during the production process.

- Encapsulations of SnO in Sn and Sn/Pb nanoparticles effectively serve to prevent the leakage of the core materials when they are melted.

- The encapsulation of Al/Cu cores with an Al_2O_3 passivation layer can resist the melting of the cores without breakage, proving its efficiency as nePCM.

- Sn@SnO and Al/Cu@Al_2O_3 nePCMs can be subject to thermal cycling that includes their melting and crystallisation temperatures while keeping their thermal properties stable.

- Non-eutectic metallic alloys can be tuned to control supercooling since when the cores are melted they often have solid remainders of one of the components in the alloy (with a melting temperature higher than the process) that act as nucleation spots during the crystallisation, reducing the difference of temperatures due to supercooling.

- Sn/Pb@SnO nePCMs can be tuned to control supercooling according to the maximum temperature reached in the thermal cycle.

- In Al/Cu@Al_2O_3 nePCMs, supercooling is very reduced, with very small differences between the melting and crystallisation temperatures, and they present high values of phase change enthalpy, that when included in nanofluids result in valuable enhancements of the thermal energy storage capacity, due to the contribution of latent heat storage.

The mentioned nePCMs were therefore established as suitable for their use in nanofluids as thermal properties enhancers. Hence, combinations with a synthetic thermal oil used in medium-temperature applications, and solar salt for high working temperatures were synthesised and tested as HTFs and TES materials, presenting improvements in their thermal capacities respect to their base fluids. The breakdown of the conclusions reached follows:

- Synthetic thermal oil and Sn nePCMs are chemically compatible.

- The nanofluids composed of the thermal oil TH66 and Sn nePCMs present enhancements of up to 22% in thermal conductivity, which are in accordance with Maxwell equation.

- The nanofluids composed of the thermal oil TH66 and Sn nePCMs present enhancements in the thermal storage capacity that are especially relevant for applications with a narrower cycling temperature range, since the contribution of

latent heat of the nanoparticles becomes more relevant (up to 37% enhancement for a 25°C temperature step).

- Solar salt and Al/Cu nePCMs are chemically compatible and no alterations occur even when the nanofluids are subject to thermal cycling. This is especially relevant since solar salt can present corrosion or interaction issues with some metals.

- Variations in the specific heat of the solar salt and Al/Cu nePCM nanofluids followed the trend observed in the literature for nanofluids based on ionic liquids. Hence, the bigger values of specific heat are obtained for mass loadings of nanoparticles around 1-1.5 wt.%.

- Thermal energy storage capacity can be enhanced through solar salt and Al/Cu nePCM nanofluids, especially when compared to the base fluid under a constant volume basis. This enhancement is higher for narrower cycle temperature ranges, since the contribution of nePCM latent heat becomes predominant (up to 18% enhancement for a 50 °C temperature step compared to the base fluid at constant volume basis).

- The nanofluids composed of solar salt and Al/Cu nePCMs with nanoparticle loadings of up to 1.5 wt.% present enhancements up to 9% in thermal conductivity, which are in accordance with Maxwell equation.

- This enhancement can result in an improvement of the heat transfer performance of those nanofluids under certain conditions of regime (according to Mouromtseff number).

- The use of solar salt and Al/Cu nePCM nanofluids as TES material can overall represent a positive economic and environmental impact.

Regarding challenges related to the use of nanofluids at high temperature, colloidal stability was a key issue since the current state of the art did not allow for a quantified analysis. A new methodology and procedure was developed for this purpose, measuring for the first time the colloidal stability of a nanofluid at high temperature. Additionally, a redispersion mechanism was also successfully developed to revert the effects of agglomeration. The conclusions corresponding to this section of the work are presented in detail next:

- A new method to measure colloidal stability of nanofluids at high temperature has been developed. It consists of an experimental set-up containing an external DLS equipment paired with a high temperature cuvette and a visualisation system.

- The novel set up for colloidal stability analysis was calibrated ensuring its reliability by comparing with an established commercial DLS equipment.

- Colloidal stability of solar salt-based nanofluids has been measured for the first time attending to the evolution of particle size distributions when the salt is melted.

- The combination of base fluid and nanoparticle, as well as the temperature, play a key role in colloidal stability.

- Ionic strength of the base fluid and Debye length of the combination are critical to the formation of agglomerates and hence, the colloidal stability of the nanofluid.

- Solar salt-based nanofluids studied (with SiO_2 and Al/Cu nePCM nanoparticles) have a lack of stability and the particle size distribution tends towards bigger cluster sizes through time.

- Mechanical redispersion consisting on a rotational engine connected to a blade at 1000 rpm effectively breaks down the clusters of particle to their initial particle size distribution in Al/Cu nePCM nanofluids.

As a step further in the nature of nePCMs, atomic layer deposition was presented as a useful method for the synthesis of coatings that can serve as encapsulation. In this thesis, multi-coated nePCMs were studied, using the second coating as a barrier against oxidation of the cores that provides the nePCM with an enhanced resistance to thermal cycling that could extend its working lifespan. The goals achieved in this respect are itemised as follows:

- Atomic layer deposition is a suitable technique to synthesise uniform nanometric coatings on nanoparticles that could be used as an encapsulation in nePCMs, and whose thickness can be easily tuned according to the number of ALD cycles performed.

- Coatings of SiO_2 and Al_2O_3 can be deposited by ALD over Sn@SnO$_x$ nePCMs, forming uniform and conformal encapsulation layers.

- Second encapsulations consisting of 8 nm SiO_2 and 10 nm Al_2O_3 coatings synthesised by ALD can act as an effective barrier against oxidation of the material in the nePCM core when subject to thermal cycling in nitrogen atmosphere.

- A coating of 10 nm of Al_2O_3 synthesised by ALD on Sn@SnO$_x$ nePCMs effectively prevents oxidation of the material in the nePCM core through thermal cycling in oxidising atmospheres.

- Specific heat of solar salt is enhanced by the addition of Sn@SnO$_2$@SiO$_2$ and Sn@SnO@Al$_2$O$_3$ multi-coated nanoparticles up to 8% and 11%, respectively.

- Thermal energy storage capacity of the nanofluids containing Sn@SnO$_2$@SiO$_2$ and Sn@SnO@Al$_2$O$_3$ nePCMs is significantly improved, reaching enhancements of 7% and 10% respectively when compared to solar salt alone at a constant volume basis.

Overall, this thesis as a whole offers a significant study on the opportunities that new materials for thermal applications at medium- and high-temperature offer. The possibility of including the contribution of the latent heat inherent to nePCMs in TES materials that commonly base their operation in sensible heat opens a new technologic field that can be explored in order to make this processes more efficient. This, paired with the increases usually achieved through the use of nanofluids in heat transfer capacity and, in the case of ionic liquids, sometimes also in sensible heat storage, makes the nanofluids developed through this work very relevant for their application in industries like solar thermal energy. All in all, they appear as a promising alternative for current materials that could boost the use of renewable energies, leading to the attainment of a cleaner world.

Chapter 9: GAPS AND FUTURE RESEARCH

Solar thermal energy is a promising alternative for energy transition in places with a high availability of sunlight, and the thermal energy storage stage is a key part to it. The work carried in this thesis has tried to throw light in the improvement of materials used in CSP plants, in order to enhance their efficiency. There is still much to discover and many aspects in which this work can be followed, including some research gaps that have been left. Some of the continuity research lines that could be taken next are:

- Developing and characterising nanofluids based on different combinations of molten salts, such as mixtures of carbonates, paired with the selection of compatible nePCMs with high phase change enthalpies.

- Studying the nanoparticle-salt interactions in depth, trying to determine if the abnormal enhancement found in specific heat is due to the formation of new bondings, and the nature of these.

- Analysing and developing different synthesis methods for a big scale production of nanofluids, looking for nanoparticle dispersion optimisation.

- Measuring stability through time when subject to thermal cycling (increase and decrease temperature cyclically and measure always at a comparable operation point (same temperature).

- Testing the nanofluids synthesised in dynamic conditions in order to measure experimentally their heat transfer properties.

- Studying the rheological behaviour of the nanofluids at high temperature in order to model their performance in dynamic conditions.

- Testing the effect of time on supercooling (since thermodynamical processes usually take place as a result of time and temperature). In the cycles tested in this work, supercooling is assumed to take place because there is a lack of nucleation points for heterogeneous crystallisation in the nePCM cores, and so a lower temperature is needed in order for it to happen. If the nePCM core materials were maintained at a constant temperature (above the supercooling temperature but below the melting point) for a sufficient amount of time, this nucleation would maybe also take place.

- Exploring different options of coatings or multi-coatings deposited by ALD, and how they can further improve the enhancements obtained in nePCM-based nanofluids.

Chapter 10: SCIENTIFIC PRODUCTION

10.1 JOURNAL CONTRIBUTIONS

- Navarrete, N., Hernández, L., Vela, A. & Mondragón, R. Influence of the production method on the thermophysical properties of high temperature molten salt-based nanofluids. *Journal of Molecular Liquids.* 302, 112570. 2020. ISSN 0167-7322
  DOI: 10.1016/j.molliq.2020.112570

- Navarrete, N., La Zara, D., Goulas, A., Valdesueiro, D., Hernández, L., van Ommen, J. R. & Mondragón, R. Improved thermal energy storage of nanoencapsulated phase change materials by atomic layer deposition. *Solar Energy Materials & Solar Cells.* 206, 110322. 2020. ISSN 0927-0248.
  DOI: 10.1016/j.solmat.2019.110322

- Gimeno-Furió, A., Hernández, L., Navarrete, N. & Mondragón, R. Characterization study of a thermal oil-based carbon black solar nanofluid. *Renewable Energy*. 140, pp. 493-500. 2019. ISSN 0960-1481
  DOI: 10.1016/j.renene.2019.03.080

- Navarrete, N., Gimeno-Furió, A., Forner-Escrig, J., Juliá, J.E. & Mondragón, R. Colloidal stability of molten salt-based nanofluids: Dynamic Light Scattering tests at high temperature conditions. *Powder Technology*. 352, pp.1-10. 2019. ISSN 0032-5910
  DOI: 10.1016/j.powtec.2019.04.045

- Navarrete, N., Mondragón, R., Wen, D., Navarro, M.E., Ding, Y. & Juliá, J.E. Thermal energy storage of molten salt-based nanofluid containing nano-encapsulated metal alloy phase change materials. *Energy*. 167, pp. 912 - 920. 2019. ISSN 0360-5442
DOI: 10.1016/j.energy.2018.11.037

- Gimeno-Furió, A., Navarrete, N., Martínez-Cuenca, R., Juliá, J.E. & Hernández, L. Influence of high temperature exposure on the thermal and optical properties of thermal oil-based solar nanofluids. *Journal of Nanofluids*. 7 - 6, pp. 1045 - 1052. 2018. ISSN 2169-4338
DOI: 10.1166/jon.2018.1543

- Mondragón, R., Juliá, J. E., Cabedo, L. & Navarrete, N. On the relationship between the specific heat enhancement of salt-based nanofluids and the ionic exchange capacity of nanoparticles. *Scientific Reports*. 8, 7532. 2018. ISSN 2045-2322
DOI: 10.1038/s41598-018-25945-0

- Muñoz-Sanchez, B., Nieto-Maestre, J., Veca, E., Liberatore, R., Sau. S., Navarro H., Ding Y., Navarrete N., Julia J.E., Fernandez A.G. & García-Romero, A. Rheology of Solar-Salt based nanofluids for concentrated solar power. Influence of the salt purity, nanoparticle concentration, temperature and rheometer geometry. *Solar Energy Materials and Solar Cells.* 176, pp. 357-373. 2018. ISSN 0927-0248
DOI: 10.1016/j.solmat.2017.10.022

- Navarrete N., Gimeno-Furio, A., Mondragon, R., Hernandez, L., Cabedo, L., Cordoncillo, E. & Julia, J.E. Nanofluid based on self-nanoencapsulated metal/metal alloys phase change materials with tuneable crystallisation temperature. *Scientific Reports*. 7, 17580. 2017. ISSN 2045-2322
DOI: 10.1038/s41598-017-17841-w

- Gimeno-Furio, A., Navarrete, N., Mondragon, R., Hernandez, L., Martinez-Cuenca, R., Cabedo, L. & Julia, J.E. Stabilization and characterization of a nanofluid based on a eutectic mixture of diphenyl and diphenyl oxide and carbon nanoparticles under high temperature conditions. *International Journal of Heat and Mass Transfer*. 113, pp.908-913. 2017. ISSN 0017-9310
DOI: 10.1016/j.ijheatmasstransfer.2017.05.097

10.2 RECENTLY SUBMITTED PAPERS

- Gil-Font, J., Hatte, M-A., Bailey, M.R., Navarrete, N., Ventura-Espinosa, J., Goulas, A., La Zara, D., van Ommen, J.R., Mondragón, R. & Hernandez, L. Improving heat transfer of stabilised thermal oil-based tin nanofluids using biosurfactant and molecular layer deposition. Submitted to *Applied Thermal Energy.* 2020.

10.3 Book chapters

- Mondragon, R., Navarrete, N., Gimeno-Furio, A., Hernandez, L., Cabedo, L. & Julia, J. E. Chapter 11: New High-Temperature Heat Transfer and Thermal Storage Molten Salt-Based Nanofluids: Preparation, Stabilization, and Characterization. *Advances in New Heat Transfer Fluids: From Numerical to Experimental Techniques*. pp. 287 - 303. CRC Press, Taylor & Francis, New York (USA) 2017. ISBN 9781498751858
  DOI: [10.1201/9781315368184](10.1201/9781315368184)

10.4 Contribution to international conferences

- Gimeno-Furió, A., Hernández, L., Navarrete, N. & Mondragón, R. Stability and optical analysis of carbon black thermal oil-based nanofluid as direct solar energy absorber. *1st International Conference on Nanofluids (ICNf2019) and 2nd European Symposium on Nanofluids (ESNf2019).* Castelló, Spain. 2019. ISBN 9788468539171

- Navarrete, N., Hernández, L., La Zara, D., van Ommen, J. R. & Mondragón, R. Nanoencapsulation of Metallic PCMs with Atomic Layer Deposition. *1st International Conference on Nanofluids (ICNf2019) and 2nd European Symposium on Nanofluids (ESNf2019)*. Castelló, Spain. 2019. ISBN 9788468539171

- Gil-Font, J., Hatte, M.A., Gimeno-Furió, A., Navarrete, N., Mondragón, R. & Hernández, L. Development, characterization and optimization of thermal oils with enhanced thermal properties though nanoencapsulated metal phase change materials. *Eurotherm Seminar #112: Advances in Thermal Energy Storage.* Lleida, Spain. 2019. ISBN 9788491441557

- Gimeno-Furió, A., Navarrete, N., Mondragón, R., Hernández, L., Barreneche, C. & Cabedo, L. Thermal stability of the black-coloured sand for concentrated solar power applications. *Eurotherm Seminar #112: Advances in Thermal Energy Storage.* Lleida, Spain. 2019. ISBN 9788491441557

- Navarrete, N., Gimeno-Furió, A., Hernandez, L. & Mondragón, R. Thermal storage and stability characterization of a Solar Salt based nanofluid containing self-nanoencapsulated phase change material. *Eurotherm Seminar #112: Advances in Thermal Energy Storage.* Lleida, Spain. 2019. ISBN 9788491441557

- Anagnostopoulos, A., Palacios, A., Navarrete, N., Navarro, M. E., Hernandez, L. & Ding, Y. Effect of temperature on the internal structure of solar salt-SiO$_2$. *24th SolarPACES International Conference on Concentrating Solar Power and Chemical Energy Systems (SolarPACES 2018)*. Casablanca, Morocco. 2018. ISBN 9780735418660
  DOI: [10.1063/1.5117718](10.1063/1.5117718)

- Anagnostopoulos, A., Palacios, A., Navarrete, N., Navarro, H. & Ding, Y. Effect of SiO_2 nanoparticles on the internal structure of molten Solar Salt. *4th Working Group Meetings NANOUPTAKE, Workshop on Nanofluids in Energy Systems*. Naples, Italy. 2018

- Martínez-Cuenca, R., Gimeno-Furio, A., Navarrete, N., Torró, S., Chiva, S. & Hernández, L. CFD modelling of Volumetric vapour generation and its applications to the receiver design. *4th Working Group Meetings NANOUPTAKE, Workshop on Nanofluids in Energy Systems*. Naples, Italy. 2018

- Navarrete, N., Mondragón, R., Wen, D., Navarro, M. E., Ding, Y. & Juliá, J. E. Characterization of nano-encapsulated metal alloy phase change materials for a molten salt-based nanofluid. *4th Working Group Meetings NANOUPTAKE, Workshop on Nanofluids in Energy Systems*. Naples, Italy. 2018

- Gimeno-Furio, A. Navarrete, N., Martinez-Cuenca, R., Julia, J.E. & Hernandez, L. Influence of High Temperature Exposure in Thermal and Optical Properties of Thermal Oil-Based Solar Nanofluid. *1st European Symposium on Nanofluids (ESNf2017)*. Lisbon, Portugal. 2017. ISBN 9789729665356

- Navarrete, N., Gimeno-Furio, A., Mondragon, R., Hernandez, L. Cabedo, L., Cordoncillo, E. & Julia, J.E. On the use of nanoencapsulated phase change materials for thermal oil and molten salt-based nanofluids. *1st European Symposium on Nanofluids (ESNf2017)*. Lisbon, Portugal. 2017. ISBN 9789729665356

- Gimeno-Furio, A., Navarrete, N., Mondragon, R., Cervantes, E., Hernandez, L., Martinez-Cuenca, R., Cabedo, L. & Julia, J.E. Thermophysical properties of a nanofluid based on a eutectic mixture of diphenyl and diphenyl oxide and carbon black nanoparticles. 13th *International Conference on Heat Transfer, Fluid Dynamics and Thermodynamics (HEFAT 2017)*. Portoroz, Slovenia. 2017. ISBN 9781775921400

- Gimeno-Furio, A., Navarrete, N., Martinez-Cuenca, R., Mondragon, R., Julia, J.E. & Hernandez, L. Thermal and Optical Characterization of Tetraethylene Glycol-Based Solar Nanofluid At High Temperature Conditions. *12th International Conference on Heat Transfer, Fluid Dynamics and Thermodynamics (HEFAT 2016).* Malaga, Spain. 2016. ISBN 9781775921240.

- Muñoz-Sánchez, B., Nieto-Maestre, J., González-Aguilar, J., Navarrete, N., Julia, J.E., Faik, A., Bauer, T., Bonk, A., Navarro, H., Ding, Y., Uranga, N., Veca, E., Sau, S., Giménez, P., García, P. & Burgaleta, J.I. Round Robin Test on the Measurement of the Specific Heat of Solar Salt. *International Conference on Concentrating Solar Power and Chemical Energy Systems (SolarPACES 2016).* United Arab Emirates. 2016. ISBN 9780735415225
  DOI: 10.1063/1.4984438

10.5 Contribution to national conferences

Gimeno-Furio, A., Navarrete, N., Mondragon, R., Hernandez, L., Martinez-Cuenca, R., Cabedo, L. & Julia, J.E. Characterization of a nanofluid base don Therminol VP-1 and carbon nanoparticles under high temperature conditions. *10th Congreso Internacional de Ingeniería Termodinámica (CNIT10)*. Lleida, Spain. 2017. ISBN 9788491440444

REFERENCES

1. IPCC. *Summary for Policymakers. Global Warming of 1.5°C. An IPCC Special Report on the impacts of global warming of 1.5 °C above pre-industrial levels. Global Warming of 1.5°C. An IPCC Special Report on the impacts of global warming of 1.5°C above pre-industrial levels and related global greenhouse gas emission pathways, in the context of strengthening the global response to the threat of climate change,* (2018). doi:10.1017/CBO9781107415324

2. IPCC. *Climate Change 2014 Synthesis Report Summary Chapter for Policymakers*. *Ipcc* (2014). doi:10.1017/CBO9781107415324

3. International Energy Agency. *Co 2 emissions from fuel combustion*. (2011). doi:10.1670/96-03N

4. European Comission. *Annual European Union greenhouse gas inventory 1990–2017 and inventory report 2019*. (2019).

5. Fabiani Appavou, Adam Brown, Bärbel Epp, Duncan Gibb, Bozhil Kondev, Angus McCrone, Hannah E. Murdock, Evan Musolino, Lea Ranalder, Janet L. Sawin, Kristin Seyboth, Jonathan Skeen, F. S. *REN21 - 2019 Global Status Report*. (2019).

6. International Energy Agency (IEA). Key world energy Statistics. 101 (2018).

7. Ren 21 comission. *REN 21-2015 Global Status Report*. (2015).

8. Romero, M. & Steinfeld, A. Concentrating solar thermal power and thermochemical fuels. *Energy Environ. Sci.* **5**, 9234–9245 (2012).

9. Therminol. Therminol 66. 4 (1998). doi:10.1088/0950-7671/25/7/416

10. Serrano-López, R., Fradera, J. & Cuesta-López, S. Molten salts database for energy applications. *Chem. Eng. Process. - Process Intensif.* **73**, 87–102 (2013).

11. Maxwell, J. C. *A treatise on electricity and magnetism*. (Clarendon Press, Oxford UK, 1873).

12. Masuda, H., Ebata, A., Teramae, K. & Hishinuma, N. Alteration of Thermal Conductivity and Viscosity of Liquid by Dispersing Ultra-Fine Particles. Dispersion of Al2O3, SiO2 and TiO2 Ultra-Fine Particles. *Netsu Bussei* **7**, 227–233 (1993).

References

---

13.   Choi, S. U. S. Enhancing thermal conductivity of fluids with nanoparticles. in *American Society of Mechanical Engineers, Fluids Engineering Division (Publication) FED* **231**, 99–105 (1995).

14.   Tavman, I. & Turgut, A. *An investigation on thermal conductivity and viscosity of water based nanofluids*. *NATO Science for Peace and Security Series A: Chemistry and Biology* (2010). doi:10.1007/978-90-481-9029-4-8

15.   Akilu, S., Sharma, K. V., Baheta, A. T. & Mamat, R. A review of thermophysical properties of water based composite nanofluids. *Renew. Sustain. Energy Rev.* **66**, 654–678 (2016).

16.   Wen, D. & Ding, Y. Formulation of nanofluids for natural convective heat transfer applications. *Int. J. Heat Fluid Flow* **26**, 855–864 (2005).

17.   Mintsa, H. A., Roy, G., Nguyen, C. T. & Doucet, D. New temperature dependent thermal conductivity data for water-based nanofluids. *Int. J. Therm. Sci.* **48**, 363–371 (2009).

18.   Shin, D. & Banerjee, D. Experimental Investigation of Molten Salt Nanofluid for Solar Thermal Energy Application. in T30024-T30024-6 (2011). doi:10.1115/ajtec2011-44375

19.   Tiznobaik, H. & Shin, D. Enhanced specific heat capacity of high-temperature molten salt-based nanofluids. *Int. J. Heat Mass Transf.* **57**, 542–548 (2013).

20.   Dudda, B. & Shin, D. Effect of nanoparticle dispersion on specific heat capacity of a binary nitrate salt eutectic for concentrated solar power applications. *Int. J. Therm. Sci.* **69**, 37–42 (2013).

21.   Shin, D., Tiznobaik, H. & Banerjee, D. Specific heat mechanism of molten salt nanofluids. *Appl. Phys. Lett.* **104**, (2014).

22.   Riazi, H. *et al.* Specific heat control of nanofluids: A critical review. *Int. J. Therm. Sci.* **107**, 25–38 (2016).

23.   Mondragón, R., Juliá, J. E., Cabedo, L. & Navarrete, N. On the relationship between the specific heat enhancement of salt-based nanofluids and the ionic exchange capacity of nanoparticles. *Sci. Rep.* **8**, 1–12 (2018).

24.   Kuchibhatla, S. V. N. T., Karakoti, A. S. & Seal, S. Colloidal stability by surface modification. *Jom* **57**, 52–56 (2005).

25.   Chieruzzi, M., Cerritelli, G. F., Miliozzi, A. & Kenny, J. M. Effect of nanoparticles on heat capacity of nanofluids based on molten salts as PCM for thermal energy storage. *Nanoscale Res. Lett.* **8**, 1–9 (2013).

26.   Muñoz-Sánchez, B., Nieto-Maestre, J., Iparraguirre-Torres, I., García-Romero, A. & Sala-Lizarraga, J. M. Molten salt-based nanofluids as efficient heat transfer and storage materials at high temperatures. An overview of the literature. *Renew. Sustain. Energy Rev.* **82**, 3924–3945 (2018).

27.   Sheng, H. W., Lu, K. & Ma, E. Melting and freezing behavior of embedded nanoparticles in ball-milled Al-10 WT% M (M = In, Sn, Bi, Cd, Pb) mixtures. *Acta Mater.* **46**, 5195–5205 (1998).

28.   Kellermann, G. & Craievich, A. F. Melting and freezing of spherical bismuth nanoparticles confined in a homogeneous sodium borate glass. *Phys. Rev. B - Condens. Matter Mater. Phys.* **78**, 5–9 (2008).

29. Lai, C. C. *et al.* A solar-thermal energy harvesting scheme: Enhanced heat capacity of molten HITEC salt mixed with Sn/SiOxcore-shell nanoparticles. *Nanoscale* **6**, 4555–4559 (2014).

30. Cingarapu, S., Singh, D., Timofeeva, E. V & Moravek, M. R. Use of encapsulated zinc particles in a eutectic chloride salt to enhance thermal energy storage capacity for concentrated solar power. *Renew. Energy* **80**, 508–516 (2015).

31. Milián, Y. E., Gutiérrez, A., Grágeda, M. & Ushak, S. A review on encapsulation techniques for inorganic phase change materials and the influence on their thermophysical properties. *Renew. Sustain. Energy Rev.* **73**, 983–999 (2017).

32. Zhang, M. M. *et al.* Encapsulated nano-heat-sinks for thermal management of heterogeneous chemical reactions. *Nanoscale* **2**, 2790–2797 (2010).

33. Wang, M., Duong, B., Fenniri, H. & Su, M. Nanomaterial-based barcodes. *Nanoscale* **7**, 11240–11247 (2015).

34. Mondal, S. Phase change materials for smart textiles - An overview. *Appl. Therm. Eng.* **28**, 1536–1550 (2008).

35. Cabeza, L. F. *et al.* Use of microencapsulated PCM in concrete walls for energy savings. *Energy Build.* **39**, 113–119 (2007).

36. Alva, G., Lin, Y., Liu, L. & Fang, G. Synthesis, characterization and applications of microencapsulated phase change materials in thermal energy storage: A review. *Energy Build.* **144**, 276–294 (2017).

37. Liu, M. & Wang, R. Y. Size-Dependent Melting Behavior of Colloidal In, Sn, and Bi Nanocrystals. *Sci. Rep.* **5**, 16353 (2015).

38. Kim, B.-G. A large thermal hysteresis between melting and solidification temperature on nanoscale Pb particles embedded in amorphous sio2 matrix prepared by sputtering. *Met. Mater.* **5**, 309–316 (1999).

39. Smalley, R. E., Bush, W. & Mansfield, S. S0883769400013014a. (2004).

40. International Energy Agency (IEA). Energy Efficiency 2017: Market Report Series. 143 (2017). doi:10.1787/9789264284234-en

41. Wen, D., Lin, G., Vafaei, S. & Zhang, K. Review of nanofluids for heat transfer applications. *Particuology* **7**, 141–150 (2009).

42. Taylor, R. *et al.* Small particles, big impacts: A review of the diverse applications of nanofluids. *J. Appl. Phys.* **113**, (2013).

43. Buongiorno, J. *et al.* A benchmark study on the thermal conductivity of nanofluids. *J. Appl. Phys.* **106**, (2009).

44. Venerus, D. C. *et al.* Viscosity measurements on colloidal dispersions (nanofluids) for heat transfer applications. *Appl. Rheol.* **20**, 2 (2010).

45. Starace, A. K., Gomez, J. C., Wang, J., Pradhan, S. & Glatzmaier, G. C. Nanofluid heat capacities. *J. Appl. Phys.* **110**, (2011).

46. Martínez-Cuenca, R. *et al.* Forced-convective heat-transfer coefficient and pressure drop of water-based nanofluids in a horizontal pipe. *Appl. Therm. Eng.* **98**, 841–849 (2016).

47. Liu, M. & Wang, R. Y. Phase change nanocomposites with tunable melting temperature and thermal energy storage density. *Nanoscale* **5**, 7234–7237 (2013).

48. Khan, P. Y., Bhattacharya, V., Biswas, K. & Chattopadhyay, K. Melting and solidification behavior of Pb-Sn embedded alloy nano-particles. *J. Nanoparticle Res.* **15**, (2013).

49. Wang, H. & Zhu, H. Melting of Pb Nanocrystals Embedded in Al, Si, and Cu Matrices. *Nanoscale Res. Lett.* **10**, 1–9 (2015).

50. Liu, M., Ma, Y., Wu, H. & Wang, R. Y. Metal matrix-metal nanoparticle composites with tunable melting temperature and high thermal conductivity for phase-change thermal storage. *ACS Nano* **9**, 1341–1351 (2015).

51. Hong, Y. *et al.* Enhancing heat capacity of colloidal suspension using nanoscale encapsulated phase-change materials for heat transfer. *ACS Appl. Mater. Interfaces* **2**, 1685–1691 (2010).

52. Hong, Y. *et al.* Controlling super-cooling of encapsulated phase change nanoparticles for enhanced heat transfer. *Chem. Phys. Lett.* **504**, 180–184 (2011).

53. Cingarapu, S., Singh, D., Timofeeva, E. V. & Moravek, M. R. Nanofluids with encapsulated tin nanoparticles for advanced heat transfer and thermal energy storage. *Int. J. energy Res.* **38**, 51–59 (2014).

54. Zou, C., Gao, Y., Yang, B. & Zhai, Q. Melting and solidification properties of the nanoparticles of Sn3.0Ag0.5Cu lead-free solder alloy. *Mater. Charact.* **61**, 474–480 (2010).

55. Lai, S. L., Guo, J. Y., Petrova, V., Ramanath, G. & Allen, L. H. Size-dependent melting properties of small tin particles: Nanocalorimetric measurements. *Phys. Rev. Lett.* **77**, 99–102 (1996).

56. Jiang, H., Moon, K. s., Dong, H., Hua, F. & Wong, C. P. Size-dependent melting properties of tin nanoparticles. *Chem. Phys. Lett.* **429**, 492–496 (2006).

57. US R Nanomaterials, I. Tin Nano powder technical data (60-80nm). (2017). Available at: http://www.us-nano.com/inc/sdetail/427.

58. US R Nanomaterials, I. Tin Nano powder technical data (300nm). (2017). Available at: http://www.us-nano.com/inc/sdetail/23090.

59. Zhu, T. S. & Li, M. Size-dependent freezing temperature of metallic and semi-metallic nanoparticles. *Mater. Res. Bull.* **63**, 253–255 (2015).

60. Alva, G., Lin, Y. & Fang, G. An overview of thermal energy storage systems. *Energy* **144**, 341–378 (2018).

61. Mahian, O., Kianifar, A., Kalogirou, S. A., Pop, I. & Wongwises, S. A review of the applications of nanofluids in solar energy. *Int. J. Heat Mass Transf.* **57**, 582–594 (2013).

62. Mondragon, R. *et al.* New high-temperature heat transfer and thermal storage molten salt-based nanofluids preparation, stabilization, and characterization. in *Advances in New Heat Transfer Fluids: From Numerical to Experimental Techniques* 287–303 (Taylor & Francis Group, LLC, 2017). doi:10.1201/9781315368184

63. Pfleger, N., Bauer, T., Martin, C., Eck, M. & Wörner, A. Thermal energy storage - overview and specific insight into nitrate salts for sensible and latent heat storage. *Beilstein J. Nanotechnol.* **6**, 1487–1497 (2015).

64. Gasia, J., Miró, L. & Cabeza, L. F. Review on system and materials requirements for high temperature thermal energy storage. Part 1: General requirements. *Renew. Sustain. Energy Rev.* **75**, 1320–1338 (2017).

65. Zhang, Z., Alva, G., Gu, M. & Fang, G. Experimental investigation on n–octadecane/polystyrene/expanded graphite composites as form–stable thermal energy storage materials. *Energy* **157**, 625–632 (2018).

66. Zhang, H., Kong, W., Tan, T. & Baeyens, J. High-efficiency concentrated solar power plants need appropriate materials for high-temperature heat capture, conveying and storage. *Energy* **139**, 52–64 (2017).

67. Kahwaji, S., Johnson, M. B., Kheirabadi, A. C., Groulx, D. & White, M. A. A comprehensive study of properties of paraffin phase change materials for solar thermal energy storage and thermal management applications. *Energy* **162**, 1169–1182 (2018).

68. Bonk, A., Sau, S., Uranga, N., Hernaiz, M. & Bauer, T. Advanced heat transfer fluids for direct molten salt line-focusing CSP plants. *Prog. Energy Combust. Sci.* **67**, 69–87 (2018).

69. Andreu-Cabedo, P. *et al.* Increment of specific heat of Solar Salt with SiO2 and Al2O3 nanoparticles. *Nanoscale Res. Lett.* **9**, 582 (2014).

70. Lasfargues, M., Stead, G., Amjad, M., Ding, Y. & Wen, D. In Situ Production of Copper Oxide Nanoparticles in a Binary Molten Salt for Concentrated Solar Power Plant Applications. *Materials (Basel).* **10**, 537 (2017).

71. Hu, Y., He, Y., Zhang, Z. & Wen, D. Effect of Al2O3 nanoparticle dispersion on the specific heat capacity of a eutectic binary nitrate salt for solar power applications. *Energy Convers. Manag.* **142**, 366–373 (2017).

72. Qiao, G., Lasfargues, M., Alexiadis, A. & Ding, Y. Simulation and experimental study of the specific heat capacity of molten salt based nanofluids. *Appl. Therm. Eng.* **111**, 1517–1522 (2016).

73. Luo, Y., Du, X., Awad, A. & Wen, D. Thermal energy storage enhancement of a binary molten salt via in-situ produced nanoparticles. *Int. J. Heat Mass Transf.* **104**, 658–664 (2017).

74. Chieruzzi, M., Cerritelli, G. F., Miliozzi, A., Kenny, J. M. & Torre, L. Heat capacity of nanofluids for solar energy storage produced by dispersing oxide nanoparticles in nitrate salt mixture directly at high temperature. *Sol. Energy Mater. Sol. Cells* **167**, 60–69 (2017).

75. Awad, A., Navarro, H., Ding, Y. & Wen, D. Thermal-physical properties of nanoparticle-seeded nitrate molten salts. *Renew. Energy* **120**, 275–288 (2018).

76. Paul, T. C., Morshed, A. K. M. M., Fox, E. B. & Khan, J. A. Enhanced thermophysical properties of NEILs as heat transfer fluids for solar thermal applications. *Appl. Therm. Eng.* **110**, 1–9 (2017).

77. Nieto De Castro, C. A. *et al.* Enhanced thermal conductivity and specific heat capacity of carbon nanotubes ionanofluids. *Int. J. Therm. Sci.* **62**, 34–39 (2012).

78. Navarrete, N. *et al.* Nanofluid based on self-nanoencapsulated metal/metal alloys phase change materials with tuneable crystallisation temperature. *Sci. Rep.* **7**, 1–10 (2017).

79. Jamekhorshid, A., Sadrameli, S. M. & Farid, M. A review of microencapsulation methods of phase change materials (PCMs) as a thermal energy storage (TES) medium. *Renew. Sustain. Energy Rev.* **31**, 531–542 (2014).

80. Ferrer, G., Barreneche, C., Solé, A., Martorell, I. & Cabeza, L. F. New proposed methodology for specific heat capacity determination of materials for thermal energy storage (TES) by DSC. *J. Energy Storage* **11**, 1–6 (2017).

81. Hentschke, R. On the specific heat capacity enhancement in nanofluids. *Nanoscale Res. Lett.* **11**, 1–11 (2016).

82. Perry, R. & Green, D. *Perry's chemical engineers' handbook.* (2001).

83. Wagner, S. J. & Rubin, E. S. Economic implications of thermal energy storage for concentrated solar thermal power. *Renew. Energy* **61**, 81–95 (2014).

84. Yu, W., Timofeeva, E. V., Singh, D., France, D. M. & Smith, R. K. Investigations of heat transfer of copper-in-Therminol 59 nanofluids. *Int. J. Heat Mass Transf.* **64**, 1196–1204 (2013).

85. Minea, A. A. & Moldoveanu, M. G. Studies on Al2O3, CuO, and TiO2 water-based nanofluids: A comparative approach in laminar and turbulent flow. *J. Eng. Thermophys.* **26**, 291–301 (2017).

86. Gimeno-Furio, A. *et al.* Stabilization and characterization of a nanofluid based on a eutectic mixture of diphenyl and diphenyl oxide and carbon nanoparticles under high temperature conditions. *Int. J. Heat Mass Transf.* **113**, 908–913 (2017).

87. Einstein, A. *Eine neue Bestimmung der Moleküldimensionen*. (Ann Phys, 1906). doi:https://doi.org/10.1002/andp.19063240204

88. Bergna, H. E. & Roberts, W. O. *Colloidal silica: fundamental and applications*. **131**, (Taylor & Francis Group, LLC, 2005).

89. Shaw, D. J. *Introduction to Colloid and Surface Chemistry*. (Butterworth-Heinemann, Oxford, UK, 1991).

90. U, D. Q. & Berli, C. *Energy of interaction in colloids and its implications in rheological modeling*. (2002).

91. Mondragon, R., Julia, J. E., Barba, A. & Carlos, J. Characterization of silica – water nano fl uids dispersed with an ultrasound probe : A study of their physical properties and stability. *Powder Technol.* **224**, 138–146 (2012).

92. Zhang, H. *et al.* Stable colloids in molten inorganic salts. *Nature* **542**, 328–331 (2017).

93. Gebbie, M. A. *et al.* Long range electrostatic forces in ionic liquids. *Chem. Commun.* **53**, 1214–1224 (2017).

94. Gebbie, M. A., Dobbs, H. A., Valtiner, M. & Israelachvili, J. N. Long-range electrostatic screening in ionic liquids. *Proc. Natl. Acad. Sci. U. S. A.* **112**, 7432–7437 (2015).

95. Mondragón, R., Segarra, C., Martínez-cuenca, R., Juliá, J. E. & Carlos, J. Experimental characterization and modeling of thermophysical properties of nano fl uids at high temperature conditions for heat transfer applications. *Powder Technol.* **249**, 516–529 (2013).

96. Torres-Mendieta, R. *et al.* Characterization of Tin/Ethylene Glycol Solar Nanofluids

Synthesized by Femtosecond Laser Radiation. *ChemPhysChem* **18**, 1055–1060 (2017).

97. Torres-Mendieta, R. *et al.* Fabrication of gold nanoparticles in Therminol VP-1 by laser ablation and fragmentation with fs pulses. *Laser Phys. Lett.* **11**, 126001 (2014).

98. Jo, B. & Banerjee, D. Enhanced specific heat capacity of molten salt-based nanomaterials: Effects of nanoparticle dispersion and solvent material. *Acta Mater.* **75**, 80–91 (2014).

99. Park, S.-J. & Seo, M.-K. Chapter 1 – Intermolecular Force. in *Interface Science and Technology* **18**, 1–57 (Elsevier, 2011).

100. Bergstrom, L. Chapter 9: Colloidal Processing of Ceramics. in *Handbook of Applied Surface and Colloid Chemistry* (John Wiley & Sons, LTD, 2001).

101. Griffin, B. A. & Jurinak, J. J. Estimation of activity coefficientes from the electrical conductivity of natural aquatic systems and soil extracts. *Soil Sci.* **116**, 26–30 (1973).

102. Ohshima, H. Interaction of colloidal particles. in *Colloid and Interface Science in Pharmaceutical Research and Development* 1–28 (Elsevier, 2014). doi:10.1016/B978-0-444-62614-1.00001-6

103. Liang, Y., Hilal, N., Langston, P. & Starov, V. Interaction forces between colloidal particles in liquid: Theory and experiment. *Adv. Colloid Interface Sci.* **134**–**135**, 151–166 (2007).

104. Luo, X., Wang, J., Dooner, M. & Clarke, J. Overview of current development in electrical energy storage technologies and the application potential in power system operation. *Appl. Energy* **137**, 511–536 (2015).

105. Oró, E., Gil, A., de Gracia, A., Boer, D. & Cabeza, L. F. Comparative life cycle assessment of thermal energy storage systems for solar power plants. *Renew. Energy* **44**, 166–173 (2012).

106. Wei, G. *et al.* Selection principles and thermophysical properties of high temperature phase change materials for thermal energy storage: A review. *Renew. Sustain. Energy Rev.* **81**, 1771–1786 (2018).

107. Khare, S., Dell'Amico, M., Knight, C. & McGarry, S. Selection of materials for high temperature latent heat energy storage. *Sol. Energy Mater. Sol. Cells* **107**, 20–27 (2012).

108. Zalba, B., Marín, J. M., Cabeza, L. F. & Mehling, H. Review on thermal energy storage with phase change: Materials, heat transfer analysis and applications. *Applied Thermal Engineering* **23**, 251–283 (2003).

109. Sharma, A., Tyagi, V. V., Chen, C. R. & Buddhi, D. Review on thermal energy storage with phase change materials and applications. *Renewable and Sustainable Energy Reviews* **13**, 318–345 (2009).

110. Liu, H., Wang, X. & Wu, D. Innovative design of microencapsulated phase change materials for thermal energy storage and versatile applications: A review. *Sustain. Energy Fuels* **3**, 1091–1149 (2019).

111. Hassan, A., Laghari, M. S. & Rashid, Y. Micro-encapsulated phase change materials: A review of encapsulation, safety and thermal characteristics. *Sustain.* **8**, (2016).

112. Navarrete, N. *et al.* Thermal energy storage of molten salt –based nanofluid containing nano-encapsulated metal alloy phase change materials. *Energy* **167**, 912–920 (2019).

113. Van Bui, H., Grillo, F. & Van Ommen, J. R. Atomic and molecular layer deposition: off the beaten track. *Chem. Commun.* **53**, 45–71 (2017).

114. Wank, J. R., George, S. M. & Weimer, A. W. Coating fine nickel particles with Al2O3 utilizing an atomic layer deposition-fluidized bed reactor (ALD-FBR). *J. Am. Ceram. Soc.* **87**, 762–765 (2004).

115. Weimer, M. A. *et al.* Ultrafast metal-insulator varistors based on tunable Al2 O3 tunnel junctions. *Appl. Phys. Lett.* **92**, 1–4 (2008).

116. King, D. M. *et al.* In situ synthesis of TiO 2-functionalized metal nanoparticles. *Ind. Eng. Chem. Res.* **48**, 352–360 (2009).

117. Kilbury, O. J. *et al.* Atomic layer deposition of solid lubricating coatings on particles. *Powder Technol.* **221**, 26–35 (2012).

118. Uuideküll, P. *et al.* Atomic layer deposition of titanium oxide films on As-synthesized magnetic Ni particles: Magnetic and safety properties. *J. Magn. Magn. Mater.* **429**, 299–304 (2017).

119. Zhang, S. *et al.* Helium interactions with alumina formed by atomic layer deposition show potential for mitigating problems with excess helium in spent nuclear fuel. *J. Nucl. Mater.* **499**, 301–311 (2018).

120. Moghtaderi, B., Shames, I. & Doroodchi, E. Combustion prevention of iron powders by a novel coating method. *Chem. Eng. Technol.* **29**, 97–103 (2006).

121. Hakim, L. F. *et al.* Synthesis of oxidation-resistant metal nanoparticles via atomic layer deposition. *Nanotechnology* **18**, 345603 (2007).

122. Zhou, Y. *et al.* Synthesis of photoactive magnetic nanoparticles with atomic layer deposition. *Ind. Eng. Chem. Res.* **49**, 6964–6971 (2010).

123. Cremers, V. *et al.* Oxidation barrier of Cu and Fe powder by atomic layer deposition. *Surf. Coatings Technol.* 1032–1041 (2018).

124. Ferguson, J. D., Buechler, K. J., Weimer, A. W. & George, S. M. SnO2 atomic layer deposition on ZrO2 and Al nanoparticles: Pathway to enhanced thermite materials. in *Powder Technology* **156**, 154–163 (Elsevier, 2005).

125. Qin, L., Gong, T., Hao, H., Wang, K. & Feng, H. Core-shell-structured nanothermites synthesized by atomic layer deposition. *J. Nanoparticle Res.* **15**, (2013).

126. Qin, L. *et al.* Enhanced energy performance from core-shell structured Al@Fe2O3 nanothermite fabricated by atomic layer deposition. *RSC Adv.* **7**, 7188–7197 (2017).

127. Manandhar, K., Wollmershauser, J. A., Boercker, J. E. & Feigelson, B. N. Growth per cycle of alumina atomic layer deposition on nano- and micro-powders. *J. Vac. Sci. Technol. A Vacuum, Surfaces, Film.* **34**, 021519 (2016).

128. Miikkulainen, V., Leskelä, M., Ritala, M. & Puurunen, R. L. Crystallinity of inorganic films grown by atomic layer deposition: Overview and general trends. *J. Appl. Phys.* **113**, 021301 (2013).

129. Beetstra, R., Lafont, U., Nijenhuis, J., Kelder, E. M. & Van Ommen, J. R. Atmospheric pressure process for coating particles using atomic layer deposition. *Chem. Vap. Depos.* **15**, 227–233 (2009).

130. Ferguson, J. D., Weimer, A. W. & George, S. M. Atomic layer deposition of SiO2 films on BN particles using sequential surface reactions. *Chem. Mater.* **12**, 3472–3480 (2000).

131. Socrates, G. *Infrared and Raman Characteristic Group Frequencies: Tables and Charts*. (John Wiley & Sons, LTD, 2004).

132. Goldstein, D. N., McCormick, J. A. & George, S. M. Al2O3Atomic layer deposition with trimethylaluminum and ozone studied by in situ transmission FTIR spectroscopy and quadrupole mass spectrometry. *J. Phys. Chem. C* **112**, 19530–19539 (2008).

133. Valdesueiro, D., Meesters, G. M. H., Kreutzer, M. T. & van Ommen, J. R. Gas-phase deposition of ultrathin aluminium oxide films on nanoparticles at ambient conditions. *Materials (Basel).* **8**, 1249–1263 (2015).

134. Zhang, D., Zara, D. La, Quayle, M. J., Petersson, G. & Ommen, J. R. Van. Nanoengineering of Crystal and Amorphous Surfaces of Pharmaceutical Particles for Biomedical Applications. (2019). doi:10.1021/acsabm.8b00805